Spring 2017

Photoproduction and Radiative Decay of ηt Meson in CLAS at JLAB

Georgie Mbianda Njencheu
Old Dominion University

PHOTOPRODUCTION AND RADIATIVE DECAY OF η' MESON IN CLAS AT JLAB

by

Georgie Mbianda Njencheu
M.S. May 2012, Old Dominion University

A Dissertation Submitted to the Faculty of
Old Dominion University in Partial Fulfillment of the
Requirements for the Degree of

DOCTOR OF PHILOSOPHY

PHYSICS

OLD DOMINION UNIVERSITY
May 2017

Approved by:

Moskov Amaryan (Director)

Charles Hyde (Member)

Sylvain Marsillac (Member)

Anatoly Radyushkin (Member)

Charles Sukenik (Member)

ABSTRACT

PHOTOPRODUCTION AND RADIATIVE DECAY OF η' MESON IN CLAS AT JLAB

Georgie Mbianda Njencheu
Old Dominion University, 2017
Director: Dr. Moskov Amaryan

In this work the η' meson photoproduction cross sections as well as the distribution of the di-pion invariant mass, $m(\pi^+\pi^-)$, in the radiative decay mode $\eta' \to \pi^+\pi^-\gamma$ have been measured using the CLAS detector at the Thomas Jefferson National Accelerator Facility using tagged incident photons in the center-of-mass energy range 1.96 GeV - 2.72 GeV. The measurements are performed on a liquid hydrogen target in the reaction $\gamma p \to p\eta'(\eta' \to \pi^+\pi^-\gamma)$. The analysis is based on the highest statistics collected in this decay channel in comparison to other experiments reported so far.

The η' photoproduction cross sections measured with radiative decay are in a good agreement with results of previous publication from the same data set in CLAS obtained through $\eta' \to \pi^+\pi^-\eta$ decay mode. Two free parameters, α and β, are extracted from a model-independent fit to the $m(\pi^+\pi^-)$ distribution and their values are found to agree well with recent theoretical expectations. The results of both parameters confirm the existence of the box anomaly, ρ-ω mixing and effects of the $a_2(1320)$ tensor meson in the radiative decay of η'.

ACKNOWLEDGEMENTS

It will be difficult to thank everyone who contributed to this achievement. However I will attempt to mention everyone that I can.

I wish to thank my committee members who were more than generous with their expertise and precious time. A special thanks to my supervisor, Dr. Moskov Amaryan for giving me the opportunity to work on this experiment. I am grateful for his help, support and guidance. He has been very generous and is truly a respectful person. Moskov is a very enthusiastic and dynamic physicist. Thank you Dr. Charles Hyde, Dr. Sylvain Marsillac, Dr. Anatoly Radyushkin and Dr. Charles Sukenik for agreeing to serve on my committee.

My special thanks goes to Dr. Michael Kunkel from whom I benefited enormously from his accessibility and willingness to discuss any issue I encountered, including the adaptation of his analysis engine to suit my experiment. In the same light I have to thank Dr. Ilya Larin for contributing in many ways to the progress of this work. I cannot speculate on the level of analysis I would have attained without Ilya's assistance.

Being in the Light Meson Decay (`LMD`) group has introduced me to fantastic people who have helped me in innumerable ways. I must, in particular, thank Dr. Gagik Gavalian and Sudeep Ghosh for their enormous contribution to this work.

DEDICATION

I dedicate my dissertation work to my family, relatives and friends for all the support, care and unconditional love. A special feeling of gratitude to my parents, Joseph Njike Mbianda and Marie Nchengwe Mboue, for believing in me and whose push for tenacity and words of encouragement resonate in my ears.

I also dedicate this work and give special thanks to my loving wife, Gisele Feumba Tonji, for all of her immeasurable support and sacrifices. I look forward to all the hard work and dedication we will input into our lives with the reward of companionship and love.

I dedicate this dessertation to my wonderful kids, Arella-Marlee Njiomoun Mbianda, Bryanelle Nchengwe Mbianda, Oumi Mbianda Njencheu and Rey-Samuel Mbianda Tonji, for all the happiness they have brought to my life.

TABLE OF CONTENTS

LIST OF TABLES

LIST OF FIGURES

CHAPTER 1

INTRODUCTION AND MOTIVATION

The $\eta'(958)$ is a pseudoscalar meson consisting of a mixture of three flavors of quarks: up (u) and anti-up ($\bar{u}$), down (d) and anti-down ($\bar{d}$), then strange (s) and anti-strange ($\bar{s}$) quarks. It should be noted that although η' does have a strange quark content, it has no net strangeness. The η' meson can be produced through various reactions, one of which is photoproduction. This particle has different decay channels, one of which is radiative decay. Radiative decays are known to be very sensitive tools to explore decay mechanisms. Especially, when studied together with two hadrons as decay products, they enable us to adjust the invariant mass of the two-hadron system via a variation of the photon energy without interference of strong three-body final state interactions. In this work we will discuss the photoproduction of the η' meson on a proton target ($\gamma p \to p\eta'$) and then its radiative decay ($\eta' \to \pi^+\pi^-\gamma$). This radiative decay is governed by the chiral anomaly. Chiral anomaly is the non conservation of the axial vector current under quantization when gauge fields are present. The anomalous decay of the π^0, also a pseudoscalar meson, was first measured in the 1960s [1] and have been updated in the recent years [2]. Radiative decays are of special interest as they provide deep insight into different aspects of particle physics.

The electromagnetic processes influenced by axial anomaly [3] are of considerable theoretical interest. Among them are the transitions of types $P^0(p) \to \gamma^*(k_1)\gamma^*(k_2)$ and $\gamma^*(q) \to P^+(p_1)P^0(p_2)P^-(p_3)$, where γ^* denotes a, generally, virtual ($q^2 \neq 0$) photon γ, $P^\pm$ stands for a charged and P^0 for a neutral meson from the pseudoscalar nonet, up to the strangeness conservation (so that $P^\pm = \pi^\pm, K^\pm$ and $P^0 = \pi^0, \eta, \eta'$). Processes of the first type are governed by the better understood triangle anomaly, FIG. 1. While processes of the second kind are influenced by the box anomaly, since on the microscopic level, the three pseudoscalar (P) mesons would couple to the photon through a four-vertex quark loop, as shown in FIG. 2.

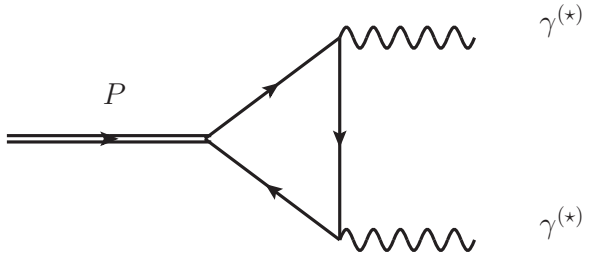

FIG. 1. A triangle diagram for a pseudoscalar meson decaying to 2γ's

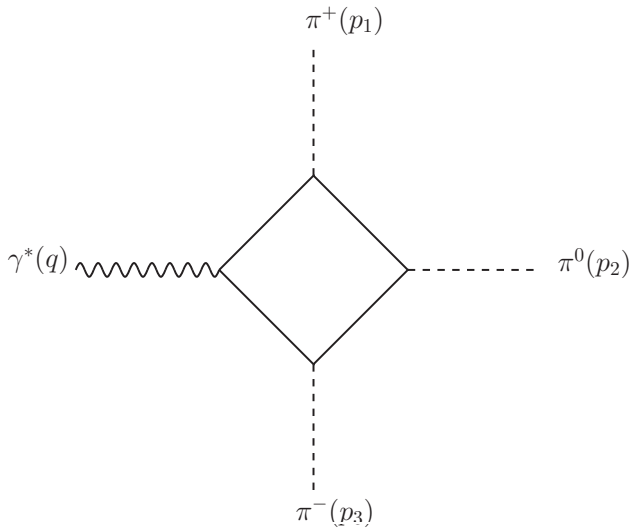

FIG. 2. A box diagram for the process $\gamma^* \to \pi^+\pi^0\pi^-$.

In the chiral limit (where $m_\pi = 0$) and the soft-point limit (of vanishing 4-momenta of external particles, $p_j = 0 = q$), which is a reasonably realistic approximation at low energies at least for the lightest pseudoscalars - the pions, the anomaly analysis predicts [4] that the theoretical amplitude is exactly

$$A_\gamma^{3\pi} \equiv \lim_{m_\pi \to 0} F_\gamma^{3\pi}(p_1 = 0, p_2 = 0, p_3 = 0) = \frac{e\, N_c}{12\pi^2\, f_\pi^3}\,, \tag{1}$$

where e is the proton charge, $N_c = 3$ the number of quark colors, and the pion decay constant $f_\pi = (90 \pm 5)$ MeV, whereby $A_\gamma^{3\pi} = (10.5 \pm 1.5)\,\mathrm{GeV}^{-3}$.

On the other hand, the experimental knowledge of the processes that should be influenced by the "box anomaly" is not at all satisfactory, being quite scant. For the $\gamma^* \to \pi^+\pi^0\pi^-$ processes, which should be best approximated by the anomaly prediction (Eqn. 1) since it involves only the lightest pseudoscalars, there is only one published experimental value for the amplitude at finite momenta p_j, i.e., the form factor $F_\gamma^{3\pi}(p_1, p_2, p_3)$. It was extracted from the cross-section measured at Serpukhov in the transition $\pi^-\gamma^* \to \pi^0\pi^-$ through the Primakoff effect, so that its value $F_\gamma^{3\pi}(\mathrm{expt}) = 12.9 \pm 0.9 \pm 0.5\,\mathrm{GeV}^{-3}$ really corresponds to the average value of the form factor over the momentum range covered by the experiment. The π^- scattering on electrons at CERN SPS yielded the total cross section [3] consistent with the Serpukhov value.

A new high-statistic data on the reaction $\pi^-\gamma^* \to \pi^-\pi^0$ transition are expected soon from the COMPASS experiments at CERN [5].

Thus the analysis of the radiative decay of η' from the $g11$ experiment in `CLAS` at `JLAB` may finally confirm the relation (Eqn. 2) between the "box anomaly" processes and the much better understood and measured "triangle anomaly" processes (FIG. 1), notably the $\pi^0(p) \to \gamma(k_1)\gamma(k_2)$ decay into two real photons, $k_1^2 = 0 = k_2^2$. Namely, the pertinent chiral-limit and soft-point amplitudes $A_\pi^{2\gamma}$ and $A_\gamma^{3\pi}$ are related [6] as

$$A_\pi^{2\gamma} = e f_\pi^2 A_\gamma^{3\pi}. \tag{2}$$

In this work, many thousands of η' events were detected that could be used to expand the world database on the differential cross sections for the photoproduction process as well as improve on the findings of chiral anomaly.

η' has a mean lifetime of $(3.2 \pm 0.2) \times 10^{-21}$ s, a full decay width of 0.198 ± 0.009 MeV and commonly decays into $\pi^+\pi^-\eta$ (BF= $(42.9 \pm 0.7)\%$), $\rho^0\gamma/\pi^+\pi^-\gamma$ (BF= $(29.1 \pm 0.5)\%$) or $\pi^0\pi^0\eta$ (BF= $(22.2 \pm 0.8)\%$). There are also other decay modes of η', with considerably lower branching fractions (BF$< 5\%$) as shown in Table 1.

Mode	Branching ratio
$\eta' \to \pi^+\pi^-\eta$	$(42.9 \pm 0.7) \cdot 10^{-2}$
$\eta' \to \rho_0\gamma$ (including non-resonant $\pi^+\pi^-\gamma$)	$(29.1 \pm 0.5) \cdot 10^{-2}$
$\eta' \to \pi^0\pi^0\eta$	$(22.3 \pm 0.8) \cdot 10^{-2}$
$\eta' \to \omega\gamma$	$(2.62 \pm 0.13) \cdot 10^{-2}$
$\eta' \to \gamma\gamma$	$(2.10 \pm 0.12) \cdot 10^{-2}$
$\eta' \to 3\pi^0$	$(1.61 \pm 0.23) \cdot 10^{-3}$
$\eta' \to \mu^+\mu^-\gamma$	$(1.03 \pm 0.26) \cdot 10^{-4}$
$\eta' \to \pi^+\pi^-\mu^+\mu^-$	$< 2.3 \cdot 10^{-4}$
$\eta' \to \pi^+\pi^-\pi^0$	$(3.7 - 1.0 + 1.1) \cdot 10^{-3}$
$\eta' \to \pi^0\rho^0$	$< 4 \cdot 10^{-2}$
$\eta' \to 2(\pi^+\pi^-)$	$< 2.5 \cdot 10^{-4}$
$\eta' \to \pi^+\pi^-2\pi^0$	$< 2.6 \cdot 10^{-3}$
$\eta' \to 2(\pi^+\pi^-)$ neutrals	$< 1 \cdot 10^{-2}$
$\eta' \to 2(\pi^+\pi^-)\pi^0$	$< 1.9 \cdot 10^{-3}$
$\eta' \to 2(\pi^+\pi^-)2\pi^0$	$< 1 \cdot 10^{-2}$
$\eta' \to 3(\pi^+\pi^-)$	$< 5 \cdot 10^{-4}$
$\eta' \to \pi^+\pi^-e^+e^-$	$(2.5 - 1.0 + 1.3) \cdot 10^{-3}$
$\eta' \to e^+e^-\gamma$	$< 9 \cdot 10^{-4}$
$\eta' \to \pi^0\gamma\gamma$	$< 8 \cdot 10^{-4}$
$\eta' \to 4\pi^0$	$< 5 \cdot 10^{-4}$
$\eta' \to e^+e^-$	$< 2.1 \cdot 10^{-7}$
$\eta' \to invisible$	$< 9 \cdot 10^{-4}$

TABLE 1. branching ratios of the η' decays [7]

1.1 UNIQUE CAPABILITIES OF JLAB

High quality continuous electron beams at energies much greater than the production threshold required to produce η' meson are provided by the Continues Electron Beam Accelerator Facility (CEBAF). In addition to this high quality electron beam, experimental HALL B at JLAB has a photon tagging system that converts the kinetic energy of electrons, through the bremsstrahlung process, into electromagnetic energy. Finally, the particle detector used, the CEBAF Large Acceptance Spectrometer (CLAS) has nearly a 4π coverage to allow measurement of the reaction $\gamma p \to p\eta'$.

These unique capabilities provided by JLAB permitted measurements of the η' differential cross sections in the radiative decay channel and also provided measurements of box anomaly of a much higher statistical quality than previously obtained.

1.2 STRUCTURE OF THE THESIS

This work is organized as follows. Chapter 2 reviews the theoretical background. We shall present an overview of pseudoscalar mesons, the bremsstrahlung process, the photoproduction and radiative decay of the η' meson.

Chapter 3 explains the electron accelerator, bremsstrahlung photon tagger, cryogenic liquid hydrogen target, detectors and other instruments used in the acquisition of data.

Chapter 4 elaborates steps taken during the data analysis. We describe techniques used to identify particles and to select events of interest and also explain how the data was corrected. Furthermore, we discuss the Monte Carlo Simulation and show how it compares to the data. Here we outline how the photon flux, a parameter needed for differential cross section calculation, is obtained.

Chapter 5 states the steps used for extracting the differential cross section as well as the steps used in fitting the di-pion invariant mass distribution to extract two free parameters relating to the anomalous decay. We compare results to other experiments and theory and give our estimates of systematic uncertainties. In this chapter, we give a summary of our work and the importance of the results obained.

CHAPTER 2

THEORETICAL BACKGROUND

2.1 PSEUDOSCALAR MESONS

Different hadrons in the quark model are classified according to their quark content. Hadrons must be constructed from a quark and an antiquark or three valence quarks (or antiquarks) to make these particles be in color-neutral states. Mesons are hadrons constructed from two valence quarks, a quark and an anti-quark with color and 'anti-color', respectively. While baryons are hadrons constructed from three quarks with suitable colors. These valence quarks give rise to the quantum numbers of the hadrons via their flavor and via their symmetry J^{PC}. Here $J = L + S$ is the total angular momentum containing orbital angular momentum L and spin S, while $P = (-1)^{L+1}$ and $C = (-1)^{L+S}$ stand for parity and charge conjugation, respectively. Baryons which are constructed from three quarks, or three antiquarks are fermions (particles with an odd half interger spin). Mesons contain a quark-antiquark pair and thus are bosons (particles with an interger spin). In this section we shall only discuss light mesons built by up (u), down (d) or strange (s) quarks, which are subject to an approximate U(3) flavor symmetry. The resulting nine states can be decomposed into a singlet and an octet state. In group notation, this can be written as:

$$3 \times \bar{3} = 8 + 1 \tag{3}$$

Table 2 illustrates how the different mesons can be classified into types according to their spin configurations.

The nonet of the pseudoscalar mesons ($J^P = 0^-$) and the nonet of the vector mesons ($J^P = 1^-$) are shown in FIG. 3 and FIG. 4. Here strangeness increases towards the upward direction and the charge increases towards the right. Note, that η and η' are not the exact octet and singlet states, respectively. These are denoted by η_0 and η_8. The physical, measured particles are mixings between the η_0 and η_8 states with an η-η'-mixing angle $\theta_{mix} \approx -20^\circ$ [8]. These states can be constructed from the flavor states according to

$$\begin{pmatrix} \eta \\ \eta' \end{pmatrix} = \begin{pmatrix} -\sin\theta_{\text{mix}} & \cos\theta_{\text{mix}} \\ \cos\theta_{\text{mix}} & \sin\theta_{\text{mix}} \end{pmatrix} \cdot \begin{pmatrix} \eta_0 \\ \eta_8 \end{pmatrix}. \tag{4}$$

Type	S	L	P	J	J^P
Pseudoscalar meson	0	0	-	0	0^-
Axial vector meson	0	1	+	1	1^+
Vector meson	1	0	-	1	1^-
Scalar meson	1	1	+	0	0^+
Tensor meson	1	1	+	2	2^+

...

TABLE 2. Types of mesons

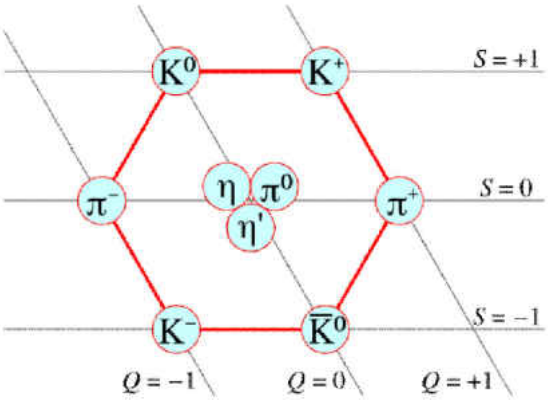

FIG. 3. nonet of pseudoscalar mesons

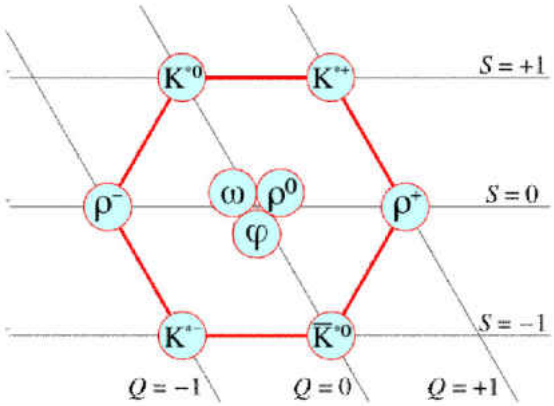

FIG. 4. nonet of vector mesons

The η and η' have a strange quark content:

$$\eta_0 \;:\; \sqrt{\frac{2}{3}}\left(u\bar{u}+d\bar{d}+s\bar{s}\right), \tag{5}$$

$$\eta_8 \;:\; \frac{1}{\sqrt{6}}\left(u\bar{u}+d\bar{d}-2s\bar{s}\right). \tag{6}$$

The masses of the mesons are $m_\eta = 547.853 \pm 0.024\,\mathrm{MeV}$ and $m_{\eta'} = (957.78 \pm 0.06)\,\mathrm{MeV}$. The decay modes and branching ratios of η' are given in Table 1.

2.2 THE BREMSSTRAHLUNG PROCESS

The η' meson photoproduction requires photons with energies high enough to create η'. Bremsstrahlung is the process by which these high energy photons were created, and then used for the η' meson photoproduction. The incident photon energy threshold for η' photoproduction is 1447 MeV. These photons created through bremsstrahlung then react with the liquid hydrogen ($l\mathrm{H}_2$) or proton target. The reaction studied here is that in which the photon-proton interaction has as final products a proton and an η' meson.

In `CLAS` the bremsstrahlung process is the electromagnetic radiation that arises due to the deceleration of an electron deflected by the Coulomb field of an atomic nucleus, that is, $eZ \rightarrow Ze\gamma$. Quantum electrodynamics (QED) predicts that there is a probability of a photon to be emitted when a charged particle interacts with a Coulomb field [9]. There are two orders, hardly distinct, in which the bremsstrahlung process may occur: (1) the charged particle (the electron in this case) interacts with the Coulomb field followed by the emission of a photon, or (2) the electron emits a photon and subsequently interacts with the Coulomb field.

The overall energy dependence of the probability that a photon of a given energy will be emitted from a bremsstrahlung process is inversely proportional to the energy of the emitted photon:

$$\frac{dN_\gamma}{dE_\gamma} \propto \frac{1}{E_\gamma} \tag{7}$$

Hence, the emission of higher energy photons is statistically unfavored over that of lower energy photons.

2.3 THE η' PHOTOPRODUCTION

A diagramatic representation of the photoproduction of the η' meson in the reaction $\gamma p \rightarrow p\eta'$ is shown in FIG. 5. Where k and p_i are the incident photon beam and proton target center-of-mass 4-momenta respectively, and q and p_f are the photoproduced η' meson and the scattered proton center-of-mass 4-momenta respectively.

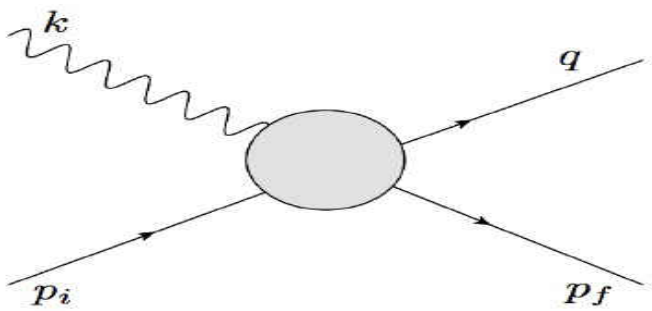

FIG. 5. Feymann diagram for photoproduction of the η' meson. k and p_i are the incident photon and target 4-momenta respectively, q and p_f are the produced η' and the scattered proton 4-momenta respectively.

A general form of the photoproduction amplitude can be written in terms of electric and magnetic multipoles. Chew, Goldberger, Low and Nambu have given a useful formalism for expressing the complete photoproduction amplitude [10]. We begin by writing the general expression for the differential cross-section for single meson production

$$\frac{d\sigma}{d\Omega} = \frac{q}{k} |\langle f| \mathcal{F} |i\rangle|^2, \tag{8}$$

The matrix elements are Pauli spinors, and the operator $\mathcal{F}$ can be written as:

$$\begin{aligned}\mathcal{F} =& i\vec{\sigma}\cdot\vec{\epsilon}\mathcal{F}_1 + \frac{1}{qk}(\vec{\sigma}\cdot\vec{\mathbf{q}})\vec{\sigma}\cdot(\vec{\mathbf{k}}\times\vec{\epsilon})\mathcal{F}_2 \\ &+ \frac{i}{qk}(\vec{\sigma}\cdot\vec{\mathbf{k}})(\vec{\mathbf{q}}\cdot\vec{\epsilon})\mathcal{F}_3 + \frac{i}{q^2}(\vec{\sigma}\cdot\vec{\mathbf{q}})(\vec{\mathbf{q}}\cdot\vec{\epsilon})\mathcal{F}_4 \ ,\end{aligned} \tag{9}$$

where $\vec{\mathbf{k}}$ and $\vec{\mathbf{q}}$ are the center-of-mass 3-momenta, $\vec{\epsilon}$ is the polarization of the photon and $\vec{\sigma}$ is the Pauli spin matrix. This form of $\mathcal{F}$ is the most general form that can be obtained requiring:

- Lorentz invariance
- linearity and homogeneity in $\vec{\epsilon}$
- gauge invariance
- parity conservation
- unitarity
- crossing symmetry

The $\mathcal{F}_i$ amplitudes are referred to as the Chew, Goldberger, Low and Nambu (CGLN) amplitudes. They can be expanded in terms of electric and magnetic multipoles ($M_{l\pm}$ and $E_{l\pm}$ respectively), and derivatives of Legendre polynomials ($P_l^{\prime(\prime)}(x)$ and $P_{l\pm1}^{\prime(\prime)}(x)$) with l being the orbital angular momentum: $(x = \cos\theta)$, where θ is the center-of-mass angle.

$$\mathcal{F}_1 = \sum_{l=0}^{\infty}[lM_{l+} + E_{l^+}]P'_{l+1}(x) + [(l+1)M_{l-1} + E_{l-}]P'_{l-1}(x) \tag{10}$$

$$\mathcal{F}_2 = \sum_{l=1}^{\infty}[(l+1)M_{l+} + lM_{l-}]P'_{l}(x) \tag{11}$$

$$\mathcal{F}_3 = \sum_{l=1}^{\infty}[E_{l+} - M_{l+}]P''_{l+1}(x) + [E_{l-} + M_{l-}]P''_{l-1}(x) \tag{12}$$

$$\mathcal{F}_4 = \sum_{l=1}^{\infty}[M_{l+} - E_{l+} - M_{l-} - E_{l-}]P''_{l}(x) \tag{13}$$

These CLGN amplitudes may be used to connect underlying electromagnetic multipoles to differential cross sections. Decomposing electromagnetic radiation into multipoles requires that a coordinate system be defined. The most convenient coordinate system for scattering experiments is to have the origin set on the target particle.

2.4 RADIATIVE DECAY OF η'

The radiative decay of pseudoscalar mesons (P) is governed by box anomaly and proceed as shown in FIG. 6. In this work, P will be the η' meson.

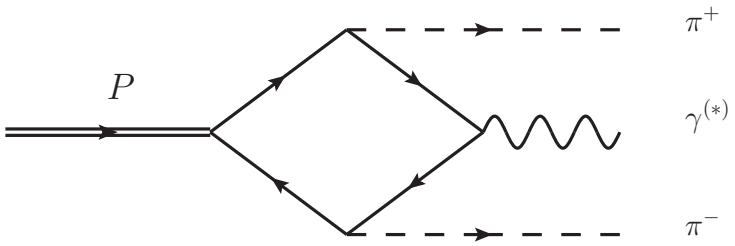

FIG. 6. A box diagram for the radiative decay of a pseudoscalar meson.

2.4.1 SYMMETRIES AND ANOMALIES

Symmetry transformations are those that do not change the physics of a system when implemented. In classical physics this means that the action and therefore the equation of motion are unchanged. In a quantum mechanical formulation, a symmetry is given if the Lagrangian is invariant under the respective transformation. The relationship between symmetries and conversation laws is expressed via the Noether theorem which says that for every continuous transformation that leaves the action invariant there exists a time independent classical charge Q and a corresponding conserved current $\partial_\mu J^\mu = 0$. There exist many different kinds of symmetries, which are all realized by nature. Listed here are two examples:

- exact symmetry: examples for exact symmetries are the electromagnetic gauge $U(1)$ or the $SU(3)$ color symmetry of quantum chromodynamics (QCD);
- anomalous symmetry: If a classical symmetry is broken in quantum physics it is called anomalous. It is not a true symmetry. An example is the axial $U(1)$ symmetry, which is the symmetry of interest here.

The concept of anomalies was introduced by Adler, Bell and Jackiw [6, 11]. Here we give a short overview of the calculations given in [12]. In the massless Dirac Lagrangian the left- and right- handed fermions are decoupled and the Lagrangian is therefore invariant under the transformation of the fields[1]:

$$\Psi \to \Psi' = e^{-i\theta\gamma_5}\Psi \tag{14}$$

The corresponding axial current

$$j_{5\mu} = \bar{\Psi}\gamma_\mu\gamma_5\Psi \tag{15}$$

is classically conserved,

$$\partial^\mu j_{5\mu} = 0. \tag{16}$$

If Ψ satisfies the Dirac equation $(i\gamma_\mu\partial^\mu - m)\Psi = 0$, then

$$\partial^\mu j_{5\mu} = (\partial^\mu\bar{\Psi})\gamma_\mu\gamma_5\Psi - \bar{\Psi}\gamma_5\gamma_\mu\partial^\mu\Psi$$

$$= (im\bar{\Psi})\gamma_5\Psi - \bar{\Psi}\gamma_5(-im\Psi)$$

[1]The (standard) notation of the γ-matrices is according to [13]. The parameter θ is real valued and $\varepsilon^{\mu\nu\alpha\beta}$ is the total antisymmetric tensor in 3+1 dimensions

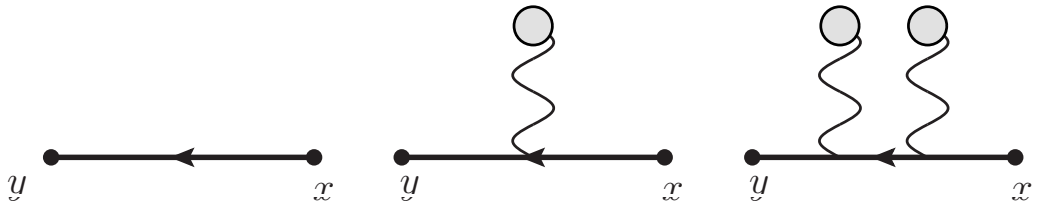

FIG. 7. higher order radiative corrections of $\Psi(y)\bar{\Psi}(x)$

$$= 2im\bar{\Psi}\gamma_5\Psi = 0$$

when $m = 0$. In Quantum Field Theory (QFT), where guage fields are present, this does not hold. The axial vector current is built from two fermion fields. Because the product of two local operators can induce singularities, their locations x and y are seperated, and the limit $(y - x) \to 0$ is taken in the end. This is visualized in FIG. 7. The lowest order contribution (without background gauge fields) results in zero, because the trace has to be taken over three γ-matrices. The next order contribution instead gives a nonvanishing result. Therefore the divergence of the current has the following form,

$$\partial^\mu j_{5\mu} = -\frac{e^2}{16\pi^2}\varepsilon^{\mu\nu\alpha\beta}F_{\mu\nu}F_{\alpha\beta}, \tag{17}$$

which is known as Adler-Bell-Jackiw anomaly [6, 11]. $F_{\mu\nu}$ is the electromagnetic field strength tensor, $F_{\mu\nu} = \partial_\mu A_\nu - \partial_\nu A_\mu$.

2.4.2 WESS-ZUMINO-WITTEN LAGRANGIAN (WZW)

The effective Wess-Zumino-Witten Lagrangian summarizes and determines the effects of anomalies in current algebra. Following the presentation of [14] and [15], the QCD Lagrangian is given by:

$$\mathcal{L}_{QCD} = -\frac{1}{2}Tr[G_{\mu\nu}G^{\mu\nu}] + \bar{q}(i\gamma_\mu D^\mu - m)q \tag{18}$$

with

$$G_{\mu\nu} = \partial_\mu G_\nu - \partial_\nu G_\mu - ig[G_\mu, G_\nu]$$
$$D_\mu q = (\partial_\mu - igG_\mu)q \tag{19}$$

where $G_\mu = G^a_\mu \lambda^a/2$ is the vector field of the gluons, $G_{\mu\nu}$ is the field strength tensor. In order to derive predictions about hadrons, low-energy chiral perturbative theory (χPT) is applied. the lowest order effective chiral action is given by:

$$\mathcal{S}_{\text{eff}} = \frac{f_\pi^2}{4} \int d^4x \ \text{Tr}[(D_\mu U)(D^\mu U^\dagger)] \tag{20}$$

with the chiral unitary matrix

$$U = \exp\left(\frac{i\sqrt{2}}{f_\pi} P\right) \tag{21}$$

and $f_\pi = 92.4$ MeV is the physical pion decay constant and P are the pseudoscalar fields [16]. In the absence of external fields, the equation of motion derived from the action in Eqn. 20 is given by:

$$\partial^\mu (f_\pi^2 U^\dagger \partial_\mu U) = 0 \tag{22}$$

As shown in [15], the equation of motion which violates extra symmetries not presnt in the `QCD` Lagrangian can be constructed by adding a symmetry violating extra term with the smallest possible number of derivatives. This is given by

$$\partial_\mu (f_\pi^2 U^\dagger \partial^\mu U) + \lambda \epsilon^{\mu\nu\alpha\beta} U^\dagger (\partial_\mu U) U^\dagger (\partial_\nu U) U^\dagger (\partial_\alpha U) U^\dagger (\partial_\beta U) = 0 \tag{23}$$

where λ is a constant and $\epsilon^{\mu\nu\alpha\beta}$ is a four-dimensional antisymmetric tensor due to violation of the extra symmetries. The Wess-Zumino five-dimensional action is constructed [15], that will lead to the equation of motion stated in Eqn. 23, as:

$$\Gamma_{WZ} = -\frac{iN_C}{240\pi^2} \int d^5x \ \epsilon^{ijklm} \text{Tr}[((\partial_i U)U^\dagger)((\partial_j U)U^\dagger)((\partial_k U)U^\dagger)((\partial_l U)U^\dagger)((\partial_m U)U^\dagger)] \tag{24}$$

This action is invariant under global charge rotations $U \to U + i\epsilon[Q, U]$, where ϵ is a constant and Q the electric charge matrix of quarks. Converting this into a local symmetry $U \to$

$U + i\epsilon(x)[Q, U]$ also changes the Wess-Zumino action to:

$$\begin{aligned}\tilde{\Gamma}(U, A_\mu) =&\Gamma(U) \; - \; \frac{e}{48\pi^2}\epsilon^{\mu\nu\alpha\beta}\int d^4x \; A_\mu \mathrm{Tr}[Q(\partial_\nu UU^\dagger)(\partial_\alpha UU^\dagger)(\partial_\beta UU^\dagger)] \\ &+ Q(U^\dagger\partial_\nu U)(U^\dagger\partial_\alpha U)(U^\dagger\partial_\beta U)] \\ &+ \; \frac{ie^2}{24\pi^2}\int d^4x \; \epsilon^{\mu\nu\alpha\beta}(\partial_\mu A_\nu)A_\alpha \\ &\times [Q^2(\partial_\beta U)U^\dagger + Q^2U^\dagger(\partial_\beta U) + QUQU^\dagger(\partial_\beta U^\dagger)] \end{aligned} \tag{25}$$

and the effective Lagrangian becomes [8]:

$$\mathcal{L} = \frac{f_\pi^2}{4}\int d^4x \; \mathrm{Tr}[(D_\mu U)(D^\mu U^\dagger)] + N_C\tilde{\Gamma} \tag{26}$$

After expanding U and intergrating by parts, one obtains

$$A = \frac{N_c e^2}{96\pi^2 f_\pi^2}\pi^0 \varepsilon^{\mu\nu\alpha\beta}F_{\mu\nu}F_{\alpha\beta}, \tag{27}$$

which is the part that describes the the triangle anomaly in the decay $\pi^0 \to \gamma\gamma$, and a term

$$B = -\frac{1}{12}\frac{N_c}{\pi^2 f_\pi^3}\epsilon^{\mu\nu\alpha\beta}A_\mu\partial_\nu\pi^+\partial_\alpha\pi^-\partial_\beta\pi^0, \tag{28}$$

that describes the coupling of a photon to three pseudoscalar mesons ($\gamma\pi^+\pi\pi^-$ - vertex) and hence the decay $\eta' \to \pi^+\pi^-\gamma$.
In summary the Wess-Zumino-Witten Lagrangian already determines the triangle anomaly sector via A and the box anomaly sector via B.

2.4.3 MATRIX ELEMENT AND RADIATIVE DECAY RATE

Following the presentation of [17], the matrix element describing the decay $\eta'(p) \to \pi^+(p_+)\pi^-(p_-)\gamma(k)$ can be defined in terms of the pion vector form factor $F_V(s_{\pi\pi})$, with $s_{\pi\pi} = m^2(\pi^+\pi^-) = q^2$ ($q^\mu = p_+^\mu + p_-^\mu$), the invariant mass squared of $\pi^+\pi^-$.
$F_V(s_{\pi\pi})$, which describes the reaction $e^+e^- \to \pi^+\pi^-$, is defined by the current matrix element

$$\left\langle \pi^+(p_+)\pi^-(p_-)\right| \mathcal{V}^\mu \left|0\right\rangle = e(p_+ - p_-)^\mu F_V(s_{\pi\pi}), \tag{29}$$

where $e > 0$ is the unit electric charge and the current $\mathcal{V}^\mu = -\delta\mathcal{L}_{int}/\delta A_\mu$, with A_μ being the photon field.

Now one can write the matrix element, in the P-wave approximation [18], for the radiative decay $\eta' \to \pi^+\pi^-\gamma$ as

$$\left\langle \pi^+(p_+)\pi^-(p_-)\right| \mathcal{V}_\mu \left|\eta'(p)\right\rangle = \varepsilon_{\mu\nu\alpha\beta}\ p^\nu p_+^\alpha p_-^\beta f_1(s_{\pi\pi}), \tag{30}$$

where $\varepsilon_{\mu\nu\alpha\beta}$ is defined such that $\varepsilon_{0123} = +1$. The corresponding differential decay rate is given by

$$\frac{d\Gamma(\eta' \to \pi^+\pi^-\gamma)}{d\sqrt{s_{\pi\pi}}} = |f_1(s_{\pi\pi})|^2 \Gamma_1(s_{\pi\pi}), \tag{31}$$

where the function

$$\Gamma_1(s_{\pi\pi}) = \frac{4}{3}\left(\frac{m_{\eta'}^2 - s_{\pi\pi}}{16\pi m_{\eta'}}\sqrt{s_{\pi\pi} - 4m_\pi^2}\right)^3, \tag{32}$$

has the phase-space terms multiplied by kinematic factors of the squared magnitude of the simplest guage-invariant matrix element, with m_π and $m_{\eta'}$ denoting the mass of the pion and the η', respectively.

Final-State Interactions

All elastic pion-pion ($\pi\pi$) interactions are determined by the Omnès function $\Omega(s_{\pi\pi})$ which for pion pairs with relative angular momentum $L = 1$ is given by [17]

$$\Omega(s_{\pi\pi}) = \exp\left\{\frac{s_{\pi\pi}}{\pi}\int_{4m_\pi^2}^{\infty} dx \frac{\delta_1(s_{\pi\pi})}{x(x - s_{\pi\pi} - i\varepsilon)}\right\}, \tag{33}$$

where $\delta_1(s_{\pi\pi})$ denotes the pion-pion P-wave phase shift. The physics of the ρ-meson is encoded in the phase shift in a model-independent way.

The Omnès function can be used to express $F_V(s_{\pi\pi})$ as follows

$$F_V(s_{\pi\pi}) = R(s_{\pi\pi})\Omega(s_{\pi\pi}). \tag{34}$$

The function $R(s)$ is a real linear polynomial demonstrated to be sufficient for the vector form factor in the radiative decay of η [19, 20], similar to that of η'.

Relating $f_1(s_{\pi\pi})$ to $F_V(s_{\pi\pi})$, we can write Eqn. 31 as

$$\frac{d\Gamma(\eta' \to \pi^+\pi^-\gamma)}{d\sqrt{s_{\pi\pi}}} = |AP(s_{\pi\pi})F_V(s_{\pi\pi})|^2 \Gamma_1(s_{\pi\pi}), \tag{35}$$

where the normalization parameter A has the dimension of mass^{-3} and the function $P(s_{\pi\pi})$ is a process-specific part that can be treated perturbatively in the frame of χPT.
A Taylor expansion around $s_{\pi\pi} = 0$ gives

$$P(s_{\pi\pi}) = 1 + \alpha \cdot s_{\pi\pi} + \beta \cdot s_{\pi\pi}^2 + O(s_{\pi\pi}) \tag{36}$$

The parameters α and β allow insights into the physics underlying the radiative decay process. α is related to the box anomaly while β of the quadratic term can approximate to a very good extend the left-hand cut induced by $a_2(1320)$ tensor-meson (see FIG. 8) in the physical decay region [21].

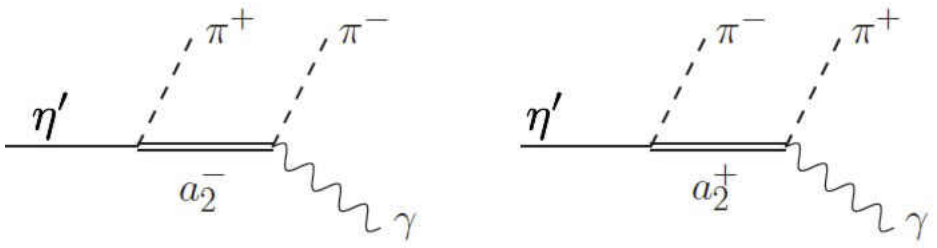

FIG. 8. Tree-level contributions of the $a_2(1320)$ resonance to $\eta' \to \pi^+\pi^-\gamma$ in the s- (left) and u-channel (right).

However, the expressions given so far ignore the contribution from the ω-meson, which

can also decay into the $\pi^+\pi^-$ final state via isospin-violating interactions. The ω-resonance is very narrow and close in mass to the ρ, the dominant resonant enhancement of the $\pi\pi$ P-wave amplitude. The inclusion of this mechanism, often named $\rho - \omega$ mixing, is essential for an accurate description of the vector form factor $F_V(s_{\pi\pi})$. For this work, experimental values for $F_V(s_{\pi\pi})$ (with this mechanism included) given in [22] was used. The contribution of ω is shown diagramatically in FIG. 9.

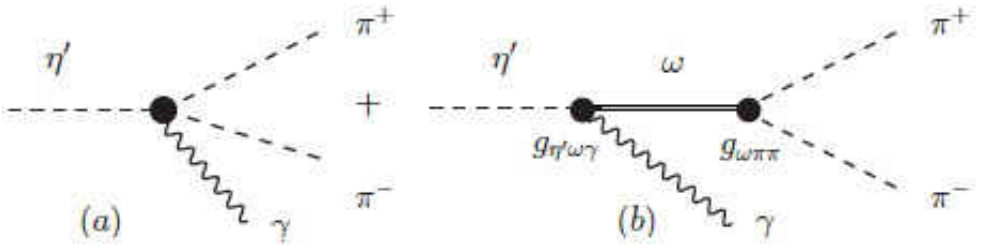

FIG. 9. Diagrams contributing to the decay $\eta' \to \pi^+\pi^-\gamma$. The pions from both diagrams undergo final-state interactions that are not shown explicitly. Source [17].

CHAPTER 3

CEBAF AND THE CLAS DETECTOR AT THOMAS JEFFERSON NATIONAL ACCELERATOR FACILITY

The g11 experiment that provided data for this analysis was conducted at Thomas Jefferson National Accelerator Facility (TJNAF, FIG. 10), located in Newport News, Virgina. It consists of four experimental halls, A, B, C, D, and the Continuous Electron Beam Accelerator Facility,[23] (CEBAF, FIG. 11).

The g11 data was collected with the CEBAF Large Acceptance Spectrometer (CLAS) in hall B, using CEBAF. The experiment ran between May 17th and July 29th 2004 as part of the E04-021 experiment *Spectroscopy of Excited Baryons with CLAS: Search for Ground and First Excited States*, with the primary purpose of a high-statistic search for the exotic Θ^+ pentaquark state [24].

The run conditions for g11 included a tagged photon beam (up to 4.016 GeV) incident on a 40 cm long (and 4 cm diameter) liquid Hydrogen target. The average current during the g11 run was I =65 nA, leading to total intergrated luminosity was on the order of 80 pb^{-1}. The CLAS detector was used to record multi-particle final states over a wide angular range of approximately 60% of the full 4π solid angle. For the g11 run an important addition to CLAS was a new Start Counter. It measures the production time of each track individually, allowing a tagged photon flux of at least 5×10^7 photons/second [25]. The experimental run resulted in roughly 20 billion triggers stored as 21 TB of raw data.

This chapter will describe the CEBAF accelerator, the experimental apparatus and setup for the g11 experiment, the Hall B photon tagger, the CLAS detector, and its data acquisition system.

FIG. 10. Aerial view of Jefferson Laboratory (JLAB) facing east. Image Source: [26]

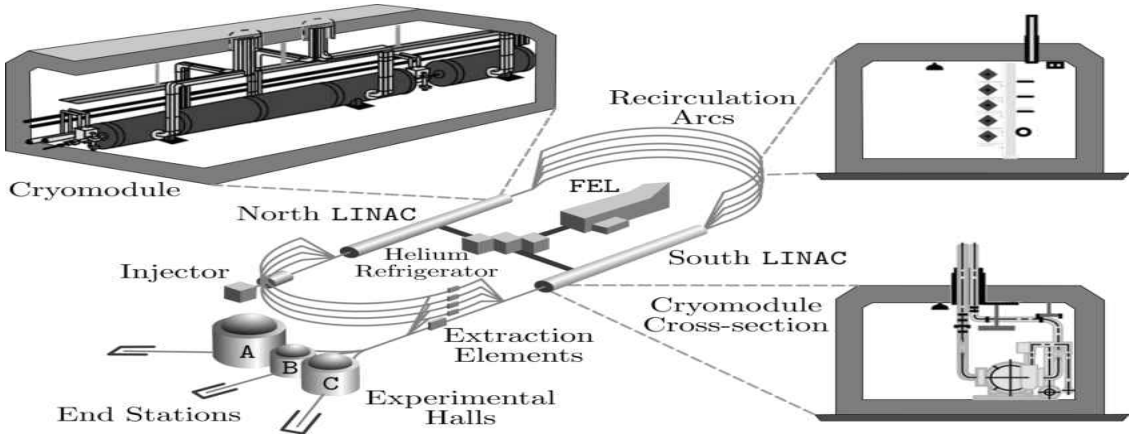

FIG. 11. The Continuous Electron Beam Accelerator Facility (CEBAF) at Jefferson Laboratory (JLAB) showing cross-sections of the linear accelerator (LINAC) halls and the recirculation arcs. Also depicted are the Free Electron Laser (FEL) and the helium refrigerator and distribution facility. Image Source:[23]

3.1 CONTINUOUS ELECTRON BEAM ACCELERATOR FACILITY

The main research unit of JLAB is the Continuous Electron Beam Accelerator Facility (CEBAF). It utilizes superconducting radio-frequency (SRF) cavities to accelerate electrons and provide a continuous wave beam with up to 75% polarization to all experimental halls simultaneously. During the g11 experiment the maximum energy of the beam was almost 6 GeV. Presently, CEBAF is upgraded to 12 GeV and now has a fourth experimental hall, Hall D.

In order to attain the running conditions described in Table 3, during the g11 run, CEBAF used a circularly polarized laser incident on GaAs photocathode to produce a highly polarized electron beam. Each diode laser, of which there are 3 in total, produce pulses which are timed such that each of the 3 experimental halls receives electron bunches (about 90 μm in length) every 2 ns. The electrons are accelerated to 100 keV by an electrostatic accelerator and then an optical chopper improves the separation of the bunches before they are accelerated further by two 1/4 SRF cavities to 62 MeV [28]. Standing waves established inside the Nb SRF cavity provide an acceleration gradient to the electron bunches passing through. Keeping the waves in phase with the electron bunches result in a continuous positive electric force on each bunch as it passed through a cavity, see FIG. 12.

TABLE 3. Operating specifications of 6-GeV CEBAF at JLAB. Table source:[27]

E_{min}	0.6 GeV
E_{max}	6.0 GeV
I_{max}	200 μA
Polarization	$> 75\%$
Geometric emittance	$< 10^9$ m rad
Momentum Spread	10^{-5}
Average currents (Halls A and C)	1-150μA
Average currents (Hall B)	1-100nA
Bunch charge	$<$ pC
Repetition rate	499 MHz/hall
Beam size (rms transverse)	~ 80 μm
Bunch length (rms)	300 fs, 90 μm
Energy spread	2.5 x 10^5
Beam power	$<$ MW
Beam loss	$<\mu$A
Number of passes	5
Number of accelerating cavities	338
Fundamental mode frequency	1947 MHz
Accelerating cavity effective length	0.5m
Cells/cavity	5
Average Q_0	4.0 x 10^9
Implemented Q_{ext}	5.6 x 10^6
Cavity impedance (r/Q)	980 Ω
Average cavity accelerating gradient	7.5 MV/m
RF power	$<$ 3.5 kW/cavity
Amplitude control	1.00 x 10^{-4} rms
Phase control	0.1° rms
Cavity operating temperature	2.08 K
Heat load @ 2 K	$<$ 9 W/cavity
Liquefier 2 k cooling power	5kW
Liquefier operating power	5MW

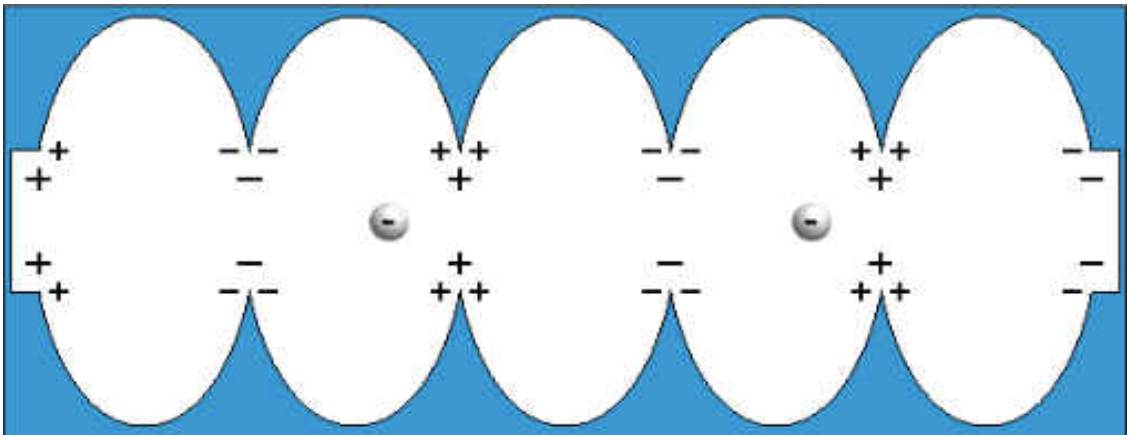

FIG. 12. Accelerating Cavity Diagram. Electron clusters experience a continuous acceleration due to a standing electromagnetic wave indicated by the positive and negative signs along the inner wall.

The beam of electrons is finally sent through a recirculating beamline, consisting of two linear accelerator (LINACs) located along the straightaways of a 7/8 mile racetrack course and connected by two 180° magnetic-dipole bending arcs (see FIG. 11) with a radius of 80 meters. Each LINAC contains 168 SRF Nb cavities (see FIG. 13). Each cavity is submerged in liquid Helium and cooled to -271°C, temperature at which Nb becomes superconducting. There are twenty cryogenic modules in total, each containing eight superconducting niobium cavities.

The beam can pass through the pair of LINACs up to five times to reach the maximum beam energy of 5.6 GeV, with a maximum current of 180 μA before being delivered to an experimental hall. Each LINAC has the capacity of accelerating the beam by up to 600 MeV giving approximately 1.2 GeV per pass. Each hall can control the beam energy to extract after a given number of passes (no greater than five), however the fifth pass can be sent to all three halls simultaneously, but it cannot provide a single low energy beam to two halls at the same time. Because of the importance of a stable and constant beam energy for nuclear physics experiments, about 2200 quadrupole and dipole magnets are placed in the accelerator tunnels to steer and focus the beam.

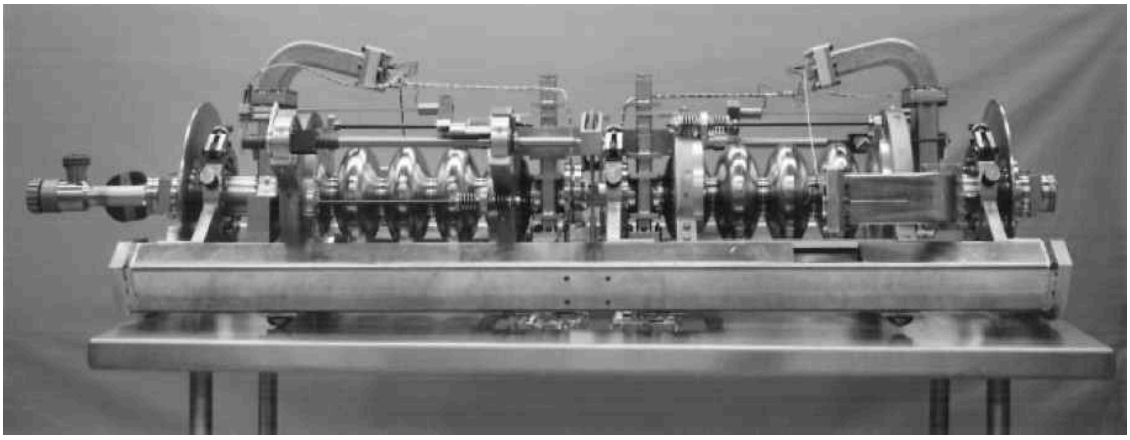

FIG. 13. A pair of CEBAF's superconducting niobium cavities. Its elliptical components are perpendicular to the beamline pipe and are covered by some supporting tools. Image Source: [23]

3.2 THE BREMSSTRAHLUNG PHOTON TAGGER

The hall B tagging system converts the CEBAF electrom beam into a *real photon* beam by means of bremsstrahlung radiation, when the electron beam passes through a radiator. The tagging system also obtains energy, and timing information about these *real photons*. The important parts of the photon tagging system are the radiator and magnetic spectrometer.

3.2.1 THE BREMSSTRAHLUNG RADIATOR

As a bremsstrahlung radiator, the g11 experiment used a gold (Au) foil of 10^{-4} radiation length. Gold is typically used as radiator since it has a high atomic number to help reduce contamination of photons produced by electron-electron scattering. The choice of gold serves two purposes, first to maximize the probability of the electron-nucleus interaction given that the bremsstrahlung cross section is proportional to Z^2, and second to minimize the number of interaction centers such that each electron interacts once, producing only one photon. Electrons of the incident beam interact with the electromagnetic field of nuclei in the thin radiator and emits real photons. After passing through the radiator, the beam becomes a mixture of photons and electrons that did not interact with the radiator as well as recoil electrons.

3.2.2 TAGGING SPECTROMETER

After the interaction in the radiator, the mixed beam then travels into a magnetic spectrometer (the"tagger") that introduces a dipole magnetic field which sweeps the electrons out of the electron-photon beam to obtain a clean photon beam. Electrons that did not interact with the radiator are bent by the field towards the beam dump. Meanwhile those electrons that interacted and lost a part of their energy are directed toward two hodoscope planes, each made of an overlapping array of scintillators to detect these energy-degraded electrons. The photon beam is not affected by the tagger magnet and continues straight to the liquid hydrogen target.

The first scintillator plane, or E-plane (Figs. 15, and 16), is used to determine the energy of the recoiling electrons. It consists of 384 narrow paddles (the"E-counters") that are 20 cm long, 4 mm thick and from 6 to 18 mm wide with a photomultiplier tube (`PMT`) on one end. The overlapping configuration of the paddles, increases the number of logical photon energy bins to 767. Struck paddles can provide photon energy resolution on the order of 0.1% of the incident electron beam energy. The trajectory of a charged particle in the magnetic field is governed by the equation

$$p = qrB \text{ (if } \vec{p} \perp \vec{B}) \tag{37}$$

where p is the particle's momentum, q is the particle's charge, r is the particle's radius of curvature and B is the magnetic field the particle traverses. If one knows the paddle an electron hits and the radius of curvature, then one can calculate the momentum of the electron. Hence the energy of the photon can be calculated by

$$E_\gamma = E_0 - E_e \tag{38}$$

where E_0 is the energy of the incident electron, E_e is the energy of the recoil electron and E_γ is the energy of the emitted photon.

The second scintillator plane, or T-plane, located 20 cm behind the E-plane is used for accurate timing measurements of the recoiling electrons. It comprises of two groups of scintillator paddles ("T-counters") that are each 2 cm thick with a `PMT` on each end. The thickness of these paddles allow for a timing resolution of 110 ps, providing the timing presicion needed to find the coincidence with detector particles triggerred by a given photon. The T-counters have different lengths and width to compensate for the $\frac{1}{E_\gamma}$ profile of the bremsstrahlung cross section thereby keeping the counting rate the same in both groups.

The first group has 19 counters that covers a photon energy range from 75-95% of the incident electron beam energy while the second has 42 counters that covers a photon energy range of 20-75% of the incident electron beam energy. The tagger can therefore tag photons of energies from 20 to 95% of the incident electron beam energy.

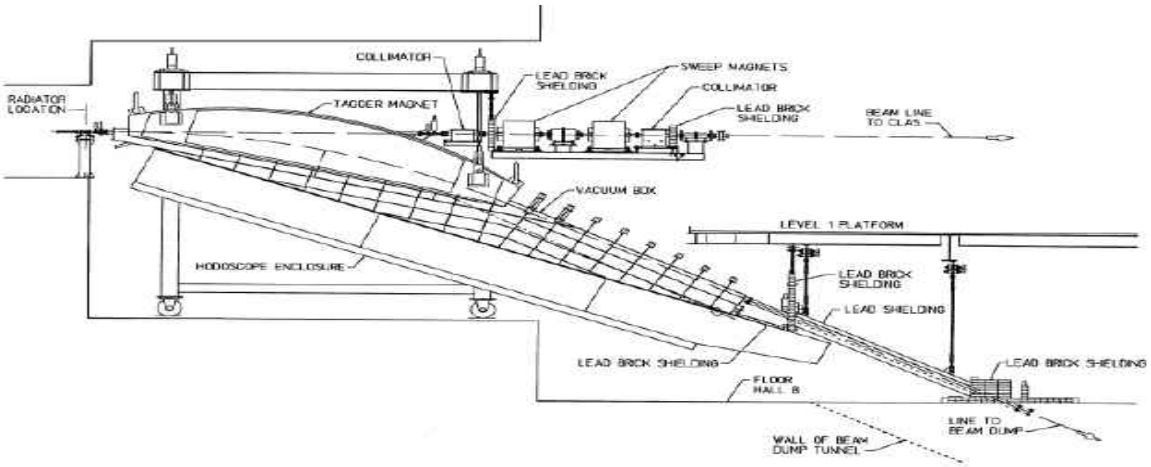

FIG. 14. A schematic of the hall B photon tagging system. Important components include the radiator, the hodoscope, and the collimator. Image source: [29].

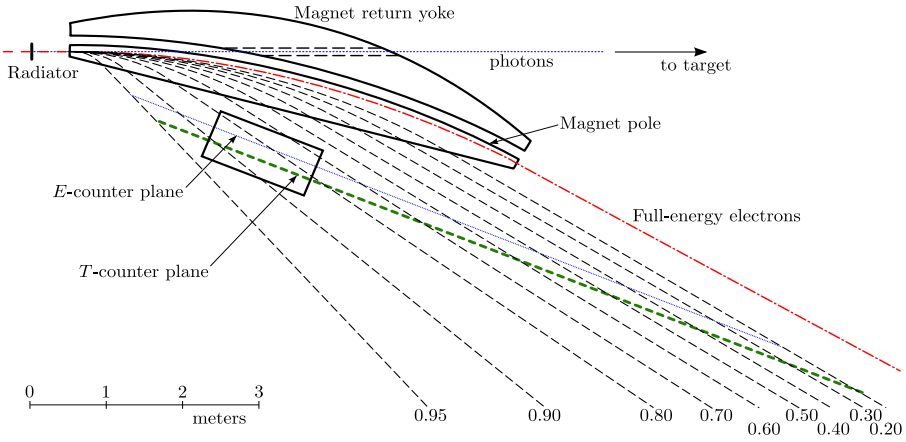

FIG. 15. Scale drawing of the photon tagger system. The rectangular area around the E- and T-counter planes outlines the expanded view shown in FIG. 16.

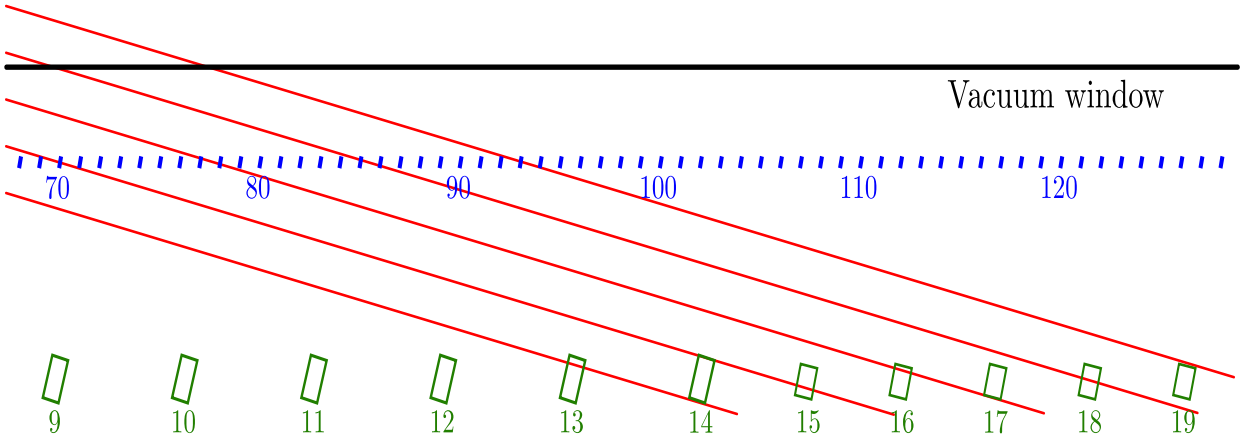

FIG. 16. Scale drawing of the E-counters (blue) and the T-counters (green) showing examples of recoiled electrons (red lines) entering from the upper left.

The signals from the scintillator paddles were read out by the PMTs located at their ends. The signals from each E-counter PMT are passed through a discriminator and then forwarded to a multi-hit time-to-digital converter (TDC) to record the E-counter timing information. The PMT signal from each T-counter are sent to a constant fraction discriminator (CFD). The output signals form the CFD are then sent to the *Master OR* (MOR) and an array of FASTBUS TDCs. Output from the TDC is stored in raw data bank to preserve precise and accurate information for each T-plane hit as well as the total number of hits recorded in the targer. The MOR provides the signal that the photon has been tagged for the CLAS Level 1 trigger.

The timing information are used during data analysis to get the hit patterns and to find the timing coincidence between the E- and T-counters. The timing resolution of the Hall B taggging system is good enough to identify which RF beam bucket each photon is associated with. The most accurate timing information available in the entire g11 experiment was the RF signal obtained from the accelerator. The time at which all the final state particles produced in the interaction were at the same piont in space (referred to as the event vertex time), was calculated by temporally propagating the RF time from the radiator to piont in space where interaction occured. A schematic of the Hall B photon tagger logic setup is shown in FIG. 17.

3.2.3 COLLIMATORS

The photon beam is further defined by passing through two collimators and sweeping magnets before it reaches the CLAS target. The collimators trim the beam halos while the sweeping magnets placed between them remove the electrons created during the secondary interactions of photons with the first collimator.

More detailed information on the hall B tagging system and DAQ of the tagger system can be found in [30].

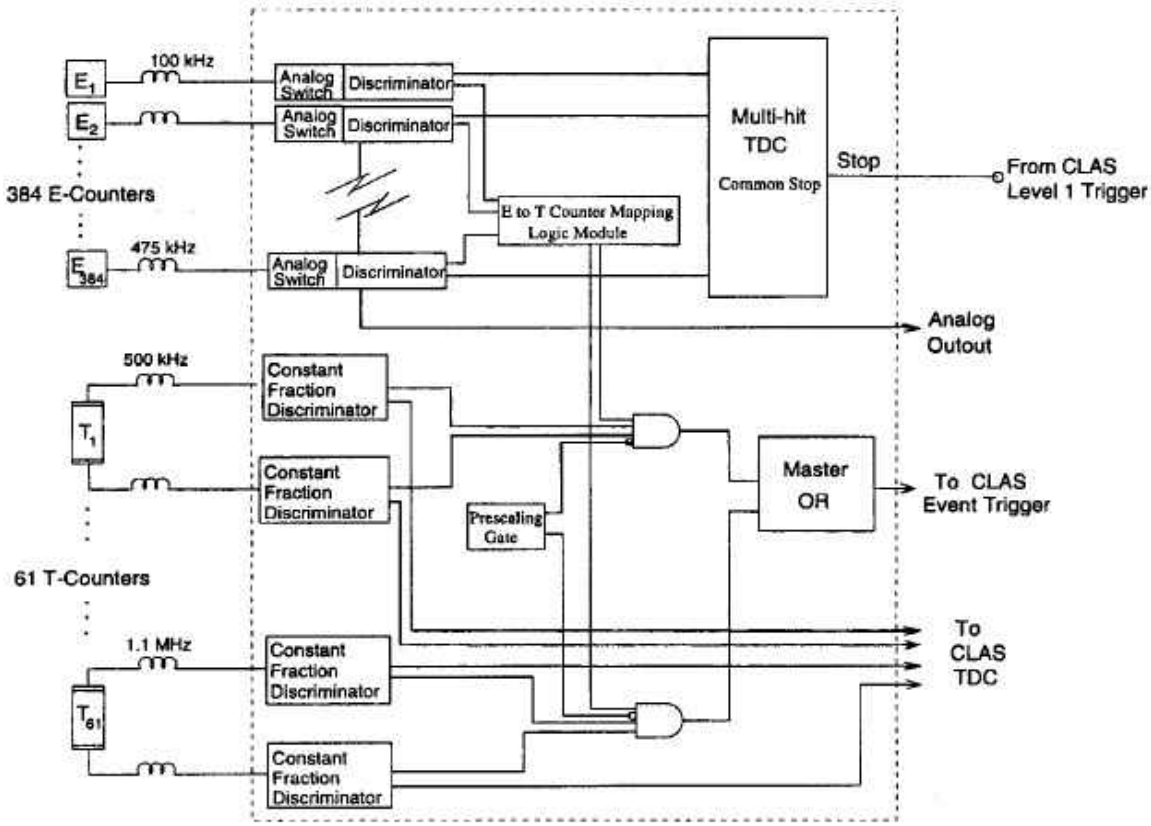

FIG. 17. Schematic diagram of the Hall B photon tagger logic system. Image source: [29].

3.3 HALL-B BEAMLINE DEVICES

There were several beamline devices used in Hall B before and after the CLAS detector (FIG. 18) during the g11 run to scan important details of the electron beam before being converted into a photon beam and the details of the photon beam prior and after hitting the liquid Hydrogen target. These included three nA beam position monitors (BPMs), with a resulotion better than 100μm, to monitor the position and current of the beam. The harp, located upstream from the center of CLAS was installed to measure the beam profile. The transverse width of the beam profile was typically less than 200μm during the entire run period.

As noticed in the previous paragraph, two types of devices measured the electron beam position. Two beam position monitors (BPMs) placed before the tagger represent the first type of device. The position monitors use three radiofrequency cavities to measure the intensity of the electron beam and its transverse location. This is a non-invasive process and the information obtained is used as feedback for the steering mechanism. The Harp Beam Profile Monitor is the second type of device which also measures the electron beam dispersion. The harp devices consist of fine tungsten and iron wires that can be passed through the beam at specific orientations and collect scattered electrons with a photomultiplier tube. This procedure measures the horizontal (x) and vertical (y) profile of the electron beam and is performed after any downtime or change in the beam. The beam position is adjusted such that more than 99% of the electron beam goes through the radiator. This procedure was conducted only when the drift-chambers and DAQ were turned off, because of its invasive nature.

Downstream devices, such as the Total Absorption Shower Counter (TASC) located at the end of the beamline, the Pair Spectrometer (PS) and the Pair Counter (PC), which were both located between the tagger and the target, measured the photon flux (see FIG. 19). The TASC consisted of four lead glass blocks of $\sim$ 17 radiation lengths, each coupled to a photo-multiplier tube (PMT). The TASC had close to 100% photon detection efficiency only if the beam current was less than 100 pA [30, 31]. The Tagging Ratio used to calibrate the tagger and measure the g11 flux was obtained from the ratio of electrons detected in the photon tagger (see Sec. 3.2) to that of photons detected in the TASC. The tagging ratio indicates which fraction of the tagged photons actually hit the CLAS target.

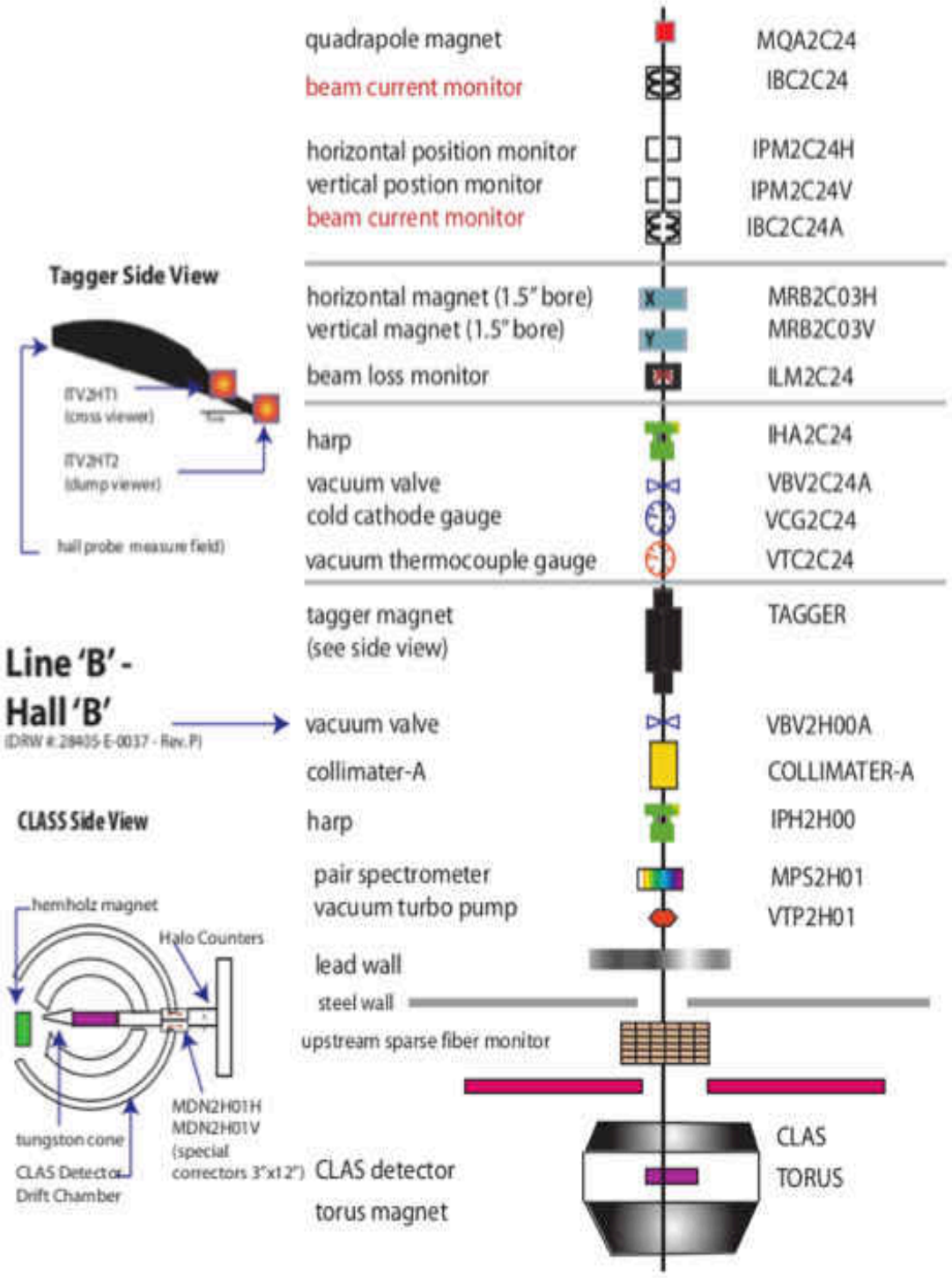

FIG. 18. Beamline and components of CLAS. Image Source [26]

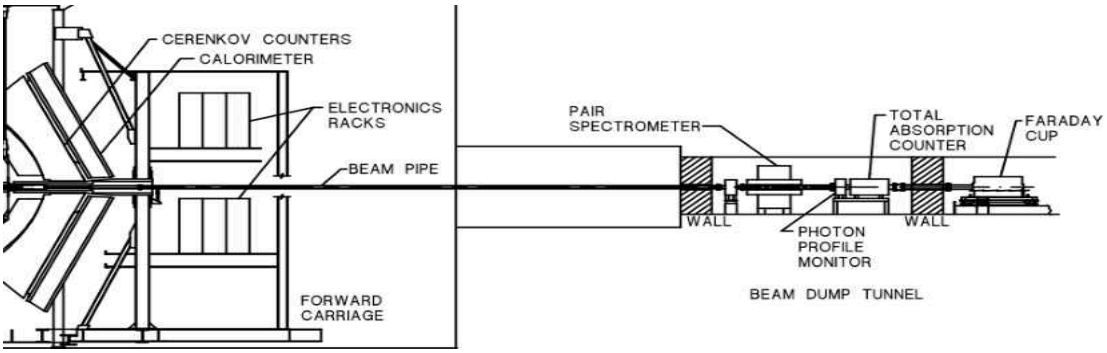

FIG. 19. Beamline components in g11 after `CLAS`

3.4 CEBAF LARGE ACCEPTANCE SPECTROMETER (CLAS)

The CEBAF Large Acceptance Spectrometer, CLAS, shown in FIG. 20, is a large acceptance (almost 4π coverage) detector installed in hall B, at JLAB. The CLAS detector is comprised of various detector subsystems. In the g11 experiment, this detector was used to measure momenta and angles of outgoing charged particles after the photon beam interaction with the liquid hydrogen target. The detector subsystems are layed out in an onion-like pattern (surrounding the target) and are combined around a toriodal magnet consisting of six superconducting coils that split CLAS into six sectors. The direction of the field of the toroidal magnet is azimuthal making charged particles conserve their azimuthal angle along their trajectory, except near the coils. The geometry of the toroidal magnetic field guided the particles that allowed for a simplified reconstruction algorithm to determine the particles' momenta, see Eqn. 37. Each sector consists of a scintillator start counter (SC) Sec. 3.4.2, three layers of drift chambers (DC) Sec. 3.4.4, a layer of scintillator "time-of-flight" counters (TOF) Sec. 3.4.5, a gas Cherenkov counter (CC) Sec. 3.4.6 and an electromagnetic calorimeter (EC) Sec. 3.4.7. The following subsections describe individual subsystems in more detail.

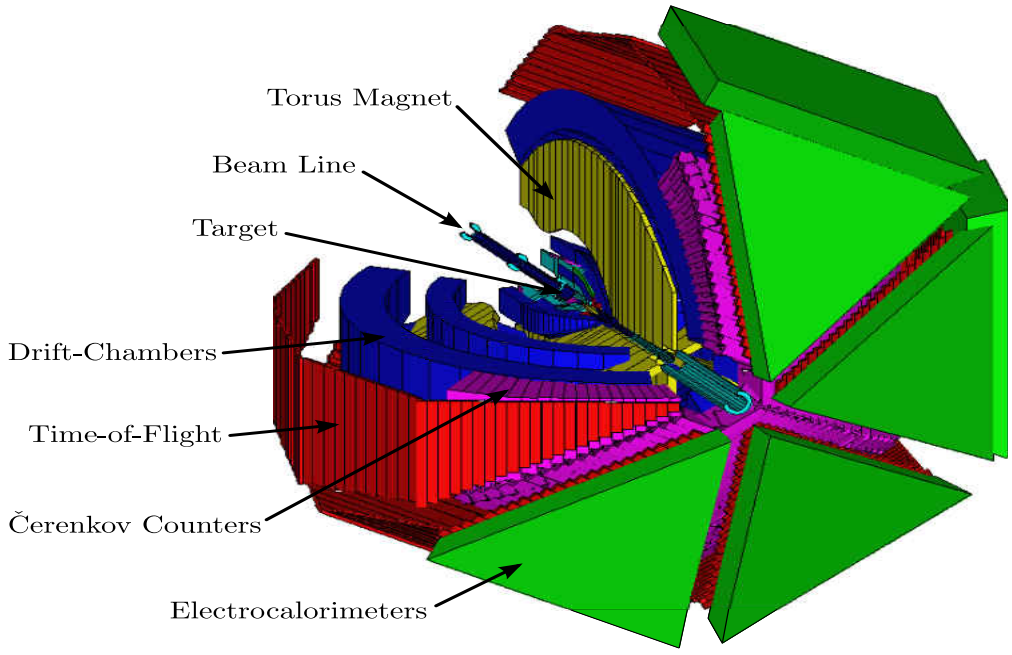

FIG. 20. 3D view of the CLAS detector [32] with subsystems identified. The detector is approximately 8 meters in diameter.

FIG. 21. The coils of the CLAS toroidal magnet prior to installation of the rest of the detector. Image Source [27]

3.4.1 CRYOGENIC HYDROGEN TARGET

The geometry of the cryotarget cell used by g11 was a cylindrical 0.127 μm thick Kapton chamber with dimensions of 40 cm in length and 2 cm in radius shown in FIG. 23. The target cell design shown in FIGs 22 and 23 had been used in several experiments and can carry different materials, such as helium, deuterium and hydrogen. The material used for the g11 experiment was liquid hydrogen (ℓH_2). The temperature and pressure inside the cell are continuously monitored on an hourly basis and used to determine the density and thickness of the liquid hydrogen. The target density averaged over all $g11$ runs is 0.07177 g/cm^3, the target density is an important parameter needed for cross section measurements. The target was positioned at the center of CLAS.

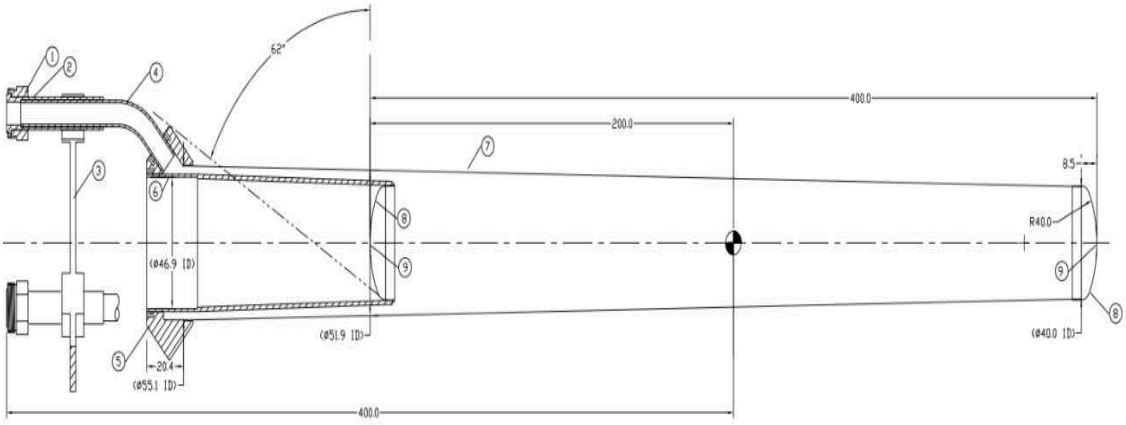

FIG. 22. Blueprint schematic of the conical Kapton target cell used for g11.

FIG. 23. A diagram of g11 cryotarget with L=40cm and R=2cm.

Item	Value
Length	40.0 cm
Radius	2.00 cm
Temperature	19.3 K
Pressure	1122 mBar
Density	0.07177 g/cm^3

TABLE 4. Specifications of the cryogenic hydrogen target

3.4.2 START COUNTER

The start counter, Figs. 24 and 25, was specifically designed to achieve full acceptance coverage for the 40 cm long cryogenic liquid hydrogen target. By detecting outgoing particles, the start counter measured the interaction time of incident photons in the target. The counter is a PMT-instrumented scintillator detector with a hexagonal shape that surrounded the target. It is segmented into six sectors corresponding to those of CLAS. Each side consists of four 2.2 mm thick independently-instrumented scintillator strips for a total of 24 channels. Each strip is connected to a light guide which is subsequently linked to a PMT. The timing resolution achieved by the start counter is ∼400 ps and had a good efficiency. Information obtained from the start counter was used in the g11 Level 1 trigger. More information on the CLAS start counter can be found in [33].

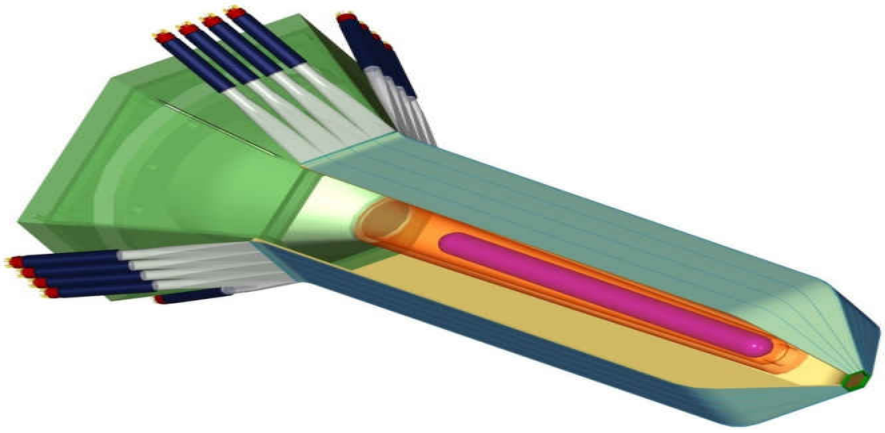

FIG. 24. Schematic view of CLAS start counter (ST) with the 40 cm long target cell (purple) at the center.

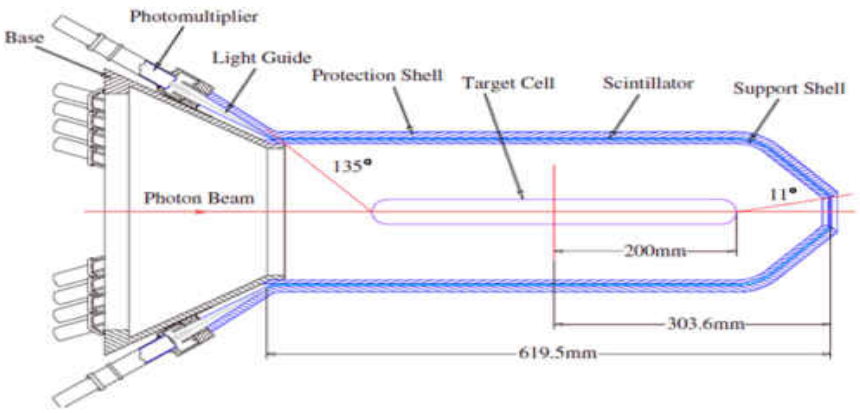

FIG. 25. Components of the ST and its angular coverage.

3.4.3 SUPERCONDUCTING TOROIDAL MAGNET

The most essential part of CLAS is the superconducting toroidal magnet. It consists of six kidney-shaped superconducting coils located between Region-1 and Region-3 of the DC and separated in the azimuthal direction by 60° around the beam line thereby seperating the whole detector into six independent sectors, see FIG. 26. FIG. 27 shows a map of the magnetic field strength. For the g11 experiment, the current in the magnet was limited to 1920 A, which was about half the maximum the magnet can support, to enhance the acceptance of negatively charged particles. Running at higher currents provides better momentum resolution but decreases the detector's acceptance for negatively charged particles. In its default configuaration, the field was such that positively charged particles are bent away from the beam pipe, while negatively charged particles bent toward the beam pipe. Knowing the strength and direction of the magnetic field and the trajectory of a particle using the DC, the particle momentum can be determined by use of Eqn. 37.

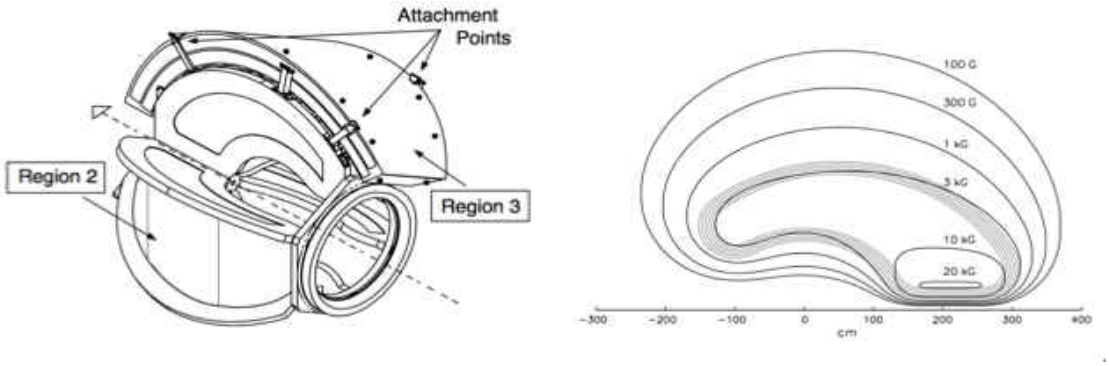

FIG. 26. Placement of the CLAS Superconducting Toroidal Magnet in relation to Region-1 and Region-3 (left). The contours of constant absolute magnetic field of the CLAS toroid in the midplane betweeen two of the coils(right).

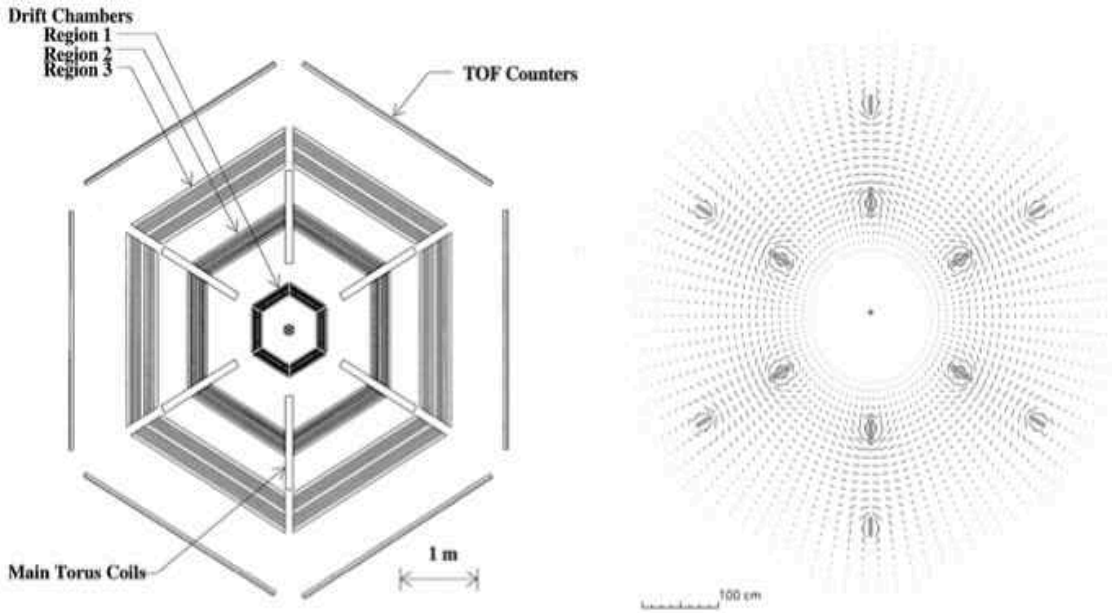

FIG. 27. Schematic cross-sectional view of the CLAS detector, perpendicular to the beam line (left). The azimuthal field vectors corresponding to the view in the left figure. The field is stronger between the coils(right). Image source: [27].

3.4.4 DRIFT CHAMBERS

The momentum of charged particles were measured by using the CLAS drift chambers DC (FIGs 20, 27) to track the particles as they traveled through the field generated by the superconducting toroidal magnet. They could track charged particles of energy higher than 200 MeV/c with polar angle resolution of 2-4 mrad and momentum resolution of 0.5 - 1%. In the g11 experiment, the coverage of the DC was $8^\circ < \theta < 142^\circ$, since the target was at the center of CLAS.

The drift chambers are arranged in three regions within each of the six sectors of the CLAS detector. The innermost region, Region 1 is closest to the target and is occupying a space where the magnetic field is weak since it is located between the torus coils and the beam line, see FIG. 26. The strongest magnetic field is experienced in Region 2 as it was mounted directly to the magnet's cryostats. Region 3, the outermost region is positioned outside of the magnet and is in an almost field-free zone, and measures the final trajectory of charged particles before the time-of-flight counters, Cerenkov counters and the electromagnetic calorimeters.

Each region of the DC spans the same polar angular range and consists of two superlayers, the *axial* and *stereo* layers of wires. Each superlayer contains six layers of hexagonal gold-plated aluminum alloy field wire cells (vertices of hexagon) of 140 μm diameter surrounding 20 μm gold-plated tungsten sense wires (center of hexagon). The first superlayer, the *axial* layer, measures the scattering angles and momenta of particles and its wires are strung parallel to the direction of the magnetic field. The second superlayer, the *stereo* layer, has wires tilted at a 6° angle with respect to the axial wires. Each DC system is filled with a 90% argon and 10% carbon-dioxide gas mixture. This mixture supports a high drift velocity of 0.04 m/μsec and rapid collection time which enhances momentum resolution. Intrinsically, the resolution provided is about 100μm. The sense wires are maintained at positive potential, while the field wires are maintained at a negative potential 50% lower than the positive value. As a charged particle passes through a cell and ionizes the gas electrons along its path, these electrons start to accelerate towards the sense wire due to the difference in potential.

Electrical signals from the sense wires go through preamplifiers, then to amplifier discriminator boards (ADBs), and finally to TDCs before being recorded in the data stream. More information on the CLAS DC system can be obtained from [34] and [35].

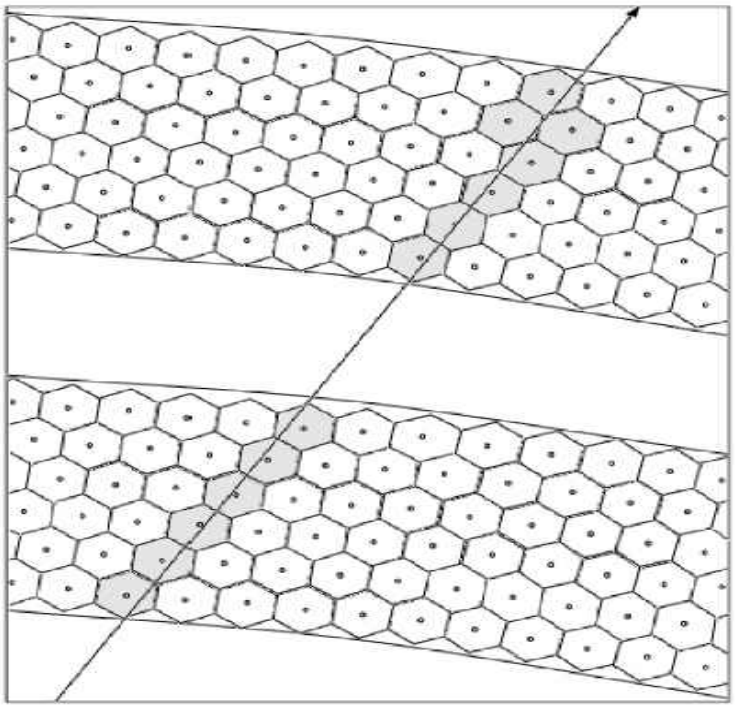

FIG. 28. Schematic of a section of drift chambers showing two superlayers. The wires are arranged in hexagonal pattern, the sense wires at the center and field wires at each corner. The arrow shows a charged particle's track with shadowed hexagons representing the hit cells.

3.4.5 TIME-OF-FLIGHT COUNTERS

The CLAS time-of-flight TOF subsystem is used to provide precise timing information of charged particles that traverse the CLAS detector to help determine the particle masses. The mass of a particle can be determined explicitly if we know its trajectory and timing measurement:

$$m = p\sqrt{(1-\beta^2)}/\beta \tag{39}$$

where

$$\beta = l_{sc}/(t_c \cdot c) \tag{40}$$

- l_{sc} is length of trajectory of particle to TOF
- t_c is the difference between the event radio-frequency (RF) corrected start and the time measured by the TOF
- c is the speed of light

In addition to particle identification, the TOF subsystem was also used in the level 1 trigger (see 3.5). Covering the outside shadow area of the torus coils, from 8° to 142°, in each sector of CLAS are segmented walls located approximately 4 m from CLAS center. The TOF subsystem is made of Bicron BC-408 organic plastic scintillation material. Each scintillator wall has four panels and a total of 57 scintillator paddles of different lengths and widths, see FIG. 29. The length of the paddles varies from 30 to 450 cm, the width is 15 or 22 cm, and the thickness is 5.08 cm. Photo-multiplier tubes (PMTs) are located at both ends of each scintillator paddle to read the signal. The timing resolution depends on the length of the bar and is within the range 150–200 ps. This level of resolution allows to distinguish between pions and protons up to a momentum of 2.5 GeV/c. The PMT signals are read out by ADCs and TDCs which are unevenly distributed at different angular regions the TOF system. Detailed information on the TOF system can be obtained from [36].

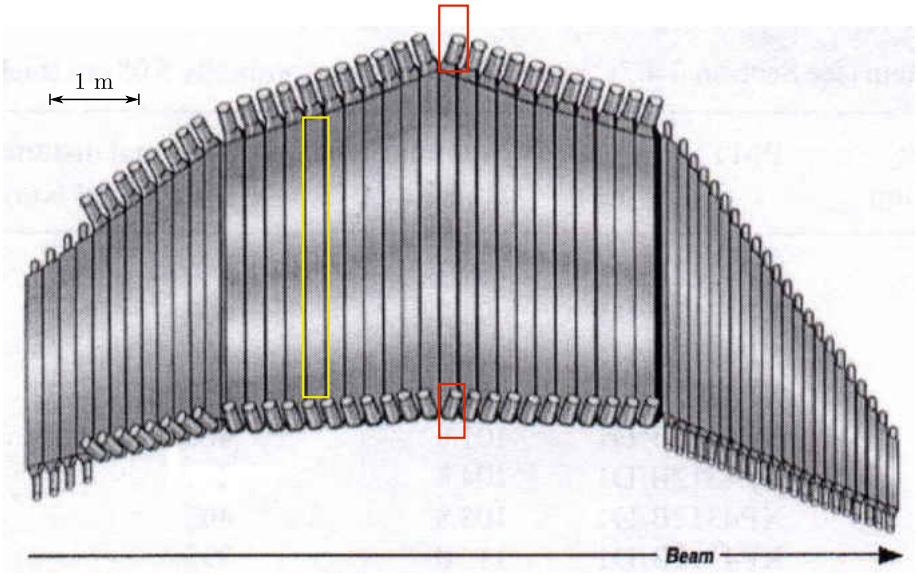

FIG. 29. Time-of-flight (TOF) paddles of one sector of CLAS. The four panels of scintillator paddles consist of 57 units of different length and width. PMT's are outlined in red while a scintillator paddle is outlined in yellow. Image Source: [37]

3.4.6 CHERENKOV COUNTERS

In CLAS, the gas Cherenkov counter (CC) is used to differentiate between electrons and negative pions for momenta below 2.5 GeV after having passsed through the drift chambers. The CC subsystem occupies the space between Region 3 of the DC and the TOF subsystem in the forward region. They are divided into 18 segments of θ (shown in FIG. 31a) covering polar angles 8° to 45° in each of the six CLAS sectors for g11, where tracks originated from the center.

When a charged particle traverses a medium with a velocity greater than the speed of light for that medium ($v > c/n$, where n is the refractive index), the dipoles of the molecules arrange themselves such that they are asymmetric along the particles path thereby creating a dipole field, see FIG. 30. The generated dipole field radiates the energy contained in this disturbance producing a coherent shockwave called Cherenkov radiation.

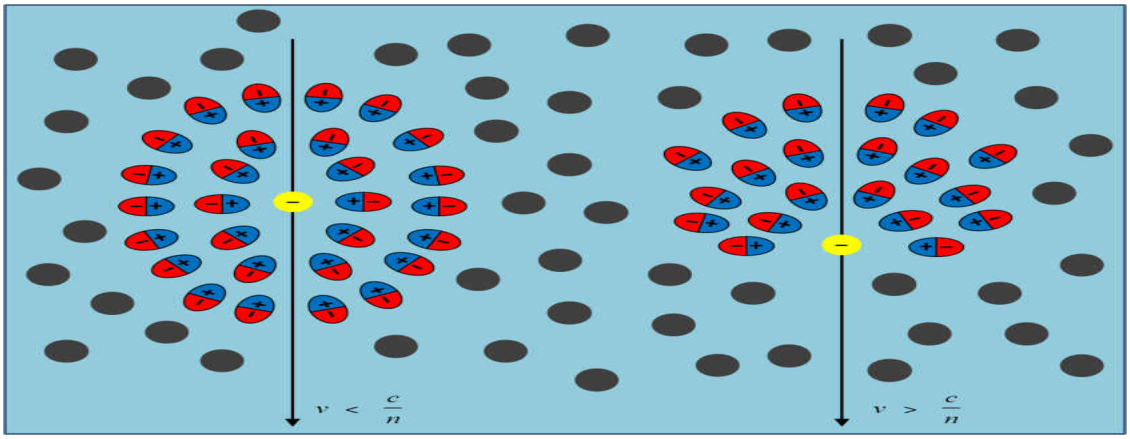

FIG. 30. Illustration of Cherenkov Radiation. Negative charged particle traveling through a medium with $v < c/n$ showing dipoles symmetrically arranged around particles path (left). Negative charged particle traveling through a medium with $v > c/n$ showing dipoles asymmetrically arranged around particles path given rise to dipole field (right).

The gas used in the CC for g11 is perfluorobutane (C_4F_{10}), chosen for its high index of refraction of 1.00153 producing a high yield of photons. The threshold energy for charged pion to produce Cherenkov radiation in C_4F_{10} is 2.7 GeV, while the threshold for electrons is 9.2 MeV. The optical element of CC subsystem constitutes an assembly of an elliptical and a hyperbolic mirror providing primary light focusing into a cone, a cylindrical mirror used to compensate for defects in the focusing, and a PMT used to count the number of photons in the light cone. To prevent the degradation of energy resolution, light-collecting cones and

the PMT's are placed in the areas obscured by the torus coils. More information on the CLAS Cherenkov detector can be found in [38]

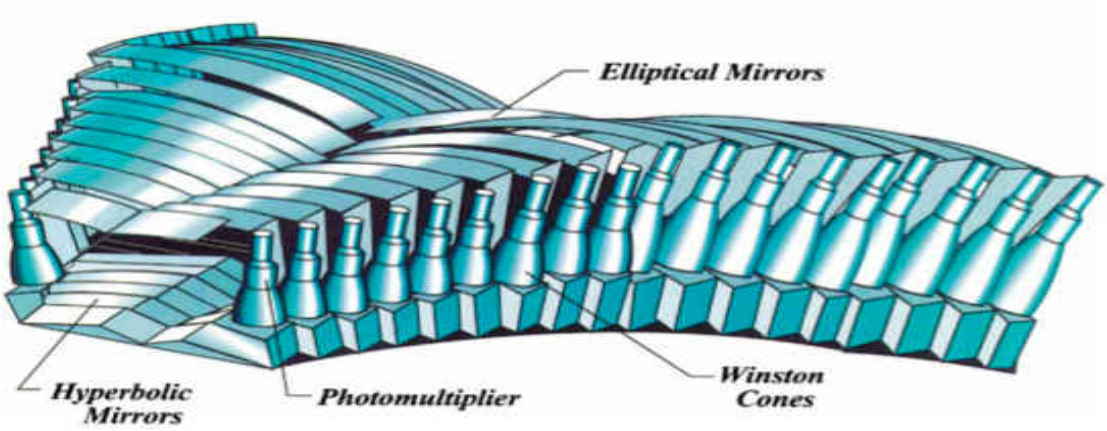

(a)

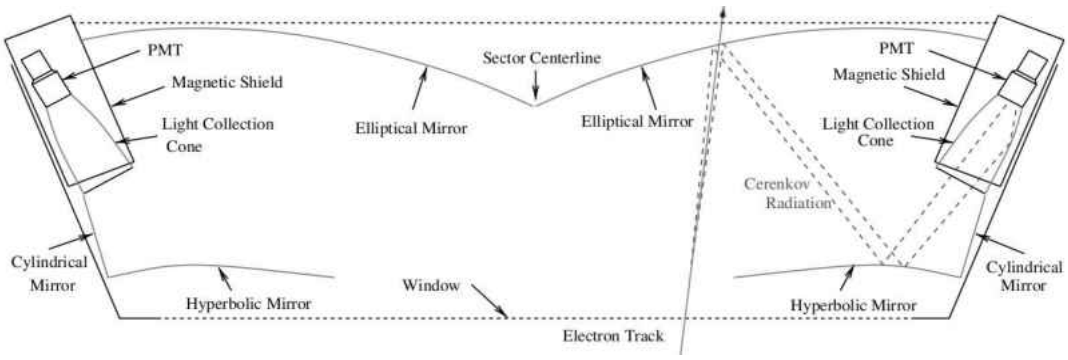

(b)

FIG. 31. Schematic of one CC showing the 18 symmetrical, mirrored segments of the CLAS CC (a). Diagram of one segment of the Cherenkov counters with a typical path of an electron entering from the bottom (b).

3.4.7 ELECTROMAGNETIC CALORIMETERS

The CLAS Electromagnetic Calorimeter (EC) was used to distinguish between electrons and pions as well as to detect neutral particles. Due to EC detection efficiencies, separation between photons and neutrons for momenta less than 2.5 GeV is done using time-of-flight measurements. Meanwhile discrimination between electrons and pions is optimal in the EC at momenta above 2.5 GeV where the pion rejection reaches its threshold in CC. The CLAS electromagnetic calorimeter (EC) [39], shown in FIG. 20 was designed with the following criteria;

- e/γ energy resolution $\sigma/E \leq 0.13/\sqrt{E(GeV)}$
- Position resolution $\delta r \approx 2cm$ *at* $1GeV$
- π/e rejection greater than 99% at $E \geq$1 GeV
- Fast ($<$ 100 ns) total energy sum for the event trigger
- Mass resolution for 2-photon decays $\delta m/m \leq 0.15$
- Neutron detection efficiency $>$ 50% for $E>$ 0.5 GeV
- Time-of-flight resolution $\approx$ 1 ns

The `EC` is located in the forward region and spans the same angles $8^\circ < \theta < 45^\circ$ as was the `CC`. The detector consists of alternating layers of scintillators sandwiched between lead (Pb) sheets. A configuration of lead to scintillator ratio of 0.24 was chosen so that roughly 1/3 of the showering particle's total energy is deposited in the scintillator. There are six equilateral triangular `EC` modules, one per sector, each a sandwich of 39 layers of 10 mm thick BC-412 scintillator followed by 2.2 mm thick lead sheet. Each scintillator is made of 36 strips parallel to one of the sides of triangle so that the orientation of the strips is rotated by 120° in each successive layer. This leads to three views, labeled u, v and w with each contaning 13 layers which are further subdivided into inner and outer stacks. The `CLAS EC` is subdivided into two stacks, *inner* and *outer*. The *inner* stack comprises of 8 *logical* layers while the *outer* stack comprises 5 *logical* layers. Such a configuration gives information on a hit location; the time and the energy are then calculated by taking account of the path length from the hit to the readout.

A final-state photon is identified in the `EC` if no charged tracks was associated with an energy deposition and also the velocity, β, of the particle is higher than 0.9c. Particles with $\beta <$ 0.9c are neutron candidates. The difference in energy deposit between the *inner* and *outer* layers provides separation of electrons from pions in the reconstructed data for energies less than 2.8 GeV. For energies greater than 2.8 GeV, identification of pions and electrons are obtained by comparing the energy deposited in the `EC` with the momentum determined from the `DC`.

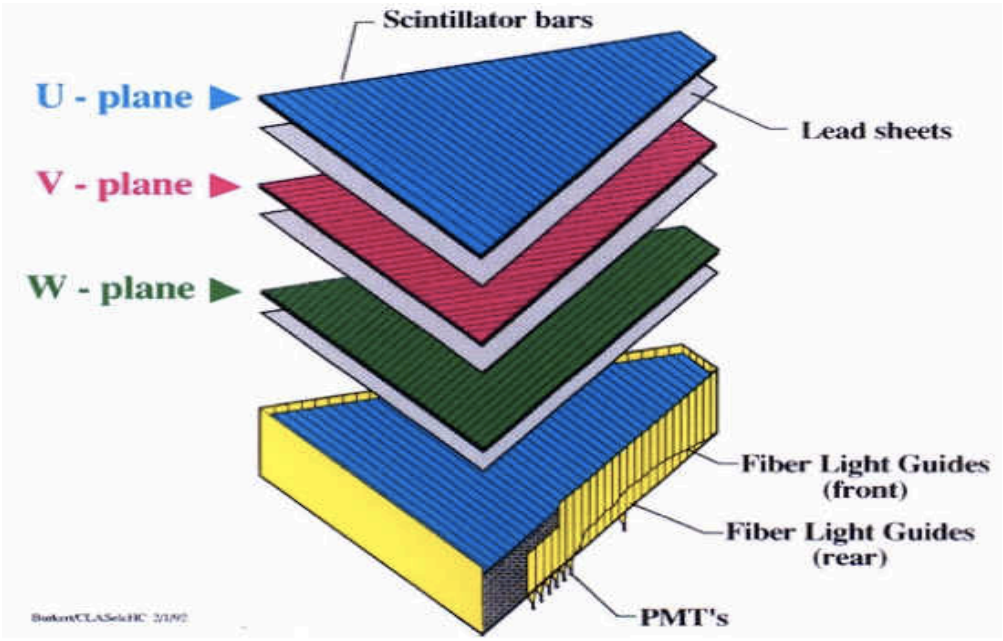

(a)

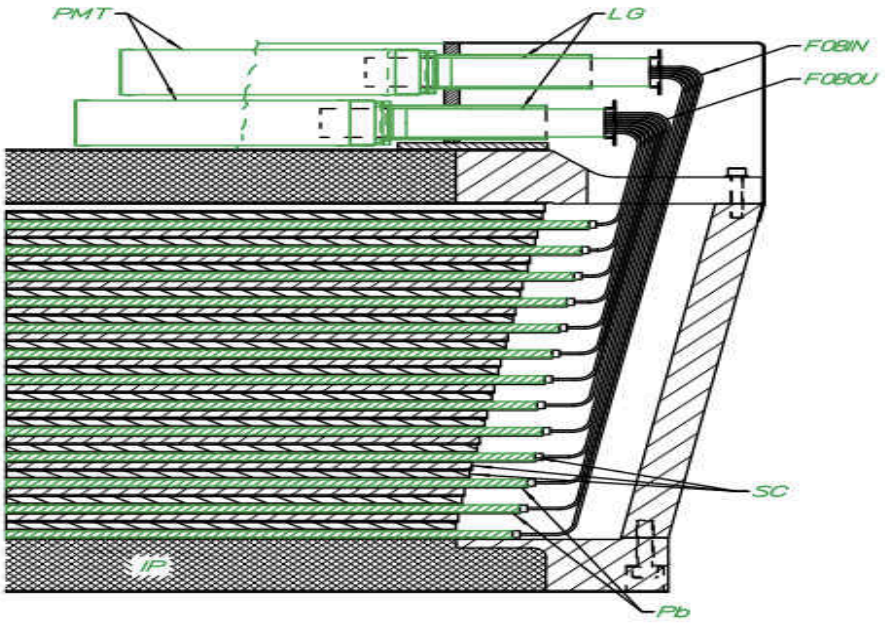

(b)

FIG. 32. Schematic view of one sector of the forward electromagnetic calorimeter (EC) showing the three planes (u, v, w) of scintillator-lead pairs (a). Side view of one plane of the forward EC showing 13 logical layers, PMT's and light guides (b). Image Source: [27].

3.5 TRIGGERING AND DATA ACQUISITION

Each subsystem of CLAS is setup with its own electronics package to actively run and monitor signals created in the component. Signals from the various subsystems are managed by the Trigger and Data Acquisition (DAQ) system. Naturally, the presence of a signal did not necessarily mean that a physics event had been recorded for analysis. Signals could be produced from unwanted sources such as cosmic radiation passing through a detector component or it could just be electronic noise. It was the task of the *trigger* to determine which sets of signals pertain to the physics of interest and to turn on and off data recording. Once there was a *trigger*, the DAQ collected the signals and wrote them to a magnetic tape to be analyzed.

In g11 events were selected based on information from the tagger, the start counter and the time-of-flight scintillators. Data events were recorded when both the tagger Master OR (MOR) and the CLAS Level 1 hardware trigger fell within a timing window of 15 ns. The entire tagger focal plane was kept on and recorded data; however, only the first 40 (highest energy) of the total 61 T-counters were enabled in the trigger. To satisfy the Level 1 trigger, a signal was required from any of the 4 start counter paddles and any of the 48 TOF paddles from two seperate sectors of CLAS within a coincidence window of 150 ns [40]. The requirement lead to data collection of events that all had at least two charged particles detected in different sectors. The tagger, the start counter, and the TOF paddles all have multiple detection elements. Hence, the logic required a pre-trigger OR of the discriminated signal in each system to have generated one signal from each control system that could be used in the trigger module coincidence. Before the pre-trigger, signals in each detector system were split to go to the analog-to-digital (ADC) and the time-to-digital-converter (TDC) boards. Following a trigger the ADC and TDC from all detector systems were digitized and then read into the data stream and the data banks were assembled into an event and recorded. The g11 total trigger rate was about 4.1 kHz and the DAQ was capable of running at 5KHz.

CHAPTER 4

DATA ANALYSIS

The data used in this analysis were collected during the g11 run period from May 17 to July 29, 2004, using the CEBAF Large Acceptance Spectrometer (CLAS). The event trigger required at least two charged tracks detected in different sectors of the CLAS detector. A total of 21 TB of data corresponding to 20 billion triggers were written on a tape. This is one of the largest photoproduction datasets recorded in CLAS. Recorded information from all the detector subsystems were then converted from digital format into a format suitable for physics analysis by the use of reconstruction scripts. This step is known as data *cooking*. During the data *cooking* step, the different detector subsystems (photon tagger, start counter, drift chambers, time-of-flight counters, etc) were calibrated. Calibration consisted of aligning the detector subsystems timing with the beam radio frequency (RF). Calibration also improved the tracks of detected particles, energy and timing reconstructions. Several iterations were necessary in calibrating the detectors. The enhancement of one subsystem's calibration helped to enhance the calibration of other components. The cooking and calibration of the g11 data set was executed by the CLAS Collaboration [41].

The principal objective of this analysis is to study the radiative decay of η' meson: $\eta' \to \pi^+\pi^-\gamma$. The η' is initially photoproduced, but because it is unstable, it will quickly decay into the lighter π-mesons and/or γ(s). Since the trigger required at least two charged tracks, this discards situations in which η' decays into entirely neutral particles. The photoproduction reaction of interest in this analysis is:

$$\gamma p \to p\eta' \tag{41}$$

followed by

$$\eta' \to \pi^+\pi^-\gamma \tag{42}$$

This decay channel has a branching fraction of approximately 29% of the total η' decay width. The η' photoproduction events are reconstructed by exclusively detecting all final state particles, including the p, π^+, π^-, and γ. This chapter describes in detail all steps involved to select events for this analysis as well as the cuts and corrections applied to study the photoproduction and radiative decay of the η' meson.

4.1 GOOD RUNS

Data for the g11 run period were collected using the data acquisition (DAQ) system and was grouped into runs, each of which consisted of $\approx$ 10M events. CLAS runs 43490 to 44133 were included in the g11 run period. Runs 43490 to 44107 were taken with an electron beam energy of 4.019 GeV, while for a small amount of runs from 44108 to 44133 the energy was 5.021 GeV. This analysis is based on the 4.019 GeV data. The statistical impact of the exclusion of 5.021 GeV data is negligible. The set of runs from 43490 to 43525 were commissioning runs. These runs were taken for diagnostic reasons and were not meant to be used for physics analysis. Hence, they were also excluded from the analysis.

Several other runs have also been excluded from our analysis. Runs 43675, 43676, 43777, 43778 and 44013 were taken with different trigger configurations than the standard production trigger. There were documented drift chambers problems that occurred during runs 43981 and 43982. Also, a data acquisition problem occurred during runs 43989 to 43991. Some other runs had problems with the DC power supply to the `TOF` counters in sector 2 (44000-44002, 44007, 44008, 44010-44012) and sector 3 (runs 43586-43596). Run 43558 was found to have an unusually low normalized ω yield. Finally, an unknown computer error occurred while skimming run 43871. These twelve runs have all been excluded from this analysis. Table 5 summarizes the cooked runs which were excluded.

Run	Description
43490-43525	Commissioning Runs
43558	Abnormal Normalized ω Yield
43586-43596	TOF Problem in Sector 3
43675-43676, 43777-43778, 44013	Different Trigger Configuration
43871	Data Processing Error
43981-43982	Logbook Lists DC Problems
43989-43991	Logbook Lists DAQ Problems
44000-44002, 44007-44008, 44010-44012	TOF Problem in Sector 2
44108-44133	5.021 GeV Beam Energy

TABLE 5. g11a cooked runs excluded from analysis and justification.

4.2 EVENT SELECTION

The trigger and detector timing information was used to select events. Events were selected with three charged tracks identified as a p, π^+ and π^- and one γ in the final state. These particles were selected according to particle id assigned by the CLAS Simple Event Builder (SEB) package. It uses the start counter (`SC`) to get an interaction vertex time for each charged particle and links it up with photons tagged by electrons in the tagger, where there are up to 10 photons for a given event. The photon with the closest time to a given track is considered to be the photon that caused the event. Specifically, the electron beam bucket (`RF` time) that produced the event is used to obtain the interaction time. A coincidence of the tagger T-counter with the `SC` is used to correlate the photon production time with the interaction time. The photon interaction time (vertex time) for the event is then obtained from the `RF` time for the photon. The velocity β_{meas} for each particle is calculated using the time of flight from the event vertex to the scintillator counter (the `TOF` detector subsystem). Each track in the event needs to have a hit registered in the `SC` for its mass to be calculated. Mass can be calculated from β and a particle's measured momentum as:

$$m_{cal} = \sqrt{\frac{p^2(1-\beta_{meas}^2)}{\beta_{meas}^2 c^2}} \tag{43}$$

where

$$\beta_{meas} = \frac{L}{ct_{meas}} \tag{44}$$

- L is the path length from the target to the scintillator,
- c is the speed of light,
- $t_{meas} = t_{sc} - t_\gamma$ is the time difference between the time at which the particle hits the `TOF` scintillator wall (t_{sc}) and the time at which the photon was at the interaction vertex.

For an assumed mass, the time of flight is calculated as:

$$t_{cal} = \frac{L}{c}\sqrt{1+(\frac{m}{p})^2} \tag{45}$$

where m is the particle's assumed mass.
Such that

$$\beta_{cal} = \frac{L}{ct_{cal}} \tag{46}$$

It then becomes possible to reject events that do not belong to the correct RF beam bucket (i.e. suppress accidental coincidences from different beam bunches) by implementing a ± 2 ns cut on

$$\triangle\, t = t_{meas} - t_{cal} \tag{47}$$

To identify a particle type, the SEB package computes the velocity β_{meas} of the detected particle and compares it with the expected velocity β_{cal} corresponding to the measured momentum and the masses of different possible types of particles. The type of particle is then chosen based on the minimum difference between β_{meas} and β_{cal}.

4.3 ENERGY AND MOMENTUM CORRECTIONS

The quality of data used for this analysis was improved by doing energy and momentum corrections so as to be certain the energies and momenta of tracks were as accurate as possible. There were three corrections implemented which consisted of the tagger energy correction, charged particle energy loss correction [42] and momentum correction [43], in that order. The major concern when the corrections were carrried out was whether the charged particles in the events used were actually p, π^+ and π^-. In the sections that follow, the procedure used for each of these corrections will be discussed.

4.3.1 TAGGER ENERGY CORRECTION

The frames holding the photon tagger's focal plane sagged under the influence of gravity, thereby causing misalignments of some components from their nominal positions. These alignment issues of the tagger's E-counters were first discovered in 2003 ([44],[45],[46]). The sagging leads to inaccuracy in the reconstructed energy of the photon from the raw tagger information. The photon energy correction was implemented by using the channel $\gamma p \rightarrow \pi^+\pi^- X$ [47]. The relative tagger energy correction as a function of E-counter are shown in FIG. 33, where the three curved segments correspond to the sagging of the aluminium frame

holding the tagger focal plane between its support points. The several points inconsistent with the curve correspond to cable swaps.

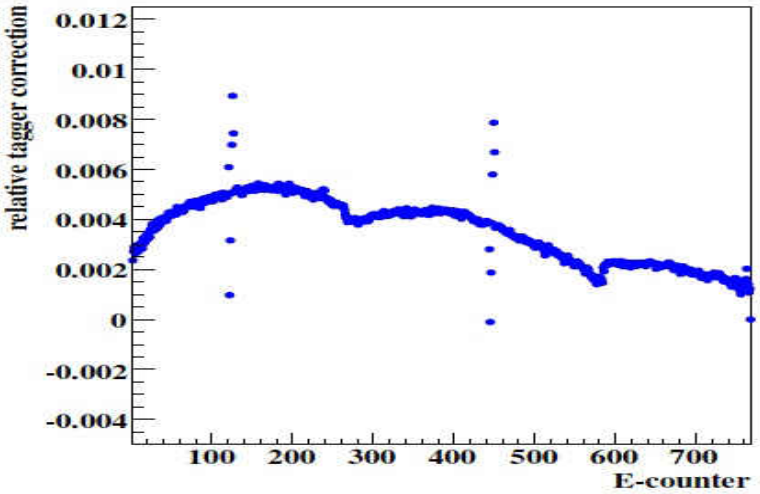

FIG. 33. Relative Tagger energy correction ($\Delta E_\gamma / E_{beam}$) as a function of tagger channel number. Structure corresponds to the physical distortion of the tagger detector plane and shifted points correspond to the cable swaps. Image source [47].

4.3.2 ENERGY LOSS CORRECTION

Tracking generally begins after a particle had already traversed through the target and start counter (ST). Therefore, the measured momentum would be decreased by the "energy-loss" the particle had undergone before entering the Region 1 DC. This "energy-loss" is due to charged particles losing their energy through atomic excitation and ionization while traveling through materials in the CLAS detector. The effect of "energy-loss", in CLAS, is only indicative to all charged particles. The momenta of the p, π^+ and π^- were corrected to

account for energy lost in the target material ($l\mathrm{H}_2$), kapton target walls, the beam pipe, the start counter and the air between the start counter and the Region 1 DC. The corrections were applied by the *eloss* software package written by Eugene Pasyuk for the CLAS detector [42]. The "energy loss" was estimated using momenta and masses of charged particles.

4.3.3 MOMENTUM CORRECTION

Inaccuracies in the magnetic field map of the toroidal magnet as well as differences in the survey information from faulty drift chambers can lead to discrepancies in the reconstructed momenta of charged particles. The g11 momentum corrections obtained by V. Kubarovsky [43] have been implemented in this analysis. The corrections were determined based on the missing mass technique. The corrections as functions of angle were obtained for p, π^+ and π^- after applying energy loss and tagger energy corrections to the data.

The reactions $\gamma p \to \pi^+\pi^- p$ and $\gamma p \to K^+K^- p$ were used to derive the proton momentum corrections, while only the inclusive reaction $\gamma p \to \pi^+\pi^- p$ was used to obtain the momentum corrections for π^+ and π^-. The corrections ($R = P_{corrected}/P_{measured} - 1$) are plotted for the positive and negative particles in FIG. 34 and FIG. 35, respectively. A polynomial fit to the data in these figures were used to calculate the momentum corrections. The maximum momentum correction factors as a function of ϕ angle are on the order of 1%.

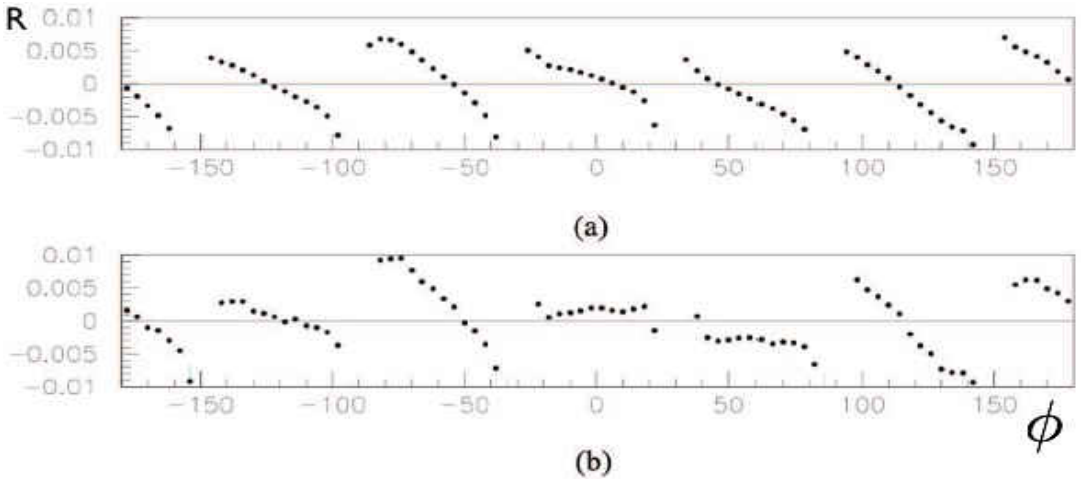

FIG. 34. Momentum correction factor $R = P_{corrected}/P_{measured} - 1$ as a function of ϕ angle for positive particles estimated from the missing mass distributions in $\gamma p \to \pi^+\pi^- p$ reaction for: (a) π^+, (b) protons. Image source: [48].

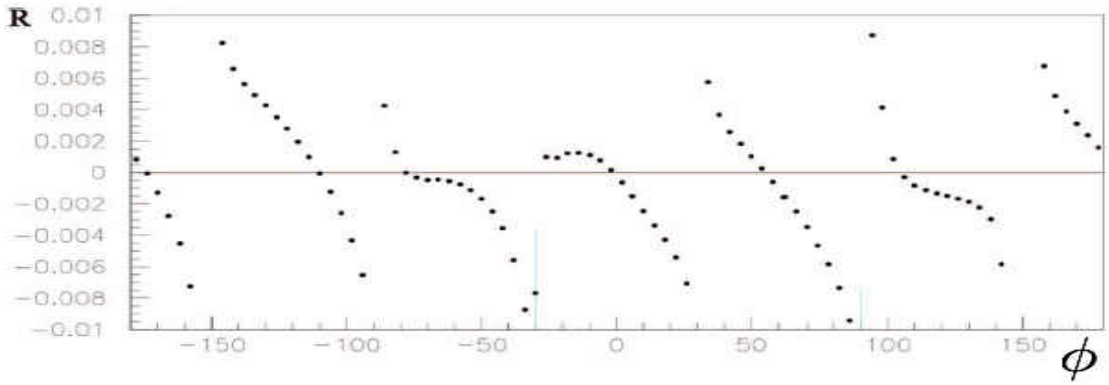

FIG. 35. Momentum correction factor $\mathrm{R} = \mathrm{P}_{\mathrm{corrected}}/\mathrm{P}_{\mathrm{measured}} - 1$ as a function of ϕ angle for π^- estimated from the missing mass distributions in $\gamma\mathrm{p} \to \pi^+\pi^-\mathrm{p}$ reaction. Image source: [48].

4.4 DETECTOR PERFORMANCE CUTS

It is important to implement cuts to data that are related to the CLAS detector performance. When some components or regions of the detector have rapidly changing efficiencies that are not well understood in the Monte Carlo simulation, corresponding events were removed from the analysis. Two of such cuts were performed in this analysis.

4.4.1 FIDUCIAL CUTS

An acceptance study comparing the agreement between data and Monte Carlo (see [47]) was used to remove regions of the detector that weren't well modeled and needed to be removed from the analysis. In particular, the magnetic field changes rapidly near the torus coils thereby making these zones hard to model. Hence, any particle whose path is close to a torus coil is removed from the analysis. This cut is most pronounced in the forward region, where the coils occupy a larger fraction of the solid angle. Regions of the dectector where the efficiency is less than 40% are cut out. FIG. 36 shows the outcome of these cuts.

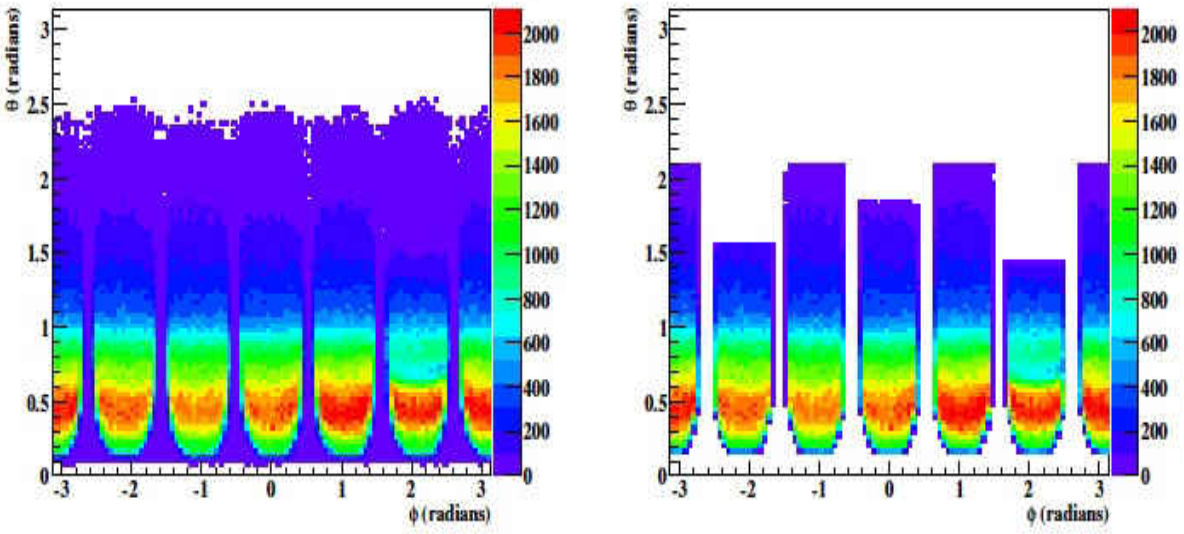

FIG. 36. θ(radians) vs ϕ(radians):(a) All tracks in run 43582. (b) Tracks in 43582 which pass our fiducial volume cuts. The effects of the fiducial cuts are most dramatic at the sector boundaries and in the forward direction where the torus coils occupy a larger fraction of the solid angle. Image source [47].

4.4.2 TOF PADDLE KNOCK OUTS

Another necessary cut required removing dead scintillator paddles. The paddles were identified by comparing occupancy plots of both the data and Monte Carlo. Table 6 lists problematic paddles in each sector that were neglected.

Sector	Paddle number
1	18,26,27,33
2	none
3	11,24,25
4	26
5	20,23
6	25,30,34

TABLE 6. Time-of-flight paddles excluded from our analysis.

4.5 PARTICLE IDENTIFICATION

The decay of η' meson to $\pi^+\pi^-\gamma$ stemming from the photoproduction process $\gamma p \to p\eta' \to p\pi^+\pi^-\gamma$ requires the identification of final state particles p, π^+, π^- and γ. While the charged particles where easily identified, the separation of a single photon from π^0 was necessary. Several cuts were implemented to reduce the background and to remove events outside of our reaction of interest. In general, the strategy is to use kinematic constraints to eliminate backgrounds while ensuring that the signal remains robust. The efficiency of various cuts was tested with Monte Carlo simulations.

The kinematic constraints used so far are listed below:

- FIG. 37 shows the missing mass squared of all detected particles with a cut on missing energy $|ME - E_\gamma| < 0.12$ GeV. Where $ME = E_{beam} - E_{p\pi^+\pi^-}$, is the missing energy of all charged particles and E_γ, is the energy of the detected photon. This plot shows a peak around zero, but it does not yet secure rejection of π^0 in the event.

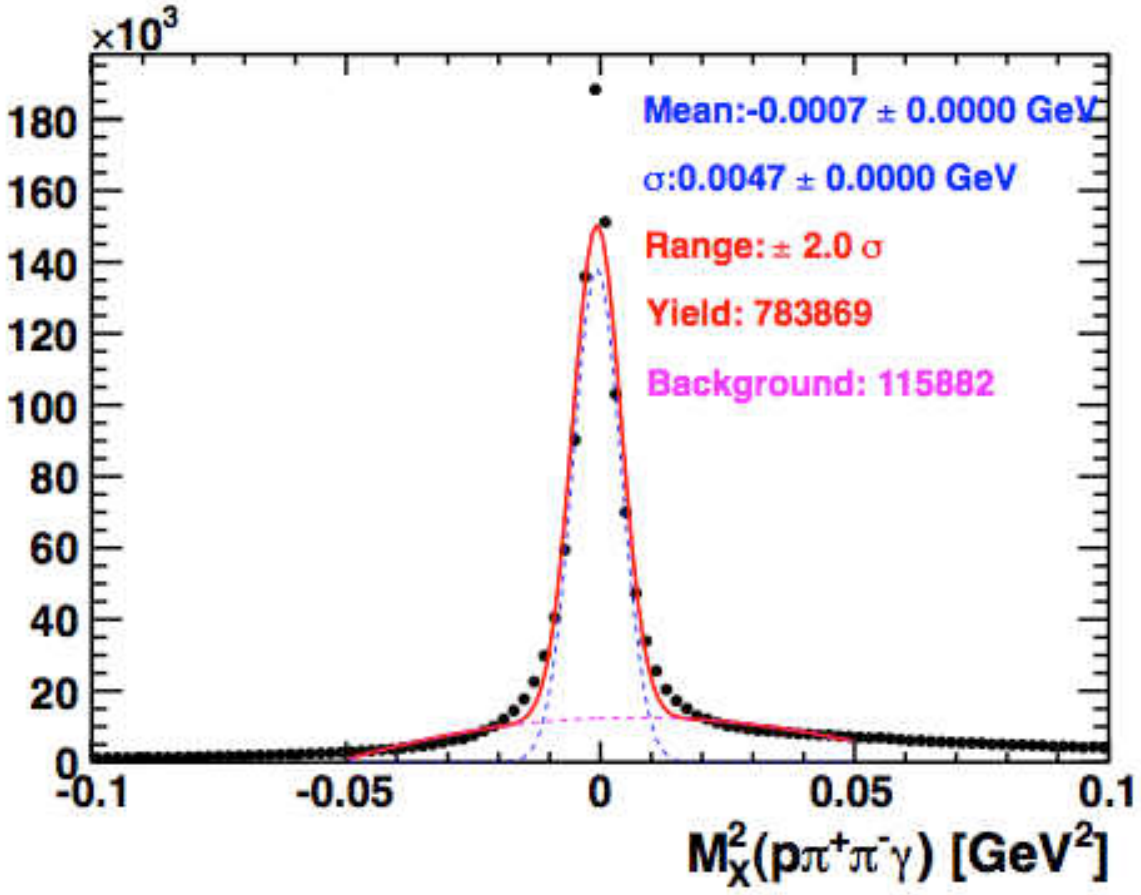

FIG. 37. Missing mass $M_X^2(p\pi^+\pi^-\gamma)$ of all detected final state particles.

- Energy cuts included that for the out-going photon, the combined energy of the three detected charged particles, and the energy difference between these two cuts (FIGs. 38, 39 and 40).

- To ensure there is no π^0 amongst p, π^+ and π^- in the final state, the square of the missing mass $M(p\pi^+\pi^-)^2$ with additional cut $|M(p\pi^+\pi^-\gamma)^2| < 0.01$ GeV^2 for the range of missing mass $M_X(p)$ in the η' region (FIG. 41) were plotted for the peak and two side bands of the distribution of $M_X(p) - M_{\eta'}$ (FIG. 42). One can clearly see how the peaks of γ and π^0 can be seperated by side band substraction (FIG. 43).

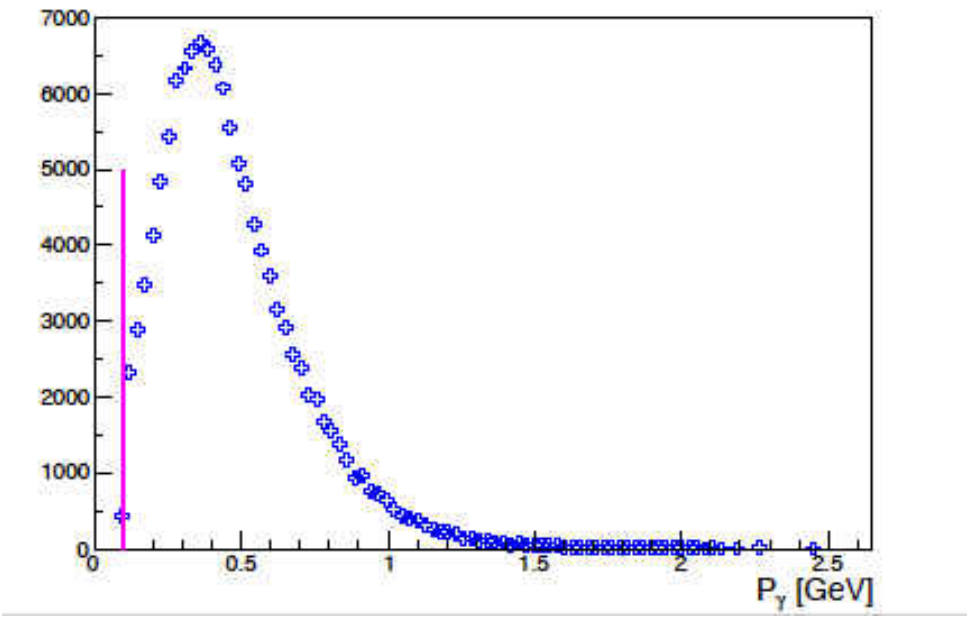

FIG. 38. Photon momentum cut ($P_\gamma > 0.1$ GeV).

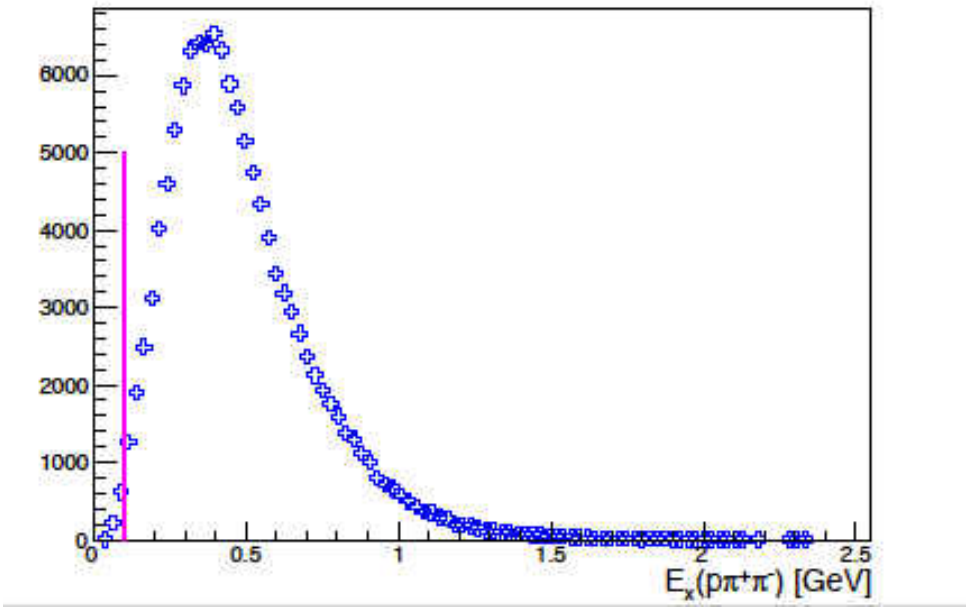

FIG. 39. Missing energy of $p\pi^+\pi^-$, $E_x(p\pi^+\pi^-) > 0.1$ GeV.

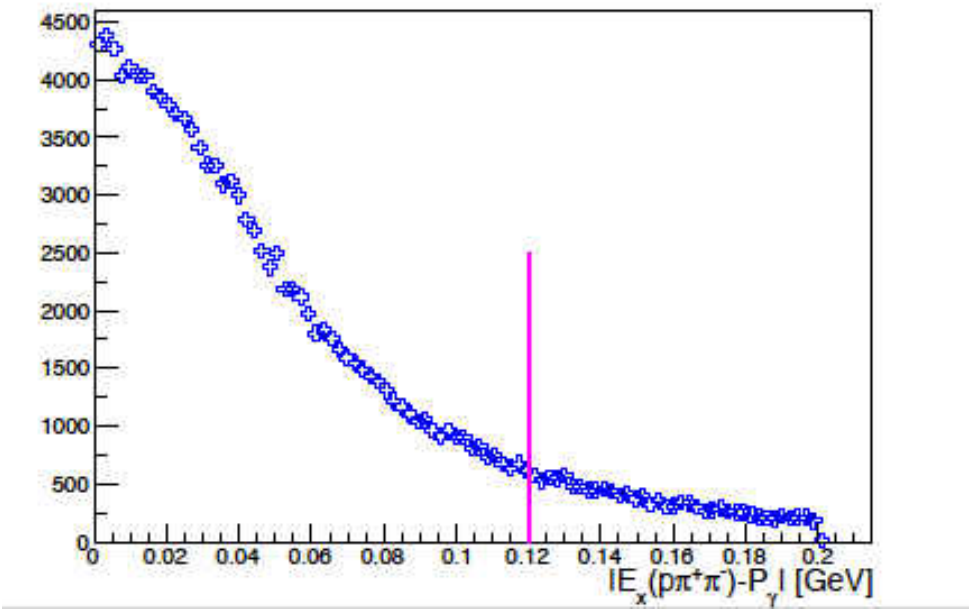

FIG. 40. Difference in the photon momentum and charged particles momentum combined, $\mid E_x(p\pi^+\pi^-) - P_\gamma \mid < 0.12$ GeV.

- Reconstruction of all particles of interest with the best resolution was obtained by plotting the missing mass $M_X(p)$ with the cuts $|M_X^2(p\pi^+\pi^-\gamma)| < 0.01$ GeV^2 and $|M_X^2(p\pi^+\pi^-)| < 0.005$ GeV^2, FIG. 41.

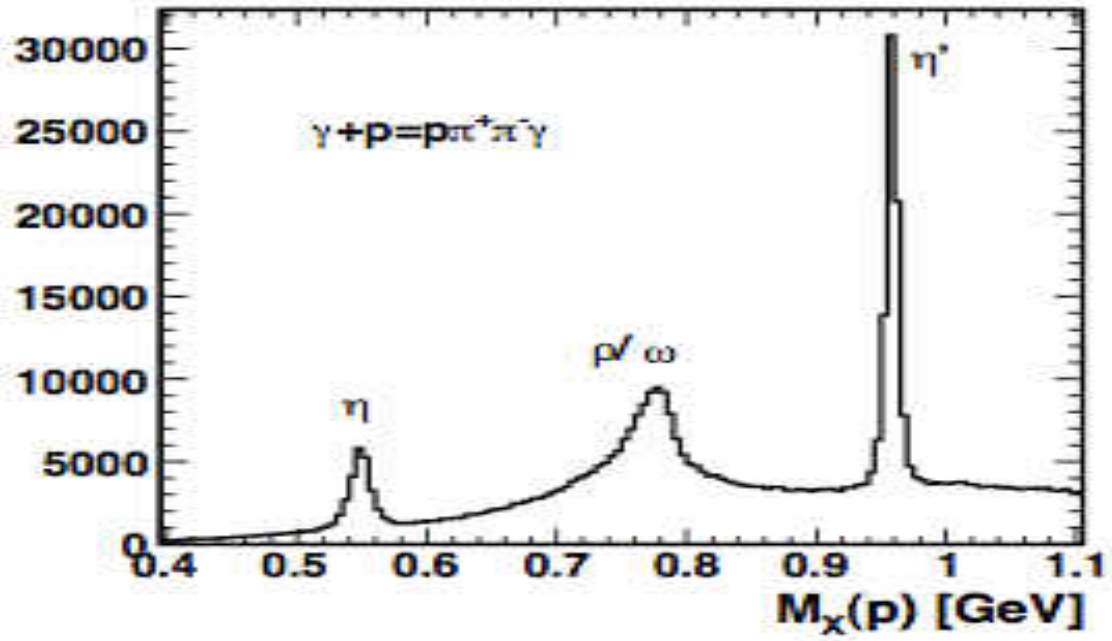

FIG. 41. Distribution of missing mass of the proton in the exclusive reaction $\gamma p \to p\pi^+\pi^-\gamma$.

4.6 EXTRACTING SIGNAL EVENTS

For each 5 MeV-wide $m_{\pi\pi}$ bin, signal and sideband regions were selected for a 3σ range from the $M_X(p) - M_{\eta'}$ spectrum. Giving a total width of each of the regions as 15 MeV, FIG. 42.

The missing mass squared distribution of the three selected charged particles, $M_x^2(p\pi^+\pi^-)$ was then analyzed for each $m_{\pi\pi}$ bin, FIG. 43. The sideband region distribution is substracted from that of signal region leading to a more regular distribution that was fitted with a gaussian or double-gaussian as deemed necessary to get the number of $\pi^+\pi^-\gamma$ signal events, with corresponding statistical errors stemming from the fitting procedure, for each $m_{\pi\pi}$ bin, FIG. 44.

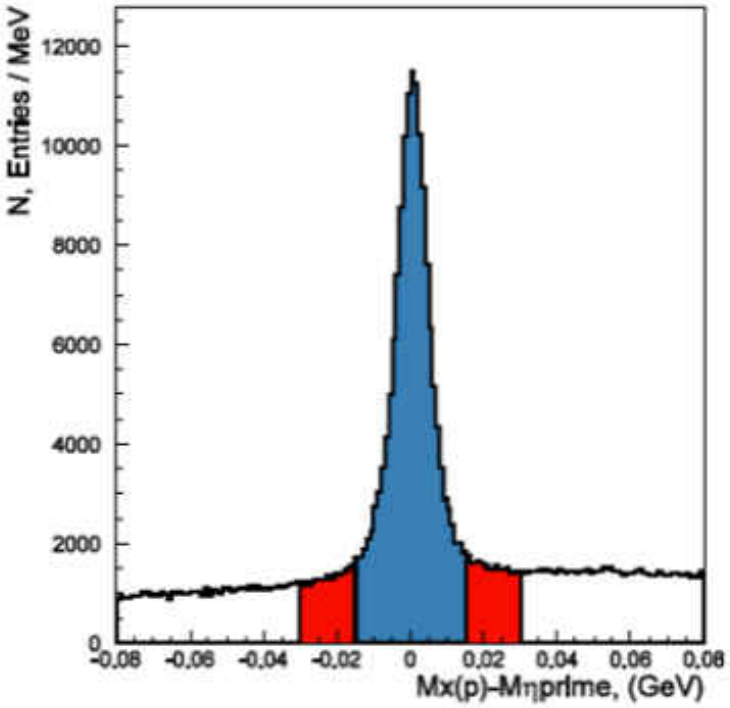

FIG. 42. Distribution of $M_X(p) - M_{\eta'}$ for 0.32 GeV$< m_{\pi\pi} <$ 0.92 GeV in the η' region from FIG. 41

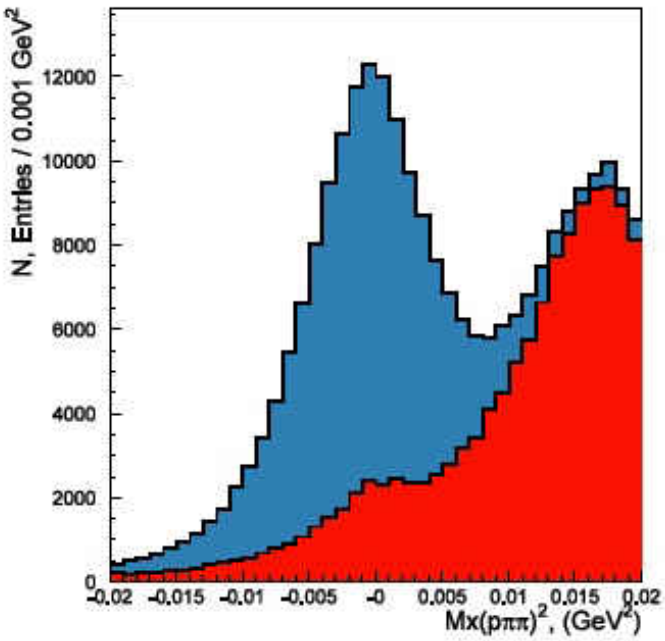

FIG. 43. Histograms of $M_x^2(p\pi^+\pi^-)$ from peak (blue) and side bands (red) of FIG. 42. The difference of this histograms signifigantly separates γ's from π^0's arising from the reaction $\eta' \to \pi^+\pi^-\pi^0$.

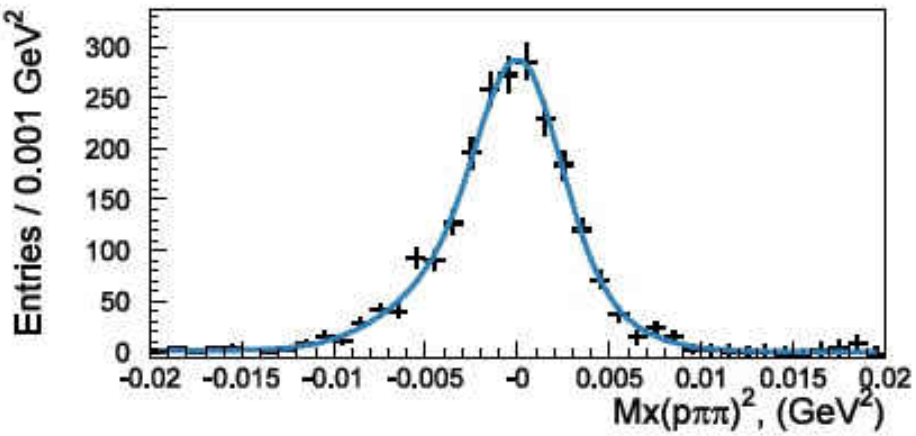

FIG. 44. Sample $M_x^2(p\pi^+\pi^-)$ distribution for $m_{\pi\pi}$ bin 0.765-0.770 GeV after side band substraction.

4.7 ACCEPTANCE CORRECTION AND NORMALIZATION

4.7.1 MONTE CARLO SIMULATION

Some particles in the reaction $\gamma p \to p\eta' \to p\pi^+\pi^-\gamma$ hit "dead" regions not covered by the CLAS detector and cannot be detected. In addition, the CLAS detector deos not have a 100% acceptance. Hence the number of measured events needs to be corrected to take these into account by calculating the acceptance of the CLAS. To obtain the acceptance corrections for the reaction $\gamma p \to p\eta' \to p\pi^+\pi^-\gamma$, an η' Monte Carlo generator was used (SGEN) along with the CLAS GSIM and RECSIS packages.

For this analysis, η' meson was generated using the Monte Carlo generator SGEN. The SGEN uses FOTRAN based programs and it is very commonly used in hadron physics experiments to generate hadronic production and decay of mesons. It gives a user the freedom to include physics models to obtain desired output. The simulated events in the analysis are modelled with a bremsstrahlung photon, the η' differential cross-section, the pion vector form factor $F_V(m^2_{\pi\pi})$ and the decay matrix element of $\eta' \to \pi^+\pi^-\gamma$. The output of SGEN are extracted in standard CLAS "gamp" files which are then processed with the CLAS simulation suite in the following way:

- The gamp files are first converted into the format of PART bank containing the event.
- GSIM: Geant3-based simulation in CLAS simulates processes affecting particles in the detector, including the energy losses of particles in the detector, particle decays and multiple scattering and finally the digitized informations is sorted in the simulated "raw" banks.
- GPP: GSIM post-processor smears detector signal more accurately to reflect the actual resolution and to simulate the experimental conditions.
- RECSIS : It is used for reconstruction of simulated data and in the same manner that the raw experimental data are analyzed. The cuts applied to the experimental data are also applied to the Monte Carlo (MC) data to select events. Corrections from the CLAS *eloss* package are applied to the reconstructed momenta of the p, π^+ and π^-. However, the momentum corrections and beam energy corrections are not applied to the MC data.

4.7.2 ACCEPTANCE AND RESOLUTION

Acceptance is the probability that an event of a given kinematics will be kept by the analysis. Once the detector acceptance is accounted for, the data must then be normalized to convert the number of events detected into the probability with which events were produced.

The acceptance is calculated as

$$\text{Acceptance} = \frac{\text{Reconstructed events (with corrections and cuts)}}{\text{Generated events}} \tag{48}$$

for each bin in $m_{\pi\pi}$.

The CLAS detector acceptance for $\eta' \to \pi^+\pi^-\gamma$ decay and resolution for two pion invariant mass have been obtained from large statistics Monte-Carlo simulation (GSIM). For this analysis we have chosen a two pion invariant mass range from 0.32 to 0.92 GeV, splitted into 60 (10 MeV wide) bins. In Monte-Carlo we simulated 20 million events for each of such a bin and additionally for one bin below and one bin above this range. Results for acceptance and mass resolution are shown on FIGs. 45, and 46.

Small efficiency enhancement at low mass end is statistically significant and needs to be understood. Decrease of mass resolution σ at high mass end can be caused by limited range for fluctuations at the edge of phase space. We can also note here that Monte-Carlo simulations show minor sytematic shift of two pion invariant mass ($\sim$1...2 MeV).

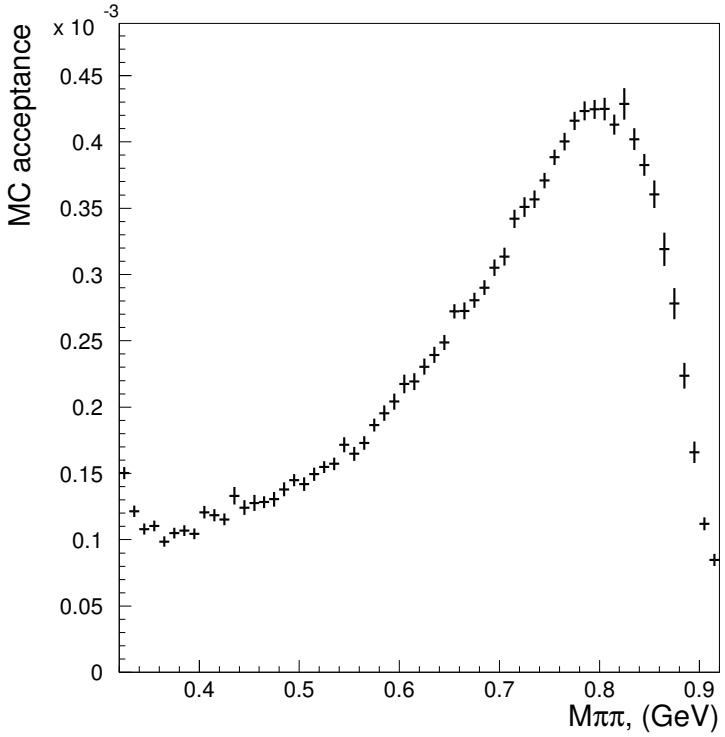

FIG. 45. CLAS detector acceptance for $\eta' \to \pi^+\pi^-\gamma$ decay as a function of two pion inv. mass

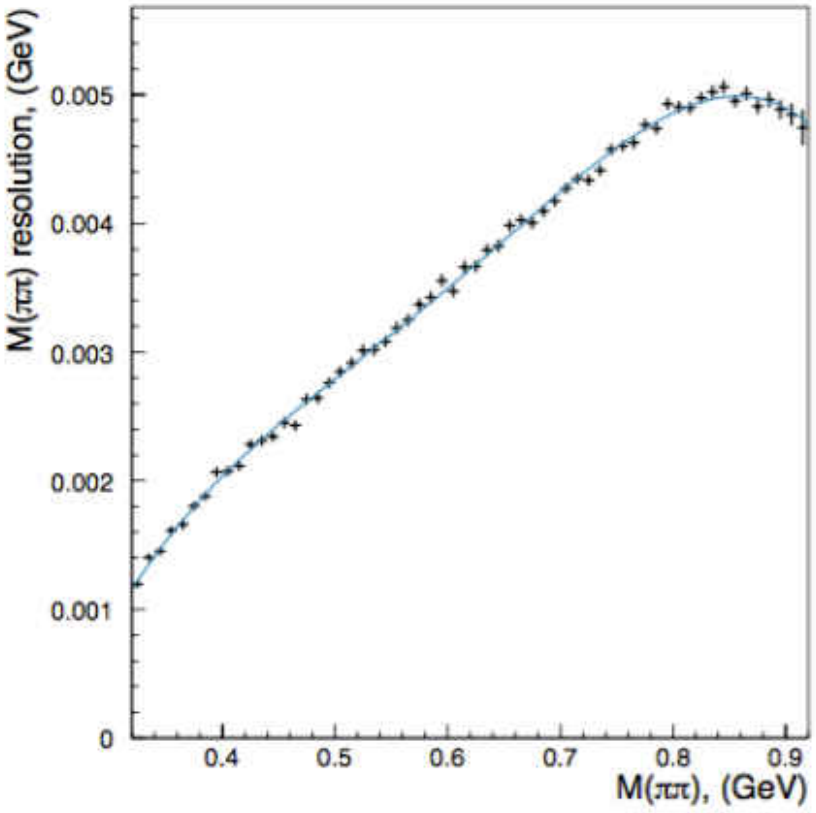

FIG. 46. CLAS detector resolution for two pion inv. mass from $\eta' \to \pi^+\pi^-\gamma$ decay. Blue curve - fit with fifth order polynomial.

4.7.3 THE MONTE CARLO AND DATA COMPARED

To check how well the η' meson event generator, used for this analysis, describes the experimental data, we compare some kinematic variables for simulation and data. The momentum, and angular distribution of the outgoing photon and the detected charged particles of both the data and simulation were compared to verify how well the simulation explains the g11 data, as shown in FIGs. 47 through 58. From all these plots we observe that the overall agreement between the data and Monte Carlo is good.

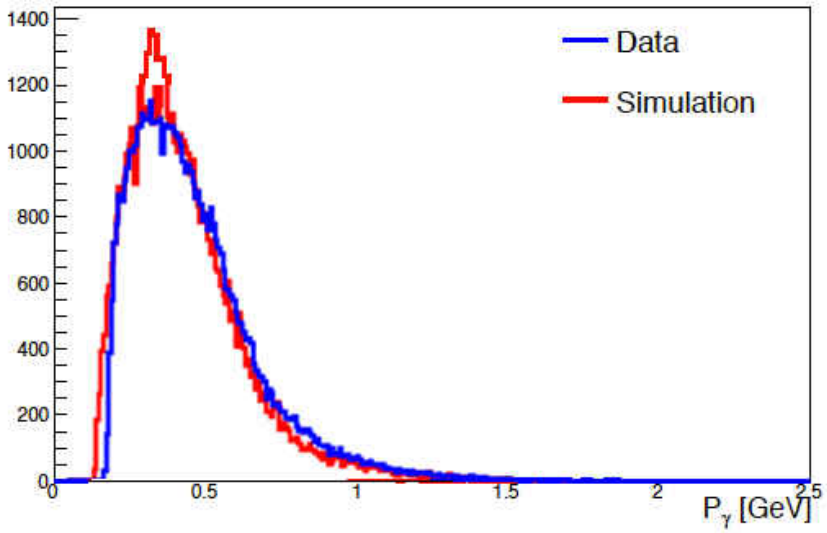

FIG. 47. Comparison of γ momentum with g11 data (blue) and simulated events (red).

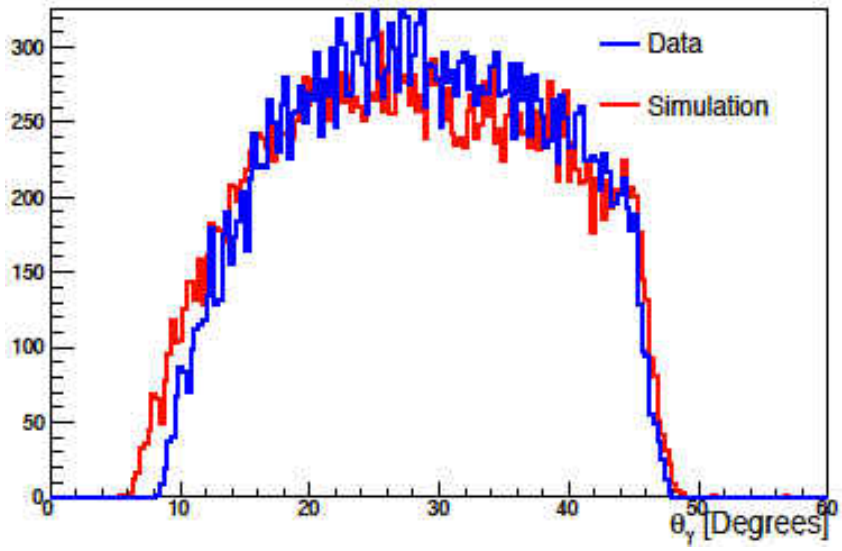

FIG. 48. Comparison of γ θ with g11 data (blue) and simulated events (red).

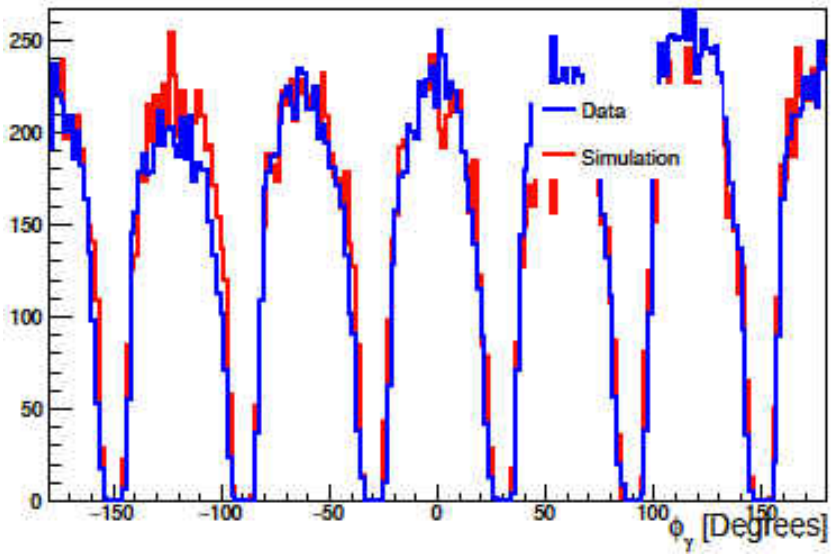

FIG. 49. Comparison of γ ϕ with g11 data (blue) and simulated events (red).

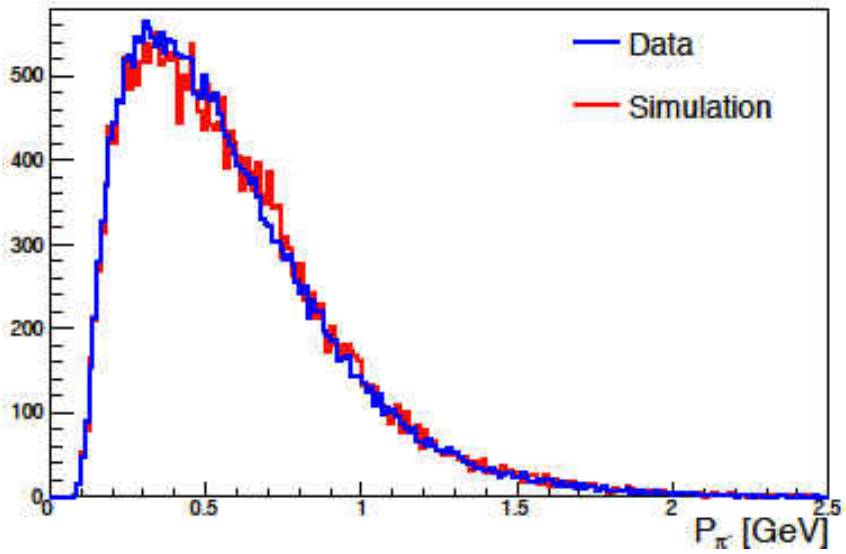

FIG. 50. Comparison of π^- momentum with g11 data (blue) and simulated events (red).

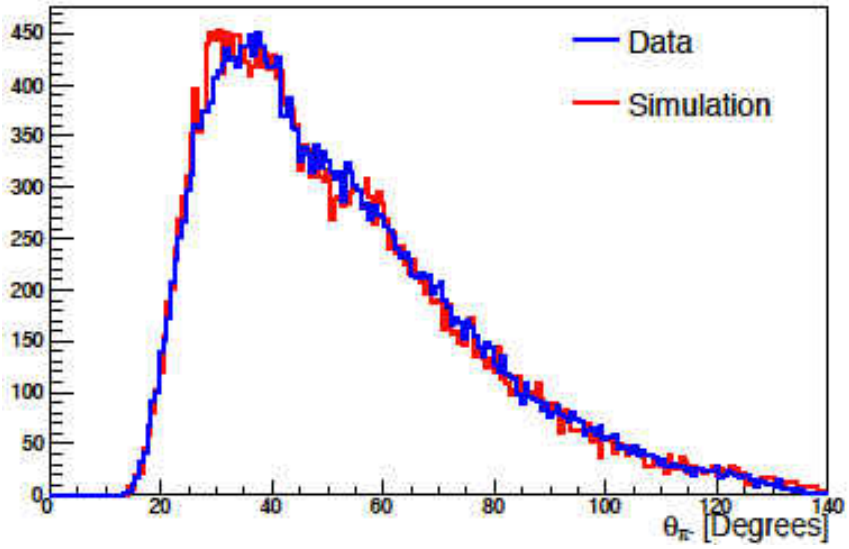

FIG. 51. Comparison of π^- polar angle θ with g11 data (blue) and simulated events (red).

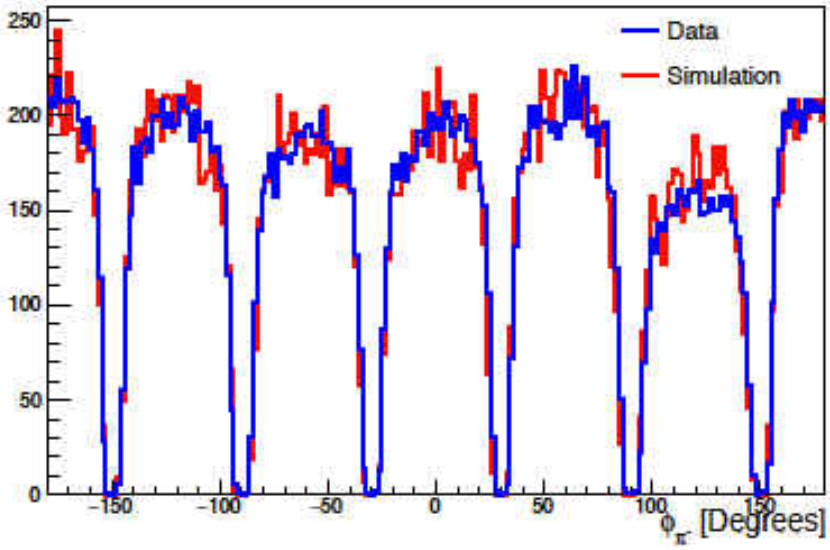

FIG. 52. Comparison of π^- azimuthal angle ϕ with g11 data (blue) and simulated events (red).

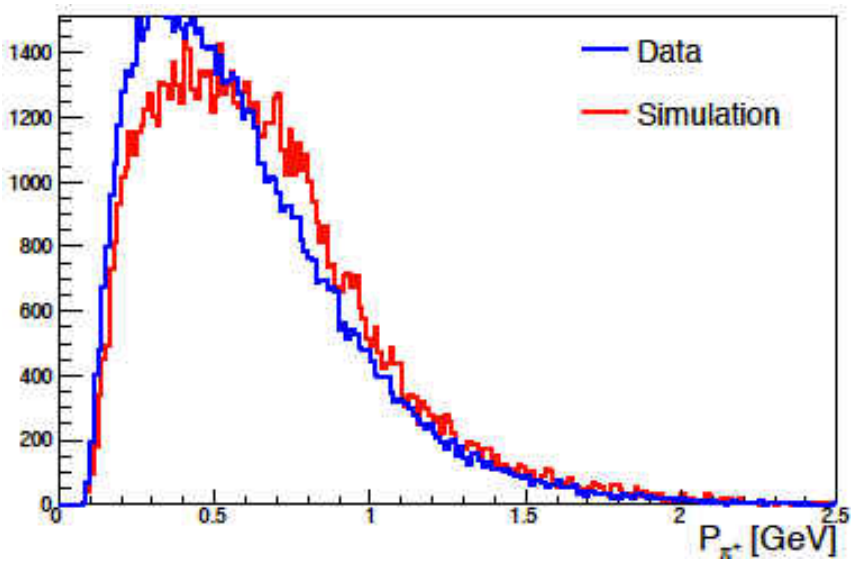

FIG. 53. Comparison of π^+ momentum with g11 data (blue) and simulated events (red).

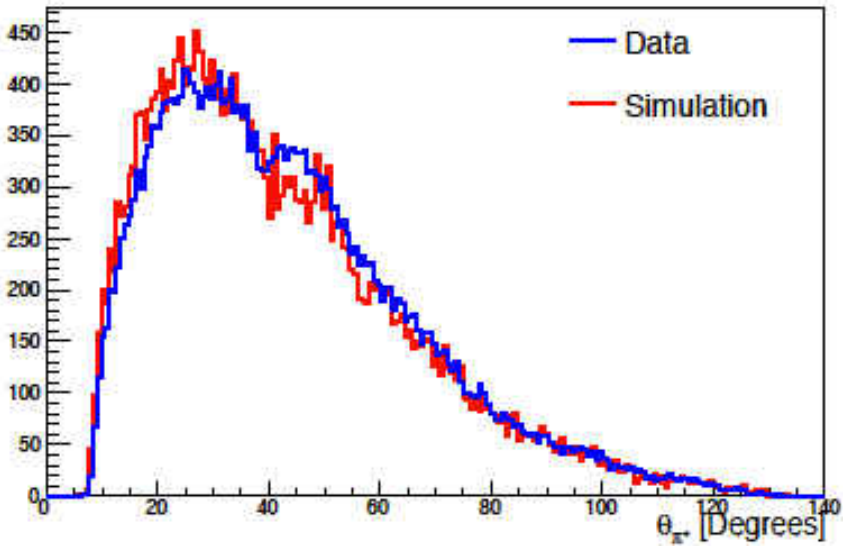

FIG. 54. Comparison of π^+ polar angle θ with g11 data (blue) and simulated events (red).

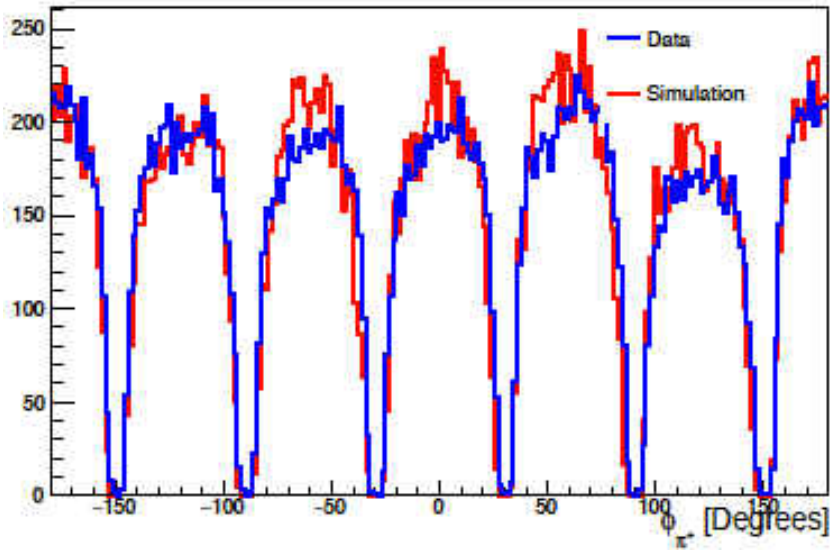

FIG. 55. Comparison of π^+ azimuthal angle ϕ with g11 data (blue) and simulated events (red).

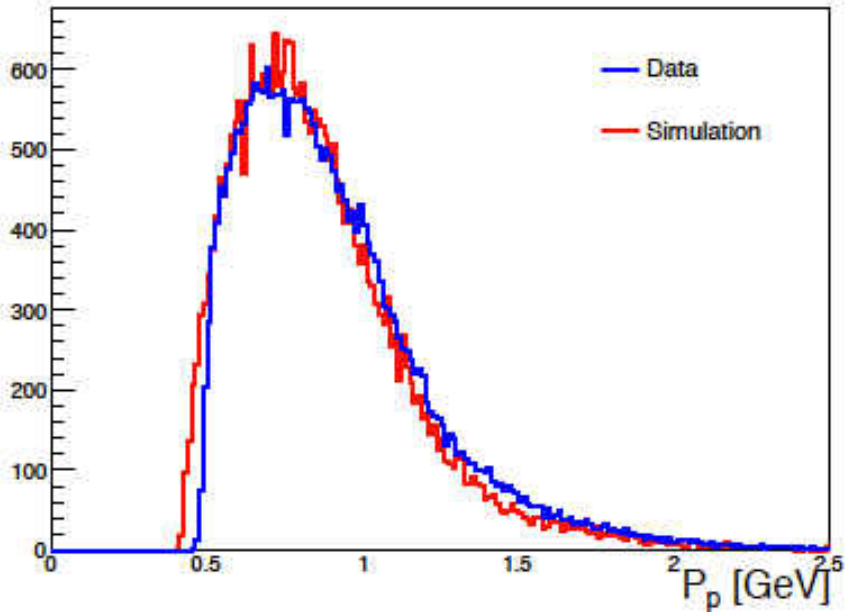

FIG. 56. Comparison of proton momentum with g11 data (blue) and simulated events (red).

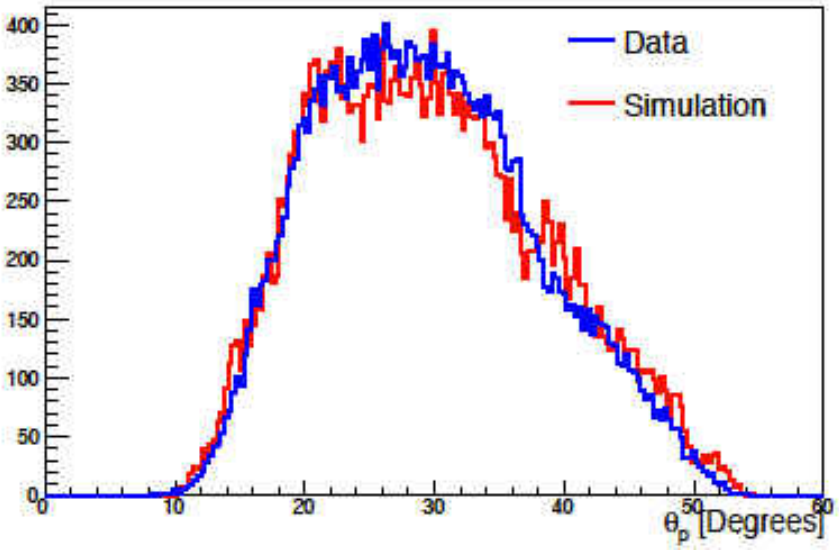

FIG. 57. Comparison of proton polar angle θ with g11 data (blue) and simulated events (red).

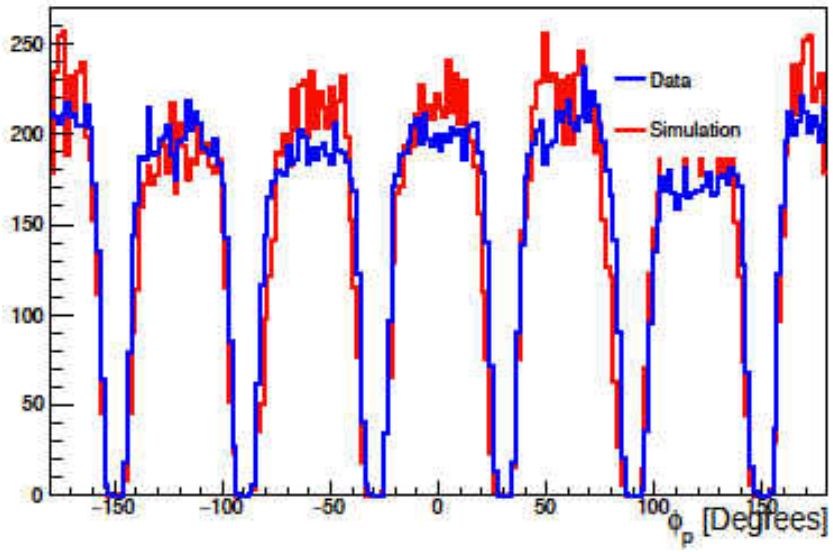

FIG. 58. Comparison of proton azimuthal angle ϕ with g11 data (blue) and simulated events (red).

4.7.4 THE TARGET DENSITY

In order to calculate the η' meson photoproduction cross section we need to know the density of the LH_2 target used in the $g11$ experiment. The density is

$$\rho = a_1 T^2 + a_2 P + a_3 \tag{49}$$

where T is the temperature, P is the pressure and the values of a_1, a_2 and a_3 are given in Table 7.

Parameter	Value
a_1	-2.89 $\times$ 10^{-5} g/cm^{3}K^2
a_2	1.0 $\times$ 10^{-7} g/cm^{3}mbar
a_3	8.249 $\times$ 10^{-2} g/cm^3

TABLE 7. The values of the parameters used to calculate the LH_2 density [48].

At the begining of each `CLAS` run, the target's temperature and pressure were measured. The mean density of the LH_2 used in $g11$ was

$$\bar{\rho} = \frac{1}{N_{run}} \sum_r \rho_r = 0.07177 g/cm^{-3}, \tag{50}$$

and the variance is calculated to be

$$\sigma^2 = \frac{1}{N_{run} - 1} \sum_r (\rho_r - \bar{\rho})^2 = 6.776 \times 10^{-9} g^2/cm^{-6}, \tag{51}$$

leading to relative fluctuations of the density of about 0.1%.

4.7.5 PHOTON FLUX NORMALIZATION

The estimation of the luminosity includes calculation of the number of target particles and the total number of photons incident on the target. Obtaining the total number of photons, or photon flux, incident on the target is an important piece of information required to calculate the η' meson photoproduction cross section. A package, the $gflux$, a standard `CLAS` normalization technique was used to determine the photon flux of the $g11$ experiment

[49]. The $gflux$ program obtains the photon fluxes for each tagger T-counter and for each g11a run by using the rates at which the electrons hit the given T-counter in a fixed time window. The number of electrons that hit the T-counter is adjusted to account for the detector live time. Then the T-counter flux is used to calculate the flux for different photon energy bins [50].

A beam current dependent normalization problem was first observed by the `CLAS` Collaboration Genova group [40] which derived a correction factor by doing a linear fit to the dependence. At a current of 65 nA, the correction factor was 1.187. The Carnegie Mellon University (`CMU`) group suggested the issue might arise from the inaccurate estimate of the `DAQ` dead time. Events associated with a beam trip are excluded from the analysis [51]. In FIG. 59 the photon flux is plotted as a function of incident photon beam energy for 0.05 GeV energy bins.

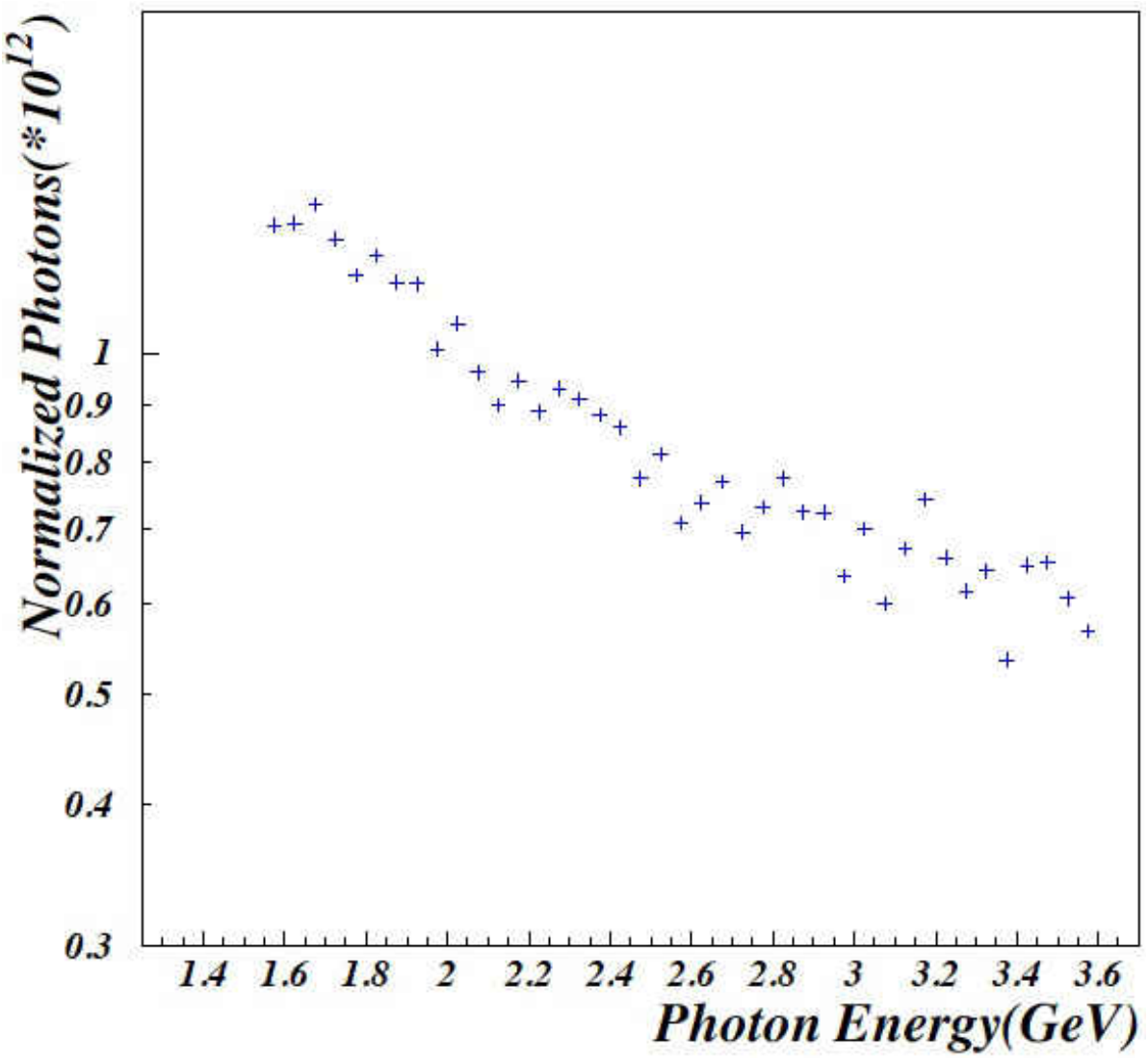

FIG. 59. Photon flux as a function of incident photon beam energy for all good runs. Image source: [48].

CHAPTER 5

RESULTS

The main purpose of this analysis is to study radiative decay of $\eta' \to \pi^+\pi^-\gamma$. In particular, as it was shown in [21], the invariant mass of $\pi^+\pi^-$ ($m_{\pi\pi}$) is sensitive to the underlying dynamics of this decay. However in order to study the decay itself one needs to account for the photoproduction cross section and only after that compare $m_{\pi\pi}$ distribution with theoretical predictions. In this chapter we present our measurement of the photoproduction cross section in this decay mode and comparison with a previous mesurement of the same data set by the CLAS collaboration in $\eta' \to \pi^+\pi^-(\eta)$ decay mode, where the η meson was reconstruced via missing mass technique. After equalizing for a photoproduction cross section, the experimental distribution of invariant mass of pion pairs was fitted using Monte Carlo simulation with all components of the decay matrix elements taken into account.

5.1 DIFFERENTIAL CROSS SECTIONS

In this section, we shall compare the differential cross section measured for the reaction $\gamma p \to p\eta'(\eta' \to \pi^+\pi^-\gamma)$ to that of the published diffrential cross section for the reaction $\gamma p \to p\eta'(\eta' \to \pi^+\pi^-\eta)$ [52]. This is an additional check of the level of correctness of our analysis.

5.1.1 CALCULATION

In a similar manner as in [52], each differential cross section point is extracted using the equation

$$\frac{d\sigma}{d\cos\theta^{\eta'}_{CM}} = \left(\frac{A}{F(W)\rho l N_A}\right)\frac{Y(W,\cos\theta^{\eta'}_{CM})}{\Delta\cos\theta^{\eta'}_{CM} Acc(W,\cos\theta^{\eta'}_{CM})}\frac{1}{BR(\eta' \to \pi^+\pi^-\gamma)} \tag{52}$$

where ρ, l and A are the target density, length and atomic weight respectively, N_A is Avogadro's number, $F(W)$ is the (corrected) number of photons in each W bin incident on the target, $\Delta\cos\theta^{\eta'}_{CM}$ is the width of each $\cos\theta^{\eta'}_{CM}$ bin (for our analysis, this quantity is always 0.075) and $BR \approx 0.291$ is the $\eta' \to \pi^+\pi^-\gamma$ branching ratio. The values used for the target factors are listed in Table 8. Y and Acc are the detected data yield and the acceptance in each (W,$\cos\theta^{\eta'}_{CM}$) bin, respectively.

Factor	Value	Description
ρ	0.7177 g/cm^3	Target density
l_{target}	40 cm	Target length
N_A	6.022×10^{23}	Avogadro's number
A_{target}	1.00794 $g/mole$	Target atomic weight

TABLE 8. Target factors used for all $d\sigma/d\cos\theta^{\eta'}_{CM}$ measurements.

As a supplementary way to check the analysis of this work, we compared the cross sections for the photoproduction of η' in the radiative decay mode $\eta' \to \pi^+\pi^-\gamma$ to those of published cross sections in the decay mode $\eta' \to \pi^+\pi^-\eta$ [52]. The comparison was done for 20 bins within the range $-0.65 < cos\theta^{\eta'}_{cm} \leq 0.85$, as the yield drops near the beam pipe, and 36 bins in the invariant mass range of 1.97 GeV $<$ W $<$ 2.83 GeV. FIGs. 60 to 63 show comparison of our calculated cross section (tabulated in Appendix A) to that of [52]. There is a very good agreement.

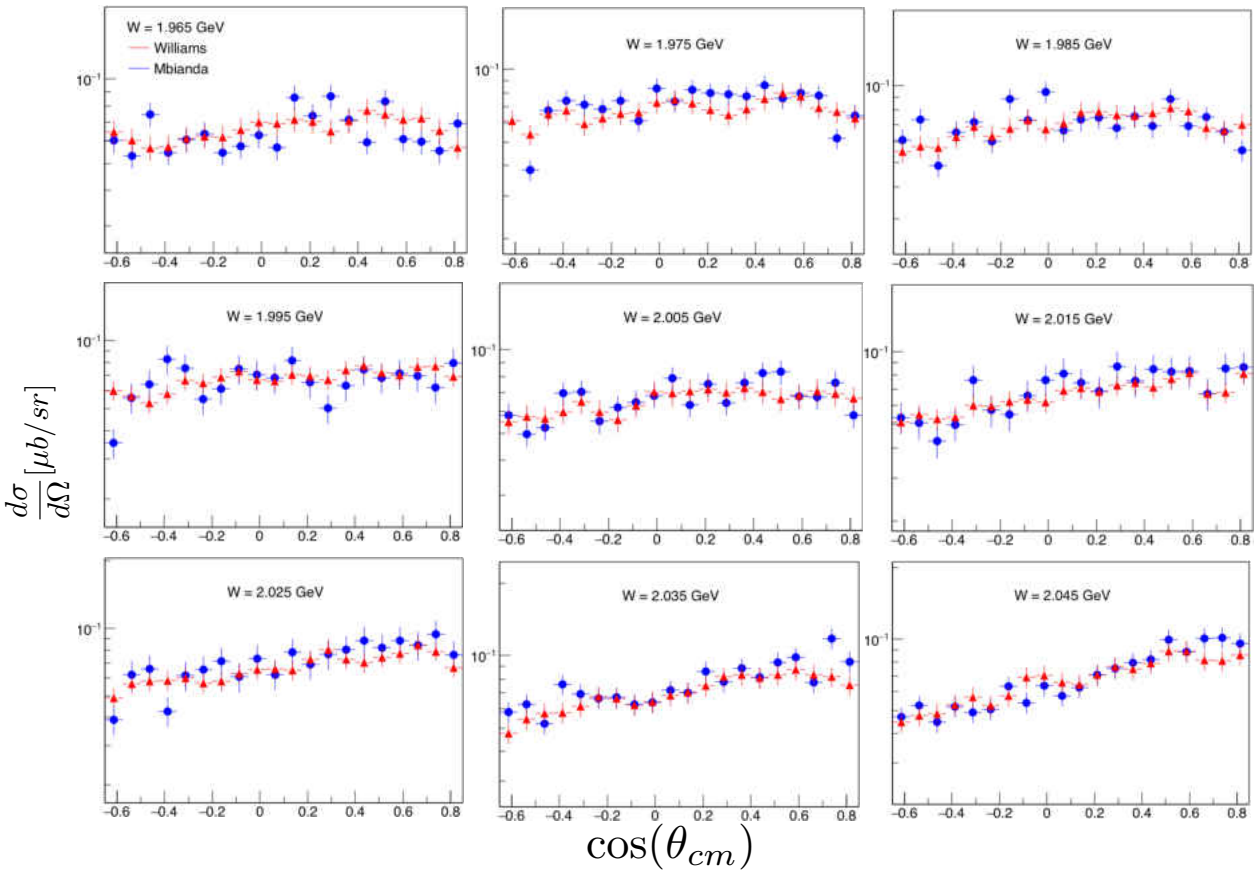

FIG. 60. $d\sigma/d\Omega$ (μ b/sr) vs. $\cos\theta^{\eta'}_{CM}$ for $\gamma p \to p\eta'$ reaction for $W = 1.96 - 2.05$ GeV. The red points are published results, [52] while the blue points are verifications from our analysis

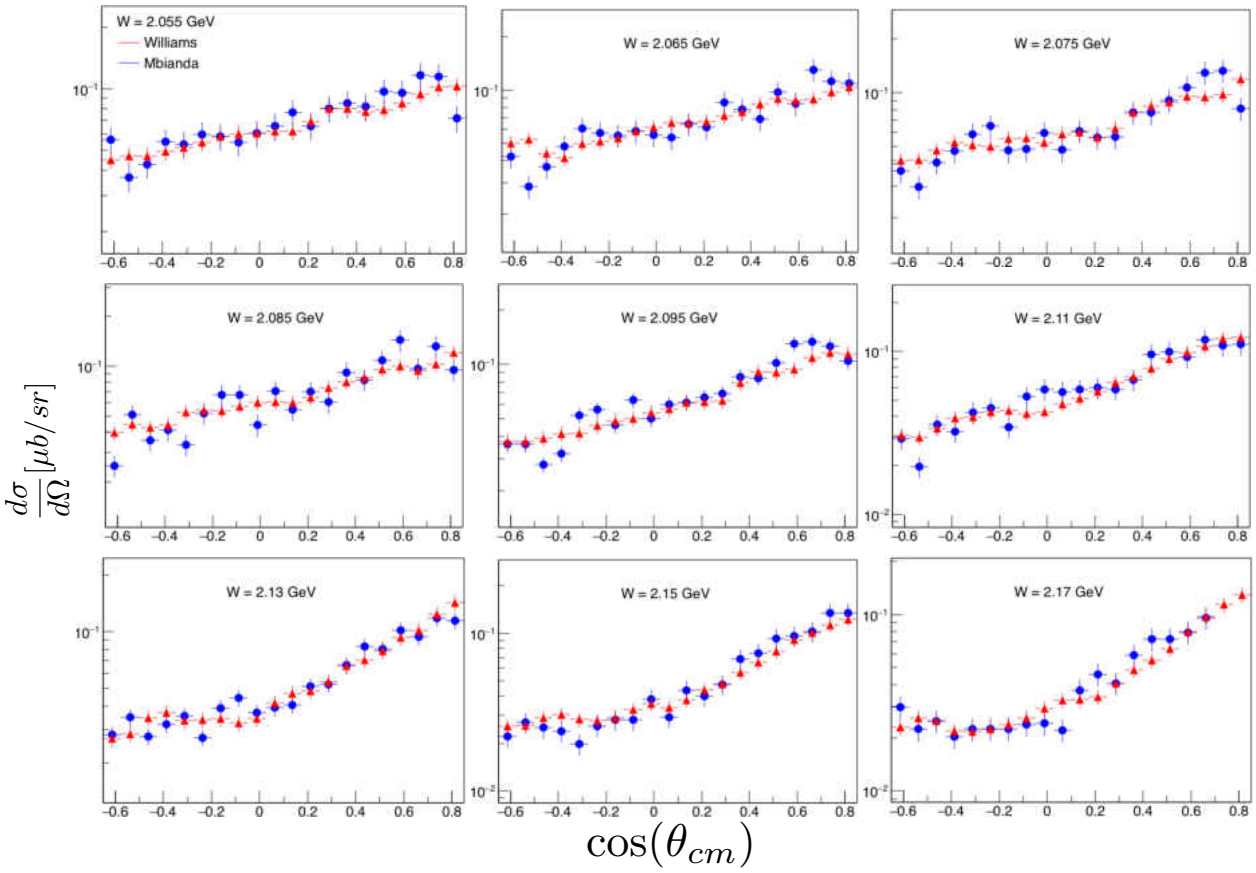

FIG. 61. $d\sigma/d\Omega$ (μ b/sr) vs. $\cos\theta^{\eta'}_{CM}$ for $\gamma p \to p\eta'$ reaction for $W = 2.05 - 2.18$ GeV. The red points are published results, [52] while the blue points are verifications from our analysis

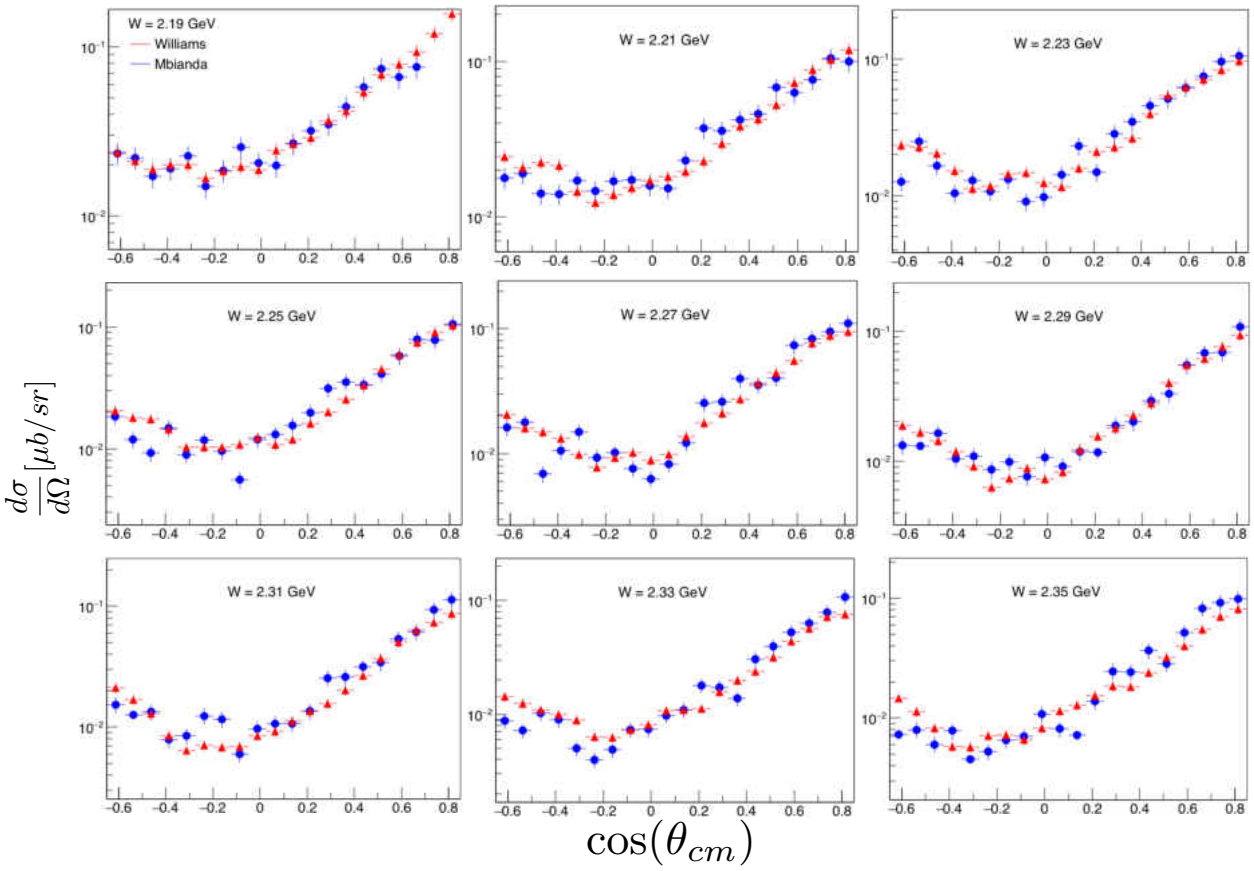

FIG. 62. $d\sigma/d\Omega$ (μ b/sr) vs. $\cos\theta^{\eta'}_{CM}$ for $\gamma p \to p\eta'$ reaction for $W = 2.18 - 2.36$ GeV. The red points are published results, [52] while the blue points are verifications from our analysis

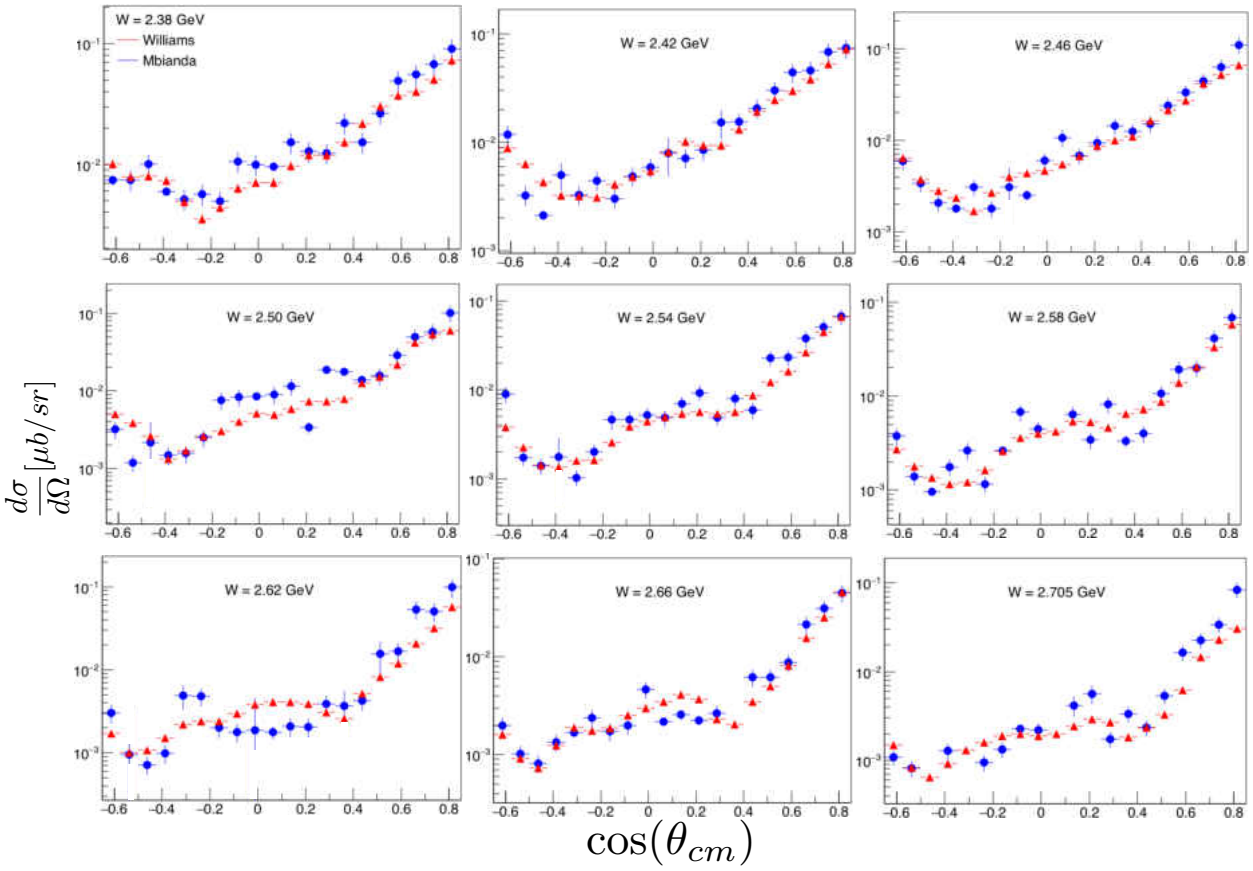

FIG. 63. $d\sigma/d\Omega$ (μ b/sr) vs. $\cos\theta^{\eta'}_{CM}$ for $\gamma p \to p\eta'$ reaction for $W = 2.36 - 2.73$ GeV. The red points are published results, [52] while the blue points are verifications from our analysis

Ratio of Cross Sections

FIG. 64 shows a constant fit to the fitted ratios of our measured cross sections to those of [52] for all 36 W bins, With fit result $R = 0.945 \pm 0.006$. This fit can be used to get an independent measurement of η' branching ratio (BR). In [52] $\mathrm{BR}(\eta' \to \pi^+\pi^-\eta) = 0.429$ was used. In this analysis we have used $\mathrm{BR}(\eta' \to \pi^+\pi^-\gamma) = 0.291$. In order to be consistent with previous measurement, that is, to have the ratio to be equal to 1, one needs to have $\mathrm{BR} = 0.291 \times 0.945 = 0.275$ with statistical error $(0.275 \times 0.006)/0.945 = 0.002$. Hence we obtain $\mathrm{BR}(\eta' \to \pi^+\pi^-\gamma) = 0.275 \pm 0.002$. The best measurement in PDG by `CLEO` Collaboration has a value $0.287 \pm 0.007 \pm 0.004$ [53]. Within error our analysis is consistent with `CLEO` and further studies need to be done to estimate systematic errors. However, statistically we have the best measurement of the BR.

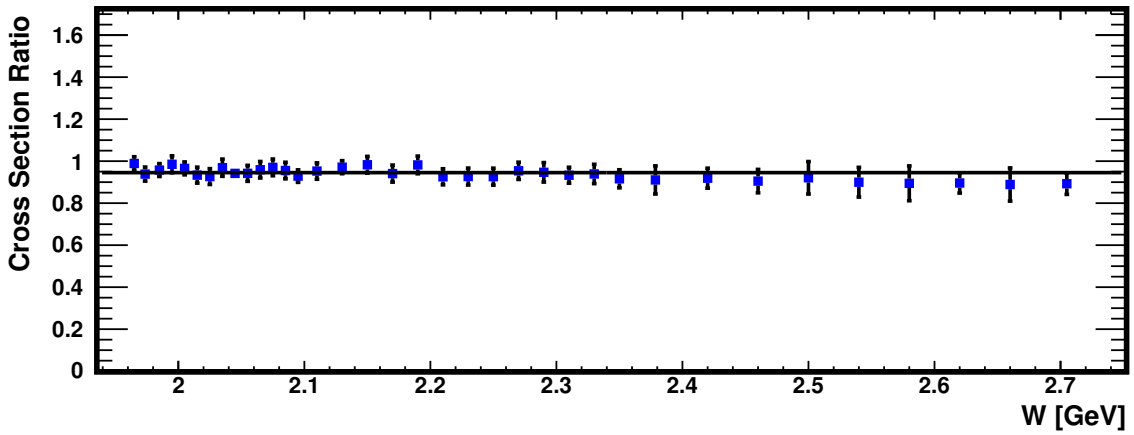

FIG. 64. Zero order polynomial fit to fitted ratio of cross sections at each W bin giving fit R=0.945 ± 0.006.

5.2 METHOD TO EXTRACT $\eta' \to \pi^+\pi^-\gamma$ DECAY PARAMETERS α AND β

5.2.1 DEFINITIONS AND FORMALISM

The distribution of the invariant mass of the two pions, m, in the radiative decay $\eta' \to \pi^+\pi^-\gamma$ (2.4.3) could be written in the following terms of the differential decay rate:

$$\frac{\partial\,\Gamma}{\partial\,m} = C_{\alpha\beta}\, f(m)\,(1 + \alpha m^2 + \beta m^4 + O(m^2))^2, \tag{53}$$

such that

$$\int_{m_{min}}^{m_{max}} \frac{\partial\,\Gamma}{\partial\,m}\, dm = 1. \tag{54}$$

where the normalization constant term $C_{\alpha\beta}$ depends only on the parameters α and β, but the function $f(m)$ does not depend on α and β. The parameter α is introduced to account for a box anomaly, while β is due to a contribution from a_2 tensor meson ([17], [21]). For simplicity the higher order term $O(m^2)$ would be skipped, but it could be easily added in the calculations. The $\eta' \to \pi^+\pi^-\gamma$ decay matrix element can be written (according to [54]) as:

$$|\mathcal{M}|^2 \sim |F_V(S_{\pi\pi})|^2\,(1 + \alpha m^2 + \beta m^4 + O(m^2))^2\, E_\gamma^2\, q^2\, sin^2(\theta) \tag{55}$$

where E_γ is the photon energy, q is the pion momentum, and θ is the angle between the pion plane and the photon (everything in the rest frame of the $\pi^+\pi^-$ pair).

The function $f(m)$ in Eqn. 53 includes product of the decay phase space distribution and squared matrix element function (Eqn. 55) with $\alpha = \beta = 0$. The pion vector form factor $|F_V(S_{\pi\pi})|^2$ is given in [22] (Table 2) as a function of squared mass of two pions $S_{\pi\pi} \equiv m^2$.

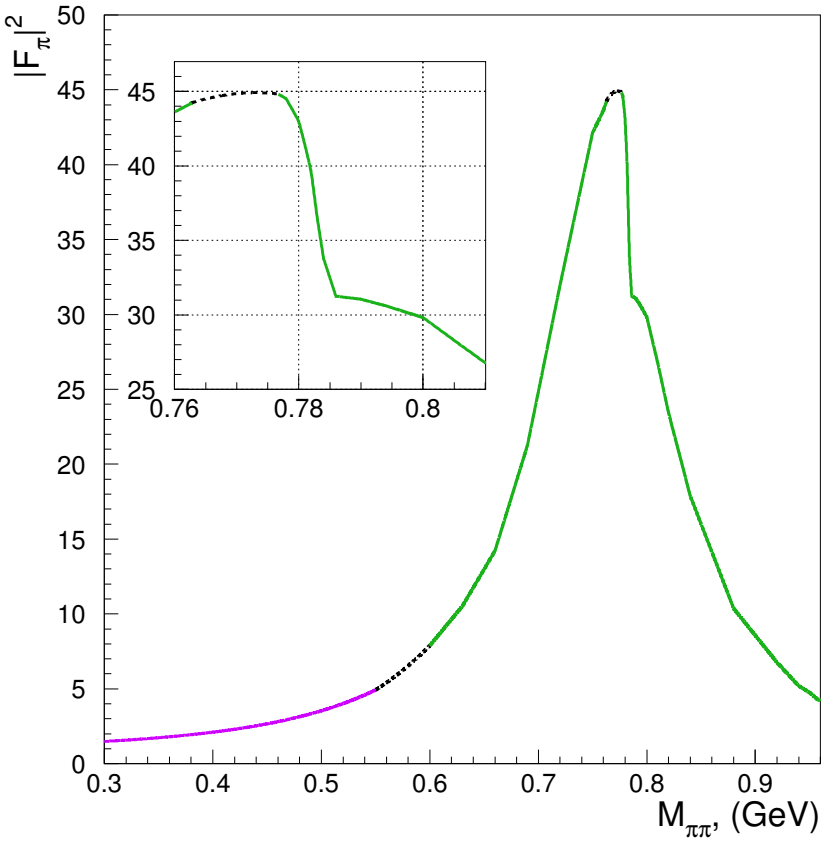

FIG. 65. Squared pion form factor as a function of dipion mass. Left part (purple) - parameterization from [55]. Central solid curve (green) - data points from [56]. Black dashed segments: left one - parabolic approximation for missed region between above data; right one - our fit of the data points presented in [56].

The shape of two pion mass spectrum for simple phase space and with matrix element $|\mathcal{M}|^2$ applied (without the α and β terms) are shown on FIG. 66.

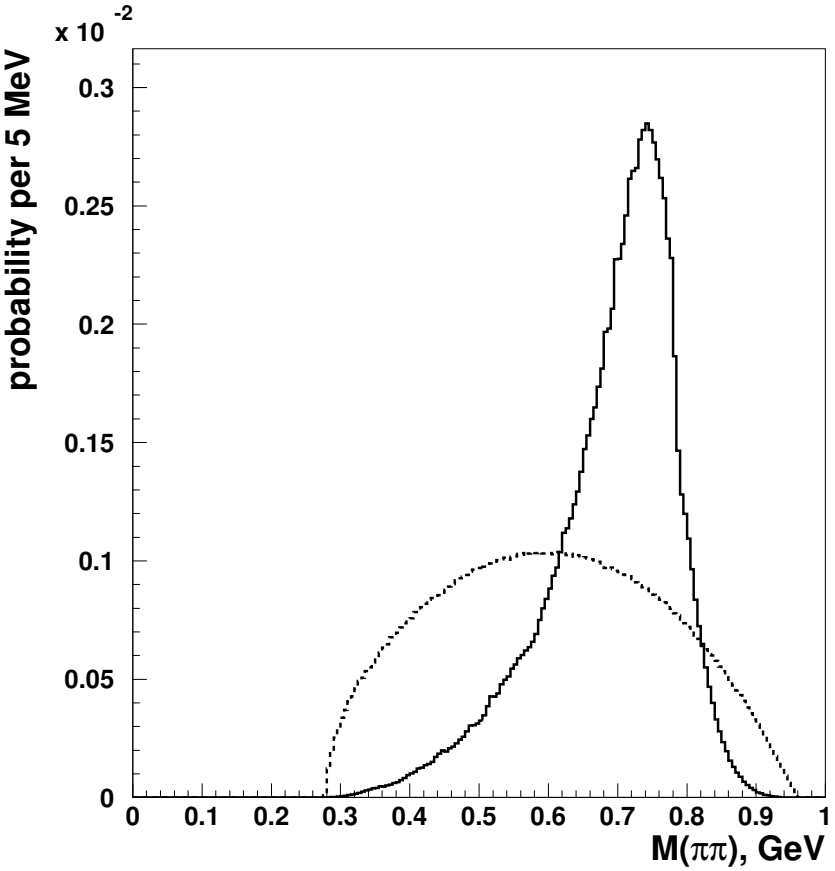

FIG. 66. Inv. mass distrubution for two pions from $\eta' \to \pi^+\pi^-\gamma$ decay. Dashed histogram - decay according to phase space, solid histogram - according to function $f(m)$ in Eqn. 53, i.e. decay with matrix element and parameters $\alpha, \beta = 0$.

Eqn. 53 can be written in the following form:

$$\frac{\partial \Gamma}{\partial m} = C_{\alpha\beta} f(m) + 2\alpha C_{\alpha\beta} f(m) m^2 + (\alpha^2 + 2\beta) C_{\alpha\beta} f(m) m^4 + 2\alpha\beta C_{\alpha\beta} f(m) m^6 + \beta^2 C_{\alpha\beta} f(m) m^8 \tag{56}$$

Now let's define the following functions and their normalization:

$$F_n(m) \equiv C_n \cdot f(m) \cdot m^{2n}, \tag{57}$$

such that

$$\int_{m_{min}}^{m_{max}} F_n(m)\ dm = 1, \tag{58}$$

where $n = 0, 1, 2, 3, 4$.
We also need to define additional parameters:

$$I_n \equiv \int_{m_{min}}^{m_{max}} F_0(m) m^{2n}\ dm \tag{59}$$

and note that $I_n = \frac{C_0}{C_n}$ because:

$$I_n = \int_{m_{min}}^{m_{max}} C_0 f(m) m^{2n}\ dm = \frac{C_0}{C_n} \int_{m_{min}}^{m_{max}} C_n f(m) m^{2n}\ dm \tag{60}$$

and the last integral in this equation is equal to 1 according to our definitions (Eqn. 57). Using all these equations we can again rewrite formula (Eqn. 56):

$$\frac{\partial \Gamma}{\partial m} = C\{F_0(m) + 2\alpha I_1 F_1(m) + (\alpha^2 + 2\beta) I_2 F_2(m) + 2\alpha\beta I_3 F_3(m) + \beta^2 I_4 F_4(m)\} \tag{61}$$

where $C \equiv \frac{C_\alpha}{C_0}$, and $C = (1 + 2\alpha I_1 + (\alpha^2 + 2\beta) I_2 + 2\alpha\beta I_3 + \beta^2 I_4)^{-1}$ due to normaization.

Function $F_0(m)$ (Eqn. 57) can be numericaly obtained from $\eta' \to \pi^+\pi^-\gamma$ decay simuation: it simply equals to m ($M_{\pi^+\pi^-}$) distribution function normalized to 1 and generated with parameters α, β in matrix element reset to zero. Other functions $F_n(m)$ in Eqn. 57 and parameters in Eqn. 59 can be numericaly calculated using known shape of $F_0(m)$. The

obtained shapes of these functions are shown on FIG. 67, with the following values of parameters: I_1=0.486, I_2=0.252, I_3=0.136 and I_4=0.076.

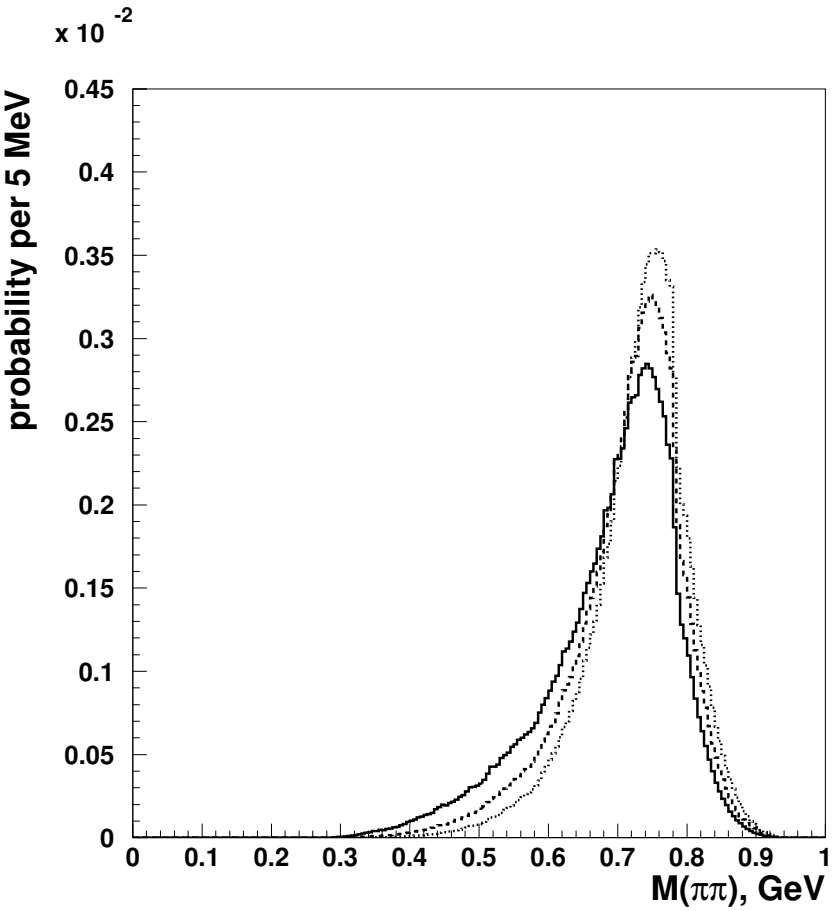

FIG. 67. Simulation result for functions $F_0(m)$ - solid histogram, $F_1(m)$ - dashed histogram, $F_2(m)$ - dotted histogram

Before using the function of Eqn. 61 in the fitting procedure it should be convoluted with the detector acceptance and resolution function $r(m, m_{meas.})$, see Sec. 4.7.2, (index *meas.* denotes the measured value of the quantity):

$$\frac{\partial \Gamma}{\partial m_{meas.}}(m_{meas.}) = \int_{m_{min}}^{m_{max}} \frac{\partial \Gamma}{\partial m}(m) \cdot r(m, m_{meas.})\, dm \tag{62}$$

The function $r(m, m_{meas.})$ was obtained from `MC` simulations (see FIG. 46). Thus to extract parameters α and β from two pion mass distribution observed in the data we can

use fitting function $\frac{\partial \Gamma}{\partial m_{meas.}}$ (Eqn. 62).

5.2.2 FITTING PROCEDURE

The aforementioned formalism was coded in C++ program. The program is designed to call the `MINUIT` minimization package in the `CERNLIB` library [57] and fits Eqn. 62 to determine the parameters α and β.

In the `MINUIT`, the minimization algorithm used is called `MIGRAD`. This uses a variation method suited for minimizing a function $F(\vec{x})$ of n variables $\vec{x}^T = (x_1, x_2, ..., x_n)$ where the gradient vector $\nabla_x F = \vec{g}(\vec{x})$ can be obtained explicitly. The variation method uses an iterative approach to minimize $F(\vec{x})$. Each iteration starts at some point $\vec{x}$ with gradient $\vec{g}(\vec{x})$. The objective is to find another point, $\vec{y}$, such that $F(\vec{y}) < F(\vec{x})$. This procedure is then repeated until the convergence criteria, $\delta F \equiv F(\vec{x}) - F(\vec{y}) < tolerance$, is met. For more information on the minimization algorithm see [58].

5.2.3 PHYSICS RESULTS OF $M_{\pi\pi}$ DISTRIBUTION

Using resolution and acceptance obtained from large statistics Monte-Carlo (section 4.7.2) in Eqn. 62 we performed the fit with the *log likelihood* option [47] to our data to extract free parameters α and β (FIG. 68). The final results of the fit give $\alpha = 1.13 \pm 0.20$ GeV^{-2} and $\beta = -1.39 \pm 0.21$ GeV^{-4} with $\chi^2/Ndof = \frac{134.6}{116} = 1.16$.

If we force both parameters to be zero, the data can not be properly fitted as $\chi^2/Ndof$ shoots up to 3.87, FIG. 69. Note the kink from the shape of the square of the pion vector form factor $|F_V(S_{\pi\pi})|^2$ reflected in FIG. 65.

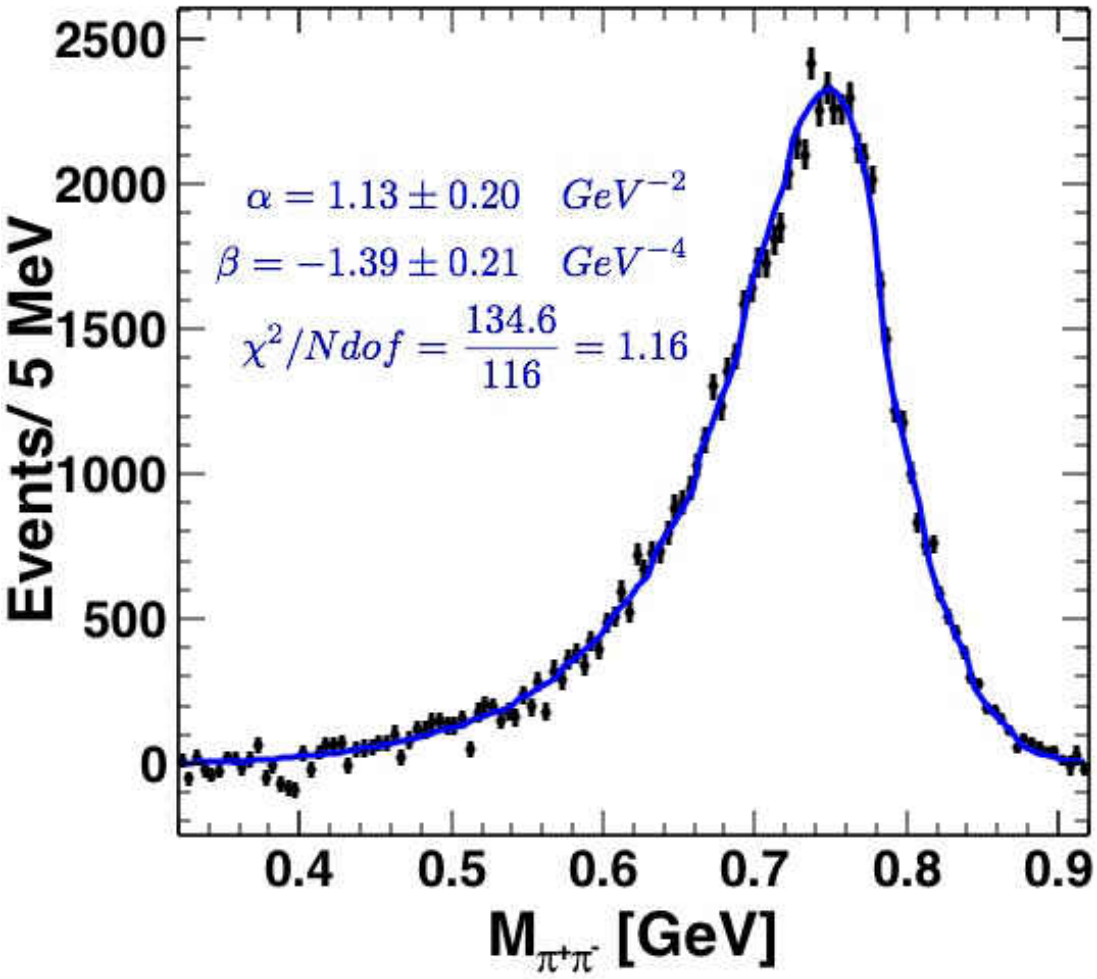

FIG. 68. Fit to acceptance corrected $M_{\pi^+\pi^-}$ distribution for the exclusive reaction $\gamma p \to p\eta'$ ($\eta' \to \pi^+\pi^-\gamma$) of the g11 dataset.

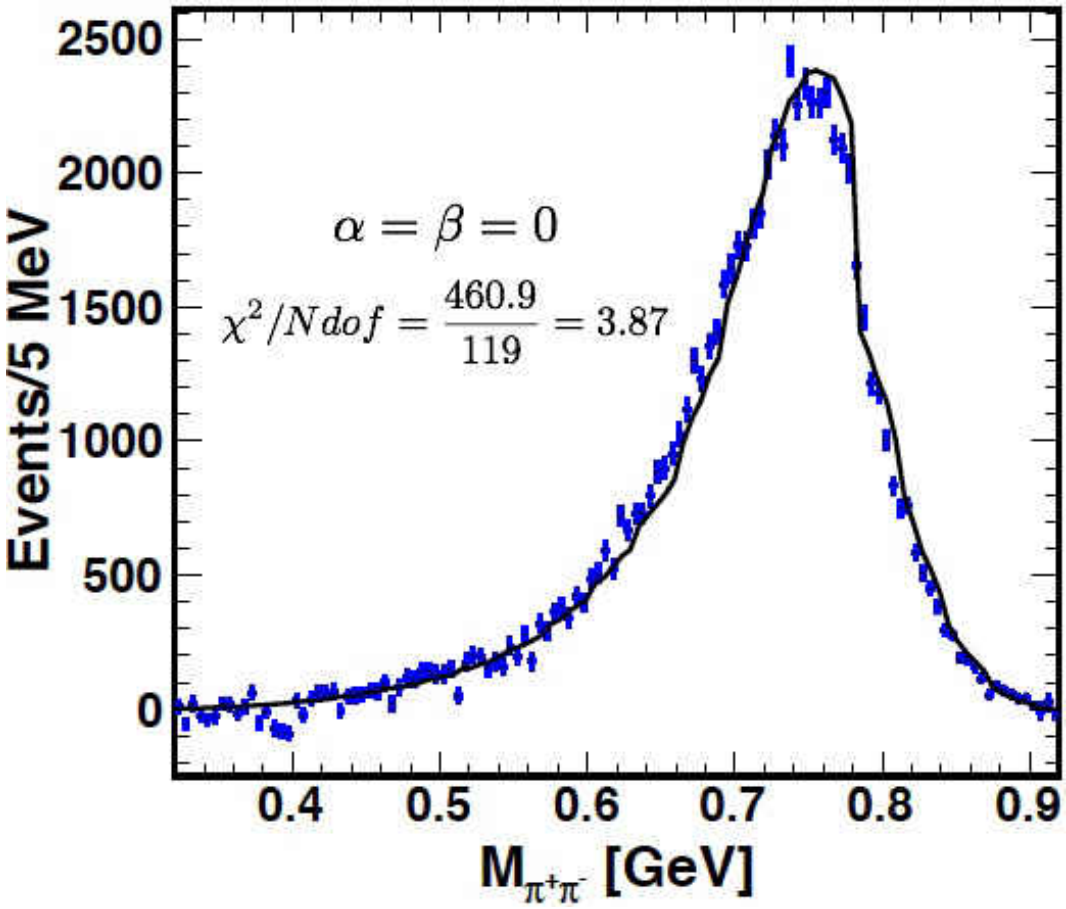

FIG. 69. Fit to $M_{\pi^+\pi^-}$ distribution with both α and β fixed to zero.

5.3 SYSTEMATIC UNCERTAINTIES

The systematic uncertainties were estimated by varying each cut used in the event selection process. In addition the selected events were split into two run periods.

Below, we re-list the stantard cuts applied to our analysis leading to $\alpha = 1.13 \pm 0.20$ GeV^{-2} and $\beta = -1.39 \pm 0.21$ GeV^{-4} ($\chi^2/Ndof = \frac{134.6}{116}$):

- $|M_X(p\pi^+\pi^-\gamma)|^2 < 0.0005$ GeV^2
- $|M_E(p\pi^+\pi^-) - P_\gamma| < 0.12$ GeV
- $M_E(p\pi^+\pi^-) > 0.1$ GeV
- $P_\gamma > 0.1$ GeV
- $|M_X(p) - M(\eta')| < 0.015$ GeV
- $|M(\pi^+\pi^-\gamma) - M(\eta')|$ not applied
- $-0.65 < \cos\theta^{\eta'}_{CM} < 0.85$

Each cut based systematic uncertainty was performed individually, that is when a cut is changed, the remaining cuts maintained their original values. Lets denote the original fit parameters as ζ_o and the new fit parameters obtained after the implementation of a new cut as ζ_n, then the systematic error is calculated as

$$\delta\zeta = \frac{|\zeta_o - \zeta_n|}{\zeta_o} = \frac{\Delta\zeta}{\zeta_o} \tag{63}$$

Table 9 shows changes in the fit parameters with cut variations.

Cut variation	$\Delta\alpha$ $(\text{GeV})^{-2}$	$\Delta\beta$ $(\text{GeV})^{-4}$
$\lvert M_X(p\pi^+\pi^-\gamma)\rvert^2 < 0.00055$ GeV^2	-0.042	+0.049
$\lvert M_X(p\pi^+\pi^-\gamma)\rvert^2 < 0.00045$ GeV^2	+0.025	-0.023
$\lvert M_E(p\pi^+\pi^-) - P_\gamma\rvert < 0.15$ GeV	-0.014	-0.011
$\lvert M_E(p\pi^+\pi^-) - P_\gamma\rvert < 0.10$ GeV	+0.046	-0.065
$M_E(p\pi^+\pi^-) > 0.12$ GeV	+0.021	-0.013
$M_E(p\pi^+\pi^-) > 0.07$ GeV	+0.002	-0.01
$P_\gamma > 0.2$ GeV	+0.035	-0.028
$\lvert M_X(p) - M(\eta')\rvert < 0.012$ GeV	-0.051	+0.068
$\lvert M_X(p) - M(\eta')\rvert < 0.017$ GeV	+0.043	-0.062
$\lvert M(\pi^+\pi^-\gamma) - M(\eta')\rvert < 0.1$ GeV	+0.034	-0.028
$-0.7 < \cos\theta^{\eta'}_{CM} < 0.9$	+0.004	+0.014
$-0.6 < \cos\theta^{\eta'}_{CM} < 0.8$	+0.062	+0.073

TABLE 9. Cut variations and changes in fit parameters.

Run periods	$\Delta\alpha$ $(\text{GeV})^{-2}$	$\Delta\beta$ $(\text{GeV})^{-4}$
First 285 runs	+0.005	+0.055
Second 285 runs	-0.059	+0.073

TABLE 10. Run periods.

Table 11 shows the systematics for each variable and the total systematics each calculated by adding in quadrature as follows

$$\delta\zeta = \sqrt{\sum_i \left(\frac{\Delta\zeta_i}{\zeta_o}\right)^2}, \tag{64}$$

and

$$\sigma_{tot} = \sqrt{\sum_i \delta\zeta_i^2}. \tag{65}$$

Source	$\delta\alpha$	$\delta\beta$
$\lvert M_X(p\pi^+\pi^-\gamma)\rvert^2$	4.33×10^{-2}	3.89×10^{-2}
$\lvert M_E(p\pi^+\pi^-) - P_\gamma\rvert$	4.26×10^{-2}	4.74×10^{-2}
$M_E(p\pi^+\pi^-)$	1.87×10^{-2}	1.18×10^{-2}
P_γ	9.59×10^{-4}	4.06×10^{-4}
$\lvert M_X(p) - M(\eta')\rvert$	5.90×10^{-2}	6.62×10^{-2}
$\lvert M(\pi^+\pi^-\gamma) - M(\eta')\rvert$	9.05×10^{-4}	4.06×10^{-4}
$\cos\theta^{\eta'}_{CM}$	5.50×10^{-2}	5.63×10^{-2}
Run times	1.79×10^{-2}	6.58×10^{-2}
Total Systematic	1.15×10^{-1}	1.26×10^{-1}

TABLE 11. Systematics for each variation.

5.4 COMPARISON WITH PREVIUOS DATA AND THEORY

The most recent high statistics study [59] ($\simeq$ 8000 events) of this η' spectrum measured in the reactions $p\bar{p} \to \pi^0\pi^0\eta'$, $p\bar{p} \to \pi^+\pi^-\eta'$ and $p\bar{p} \to \omega\eta'$, has been done at Crystal Barrel, using two parametrizations of the ρ meson without including contributions from ω and effects of the a_2 tensor meson in the $\pi\eta$ system. This experiment confirmed the existence of box anomaly with a statistical significance of 4σ and that the box anomaly allowed to find the ρ^0 mass in $\eta' \to \pi^+\pi^-\gamma$ decay at values expected from $e^+e^- \to \pi^+\pi^-$ annihilation [60]. FIG. 70 shows a comparison of `CLAS` data scaled to fit the Crystal Barrel data.

From theory a dispersive analysis of the anomalous η' decay process $\eta' \to \pi^+\pi^-\gamma$ by the effects of a_2 was done, arriving at a strong motivation to further scrutinize the physics of light mesons (from higher statistic data) relevant for hadronic corrections to the muon's anomalous magnetic moment. FIG. 71 shows our result compared to the most recent theoretical prediction [21].

Table 12 shows comparisons to world data and theory.

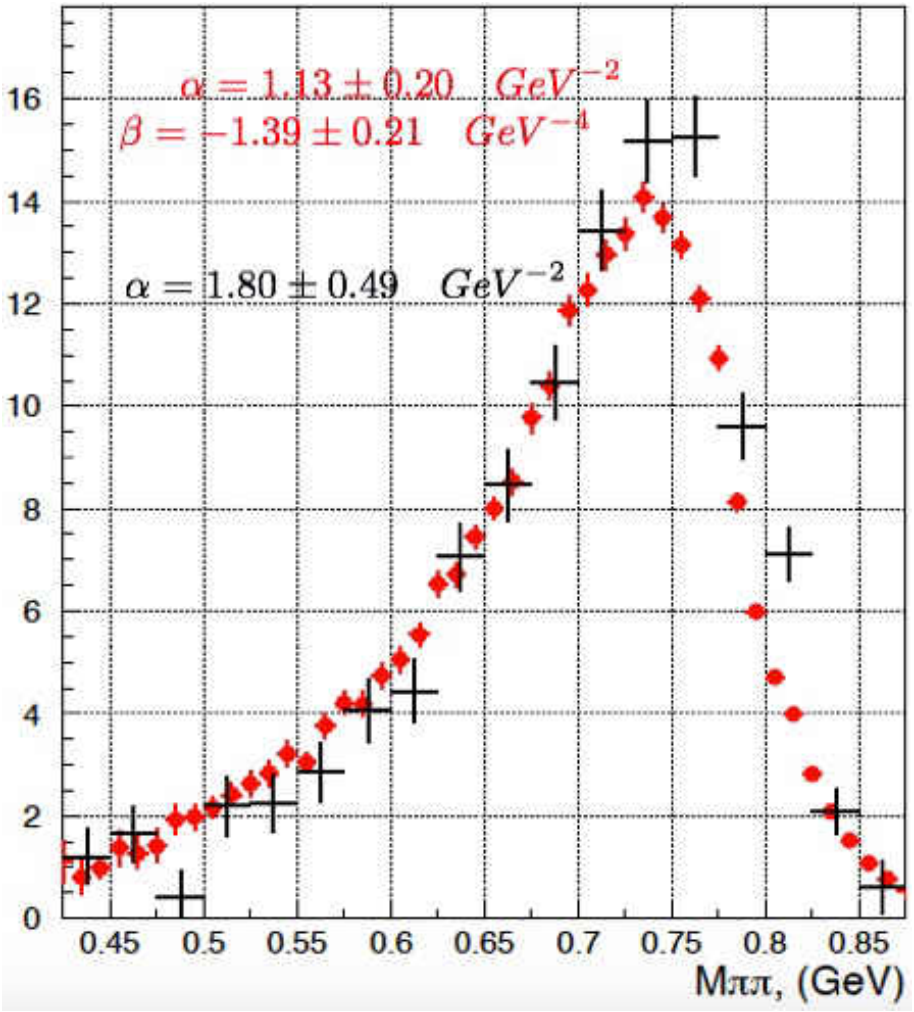

FIG. 70. Comparison of CLAS data (red dotes) with Crystal Barrel data (black crosses). The CLAS data was scaled to fit the Crystal Barrel data [59].

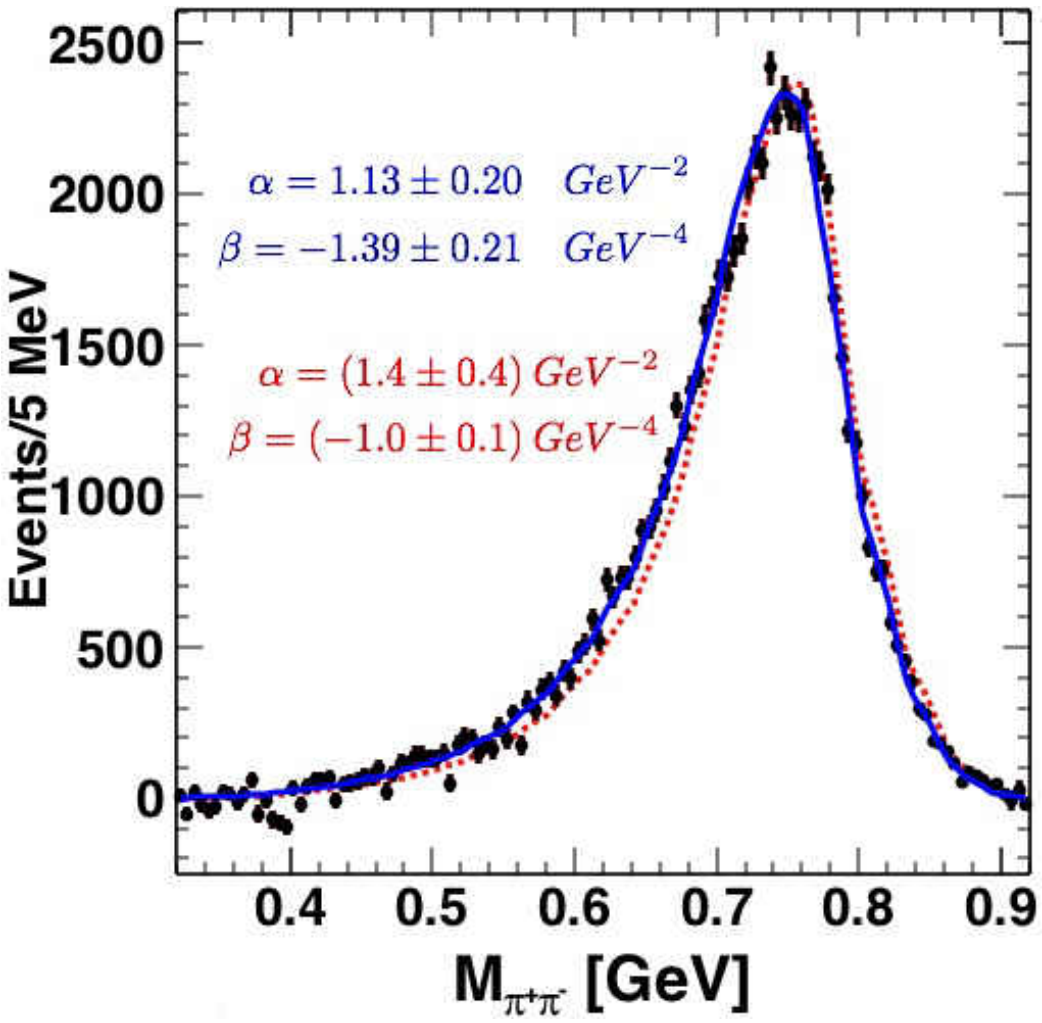

FIG. 71. Comparison of CLAS data (solid line fit) with theoretical prediction from [21] (dotted).

Experiment	α [GeV^{-2}]	β [GeV^{-4}]
GAMS-200 (1990)	2.7 ± 1.0	
CRYSTAL BARREL (1997)	$1.80 \pm 0.49 \pm 0.04$	
CLAS(g11) (2017)	$1.13 \pm 0.20 \pm 0.12$	$-1.39 \pm 0.21 \pm 0.13$
Theory		
Kubis (2015)	1.4 ± 0.4	-1.0 ± 0.1

TABLE 12. Experimental and theoritical results compared.

5.5 SUMMARY

The η' meson photoproduction cross sections has been measured before in CLAS from the $g11$ data for the decay mode $\eta' \to \pi^+\pi^-\eta$ and our work for the decay mode $\eta' \to \pi^+\pi^-\gamma$ is in very good agreement with the previous measurement for an extensive angular coverage. With the inclusion of this work, the world data on BR ratio of $\eta' \to \pi^+\pi^-\gamma$ will be potentially improved with our high statistics data. The affirmation to the published η' differential cross section information will give more insight to possible resonance couplings to the $p\eta'$ channel.

For the first time in CLAS, we have also extracted two free parameters, α and β, from a model-independent fit to the $m(\pi^+\pi^-)$ distribution of the anomalous decay $\eta' \to \pi^+\pi^-\gamma$. The values obtained are found to agree well with recent theoretical expectations. The results of both parameters confirm the existence of the box anomaly, ρ-ω mixing and the effects of the $a_2(1320)$ tensor meson (the lowest-lying resonance) that can contribute into $\pi^+\pi^-\gamma$ system.

BIBLIOGRAPHY

[1] N. P. Samios, Phys. Rev. **121**, 275 (1961)

[2] I. Larin *et al.*, A New Measurement of the π^0 Radiative Decay Width Phys. Rev. Lett. **106** 162303 (2011) [arXiv:1009.1681 [nucl-ex]]

[3] S. Benić it et al., arXiv: 1109.3140

[4] Y. M. Antipov, V. A. Batarin, V. A. Bezzubov, N. P. Budanov, Y. P. Gorin, Y. A. Gornushkin, S. P. Denisov, S. V. Klimenko *et al.*, Phys. Rev. **D36** (1987) 21

[5] P. Abbon *et al.* [COMPASS Collaboration], Nucl. Instrum. Meth. A **577**, 455 (2007) [arXiv:hep-ex/0703049].

[6] S. L. Adler, Phys. Rev. **177**, 2426 (1969)

[7] Particle Data Group, C. Amsler *et al.*, Phys. Lett. B667, 1 (2008)

[8] B. R. Holstein, Phys. Scripta **T99**, 55 (2002), hep-ph/0112150

[9] R. P. Feynman, Quantum Electrodynamics (Benjamin, 1961)

[10] G. F. Chew, M. L. Goldberger, F. E. Low, and Y. Nambu, Phys. Rev. 106, 1345 (1957)

[11] J. S. Bell *et al.*, **A60**, 47 (1969)

[12] M. E. Peskin, D. V. Schroeder, *An Introduction to Quantum Field Theory* (Addison-Wesley, USA, 1995)

[13] J. D. Bjorken and S. D. Drell, Bibliograph Inst./Mannheim 1967

[14] J. Wess and B. Zumino, Phys. Lett. B37, 95 (1971)

[15] E. Witten, Nucl. Phys. B223, 422 (1983)

[16] Thimo Petri, Anomalous Decays of Pseudoscalar Mesons, PhD thesis Institut für Kernphysik, Forschungszentrum Jülich 2010

[17] C. Hanhart *et al.* arXiv:1611.09359v1 (2016)

[18] B. Kubis and J. Plenter, Eur. Phys. J. C 75, 283 (2015) [arXiv:1504.02588 [hep-ph]]

[19] D. Babusci et al. [KLOE Collaboration], Phys. Lett. B 718, 910 (2013) [arXiv:1209.4611 [hep-ex]]

[20] P. Adlarson *et al.* (WASA@COSY Collaboration), Phys. Lett. **B707**, 243 (2012), 1107.5277

[21] B. Kubis *et al.* Eur. Phys. J. C75 (2015) no. 6, 283

[22] F. Ambrosino et al., Physics Letters B, Vol. 700 (2011), p 102-110

[23] C. Leemann, D. Douglas, G. Krafft. The Continuous Electron Beam Accelerator Facility: CEBAF at the Jefferson Laboratory. Annu. Rev. Nucl. Part. Sci., Vol. 51, p 413-450, 2001

[24] M. Battaglieri *et al.* Spectroscopy of Exotic Baryons with CLAS: Search for ground and first excited states. CLAS Analysis Proposal PRO4-021 (2004) Nucl. Inst. Meth. A 440, 263 (2000)

[25] M. Battaglieri *et al.* Study of Pentaquark States in Photoproduction off Protons, CLAS Experiment Proposal E-04-017

[26] `https://www.flickr.com/photos/jeffersonlab/12614907725/`. CEBAF 2013_V2, 2013

[27] Micheal Kunkel, Photoproduction of π^0 on Hydrogen with CLAS from 1.1 GeV - 5.45 GeV using $e^+e^-\gamma$ Decay, PhD thesis Old Dominion University 2014

[28] B.M. Dumham. Jefferson Lab, a status report, 1997

[29] D. I. Sober *et al.* The bremsstrahlung tagged photon beam in Hall B at JLab. Nucl. Inst. Meth. A 440, 263 (2000)

[30] Sober D. I. *et al.*. The bremsstrahlung tagged photon beam in Hall `B` at JLab. Nucl. Instr. and Meth. A, Vol 440, p 263-284, 2000

[31] J. Li. The New Tagger Calibration Program. CLAS-NOTE, 2003-004

[32] B. A.Mecking *et al.*. The `CEBAF` Large Acceptance Spectrometer (`CLAS`). Nucl. Instr. and Meth. A, Vol 503, p 513, 2003

[33] Y. G. Sharabian *et al.*. A new highly segmented start counter for the `CLAS` detector. Nucl. Instr. and Meth. A, Vol 556, p 246-258, 2006

[34] M. Mestayer *et al.*. The CLAS Drift Chamber System. Nucl. Instr. and Meth. A, Vol 449, p 81-111, 2000

[35] Lawrence, David and Mestayer, Mac. `CLAS` Drift Chamber Calibration: Software and Procedures. CLAS-NOTE, 1999-018

[36] E. Smith *et al.*, Nucl. Inst. Meth. A 432, 265 (1999)

[37] E. S. Smith *et al.*. The Time-Of-Flight System for `CLAS`. Nucl. Instr. and Meth. A, Vol 432, p 265-298, 1999

[38] G. Adams *et al.*. The CLAS Cherenkov detector. Nucl. Instr. and Meth. A, Vol 465, p 81-111, 2000

[39] M. Amarian *et al.*. The CLAS Forward Electromagnetic Calorimeter. Nucl. Instr. and Meth. A, Vol 460, p 239, 2001

[40] M. Battaglieri and R. De Vita. The g11 Triggers efficiency. Private Communication (2005)

[41] M. Ungaro, R. De Vita and L. Elouadrhiri. g11 data processing. CLAS Note 2005-014

[42] E. Pasyuk. Energy loss corrections for charged particles in CLAS. CLAS-NOTE, 2007-016

[43] V. Kubarovsky, http://www.jlab.org/Hall-B/secure/g11/valery/note/ valery note.ps.gz

[44] M. Williams, D. Applegate and C.A. Meyer. Determining Momentum and Energy Corrections for g1c Using Kinematic Fitting. CLAS Note 2004-017

[45] D. Sober, H. Crannell and and F.J. Klein. The Tagger Energy Scale: Interpreting the CMU Kinematic Fit Results. CLAS Note 2004-019

[46] S. Stepanyan. Evidence for an Exotic Pentaquark Baryon State $\Theta^+(1530)$, in the $\gamma d \to pK^+K^-n$ reaction. CLAS Analysis Note 2003-105

[47] Mike Williams, Measurement of Differential Cross Sections and Spin Density Matrix Elements along with a Partial Wave Analysis for $\gamma p \to p\omega$ using CLAS at Jefferson Lab, PhD thesis Carnegie Mellon University 2007

[48] Heghine Seraydaryan, Photoproduction of the $\phi(1020)$ Meson in Neutral Decay Mode $\gamma p \to \phi p \to K_S K_L p$, PhD thesis Old Dominion University 2011

[49] J. Ball and E. Pasyuk. Photon Flux Determination Through Sampling of "out-of-time" Hits with the Hall B Photon Tagger. CLAS Note 2005-002

[50] R. De Vita, M. Battaglieri, CLAS Note No. 2009-105, 2009

[51] /mss/clas/g11a/production/pass1/v1/trip

[52] M. Williams *et al.* [CLAS Collaboration], Phys. Rev. C **80**, 045213 (2009)

[53] T. K. Pedlar *et al.* [CLEO Collaboration], Phys. Rev. D **79**, 111101 (2009) doi:10.1103/PhysRevD.79.111101 [arXiv:0904.1394 [hep-ex]]

[54] P. Adlarson et al., Physics Letters B, Vol. 707 (2012), p 243-249

[55] F. Stollenwerk et al., Physics Letters B, Vol. 707 (2012), p 184-190

[56] R.R. Akhmetshin et al., Physics Letters B, Vol. 648 (2007), p 28-38

[57] F. James. MINUIT: Function Minimization and Error Analysis. CERN Program Library D506 (1998)

[58] R. Fletcher and M.J.D. Powell. A rapidly converging descent method for minimization. Comput. J 6, 163 (1963)

[59] A. Abele *et al.* (Crystal Barrel Collaboration), Phys. Lett. **B402**, 195 (1997)

[60] L.M. Barkov *et al.*, Nucl. Phys. B 256 (1985) 365

APPENDIX A

TABULAR DATA

TABLE 13. $\frac{d\sigma}{d\Omega}$ data for $W = 1.965 \pm 0.005$ GeV

$\cos\theta^{\eta'}_{cm}$	$\pm d\cos\theta^{\eta'}_{cm}$	$\frac{d\sigma}{d\Omega}\left[\frac{\mu b}{sr}\right]$	$\Delta\left(\frac{d\sigma}{d\Omega}\right)$
-0.6125	0.0375	0.06039752	0.006039635
-0.5375	0.0375	0.05317042	0.005316483
-0.4625	0.0375	0.07486979	0.007486788
-0.3875	0.0375	0.05469645	0.005471025
-0.3125	0.0375	0.06058728	0.006100342
-0.2375	0.0375	0.0635877	0.00634998
-0.1625	0.0375	0.0545789	0.00545801
-0.0875	0.0375	0.05769554	0.005770154
-0.0125	0.0375	0.06302402	0.006301865
0.0625	0.0375	0.05697672	0.005694227
0.1375	0.0375	0.0860348	0.00898436
0.2125	0.0375	0.07389437	0.007394837
0.2875	0.0375	0.08677573	0.008956362
0.3625	0.0375	0.07177166	0.006999843
0.4375	0.0375	0.05960176	0.005959694
0.5125	0.0375	0.08324076	0.008363499
0.5875	0.0375	0.06118819	0.006174867
0.6625	0.0375	0.05982341	0.005954583
0.7375	0.0375	0.0554771	0.00574867
0.8125	0.0375	0.06931417	0.006958728

TABLE 14. $\frac{d\sigma}{d\Omega}$ data for $W = 1.975 \pm 0.005$ GeV

$\cos\theta^{\eta'}_{cm}$	$\pm d\cos\theta^{\eta'}_{cm}$	$\frac{d\sigma}{d\Omega}\left[\frac{\mu b}{sr}\right]$	$\Delta\left(\frac{d\sigma}{d\Omega}\right)$
-0.6125	0.0375	0.02140342	0.002395524
-0.5375	0.0375	0.03838949	0.003824076
-0.4625	0.0375	0.06759843	0.006039752
-0.3875	0.0375	0.07428759	0.007477573
-0.3125	0.0375	0.07150523	0.006302402
-0.2375	0.0375	0.06862579	0.006118819
-0.1625	0.0375	0.07427985	0.007389437
-0.0875	0.0375	0.06140342	0.006140342
-0.0125	0.0375	0.08346937	0.008177166
0.0625	0.0375	0.0738725	0.00748697
0.1375	0.0375	0.08222747	0.008324076
0.2125	0.0375	0.07974887	0.007394837
0.2875	0.0375	0.07883179	0.006450839
0.3625	0.0375	0.07741286	0.007486788
0.4375	0.0375	0.08571341	0.008346937
0.5125	0.0375	0.07624314	0.007394837
0.5875	0.0375	0.07978077	0.007741286
0.6625	0.0375	0.07767853	0.007978077
0.7375	0.0375	0.05183729	0.007624314
0.8125	0.0375	0.06450839	0.007883179

TABLE 15. $\frac{d\sigma}{d\Omega}$ data for $W = 1.985 \pm 0.005$ GeV

$\cos\theta^{\eta'}_{cm}$	$\pm d\cos\theta^{\eta'}_{cm}$	$\frac{d\sigma}{d\Omega}\left[\frac{\mu b}{sr}\right]$	$\Delta\left(\frac{d\sigma}{d\Omega}\right)$
-0.6125	0.0375	0.06103414	0.005288554
-0.5375	0.0375	0.0736816	0.008383631
-0.4625	0.0375	0.04852055	0.004626232
-0.3875	0.0375	0.06546507	0.00638428
-0.3125	0.0375	0.07187053	0.00727756
-0.2375	0.0375	0.06031146	0.008275089
-0.1625	0.0375	0.08831324	0.009173434
-0.0875	0.0375	0.07309996	0.00723881
-0.0125	0.0375	0.09416297	0.00960655
0.0625	0.0375	0.06660266	0.00623425
0.1375	0.0375	0.07331361	0.00725076
0.2125	0.0375	0.0747347	0.009805234
0.2875	0.0375	0.06808763	0.007533036
0.3625	0.0375	0.07573305	0.007463966
0.4375	0.0375	0.06917511	0.00616626
0.5125	0.0375	0.08821015	0.00822539
0.5875	0.0375	0.06946776	0.0060639
0.6625	0.0375	0.07517381	0.0073087
0.7375	0.0375	0.06568973	0.00627649
0.8125	0.0375	0.05566317	0.00593396

TABLE 16. $\frac{d\sigma}{d\Omega}$ data for $W = 1.995 \pm 0.005$ GeV

$\cos\theta^{\eta'}_{cm}$	$\pm d\cos\theta^{\eta'}_{cm}$	$\frac{d\sigma}{d\Omega}\left[\frac{\mu b}{sr}\right]$	$\Delta\left(\frac{d\sigma}{d\Omega}\right)$
-0.6125	0.0375	0.03525703	0.003103414
-0.5375	0.0375	0.05589088	0.00736816
-0.4625	0.0375	0.06417488	0.004852055
-0.3875	0.0375	0.08256188	0.006546507
-0.3125	0.0375	0.0751837	0.007187053
-0.2375	0.0375	0.05516726	0.006031146
-0.1625	0.0375	0.06115622	0.006831324
-0.0875	0.0375	0.07492539	0.007309996
-0.0125	0.0375	0.07071035	0.007416297
0.0625	0.0375	0.06822832	0.006660266
0.1375	0.0375	0.08167175	0.007331361
0.2125	0.0375	0.06536823	0.00647347
0.2875	0.0375	0.05022024	0.005808763
0.3625	0.0375	0.06309311	0.006573305
0.4375	0.0375	0.0744417	0.006917511
0.5125	0.0375	0.06816926	0.006821015
0.5875	0.0375	0.07137593	0.006946776
0.6625	0.0375	0.06953913	0.007017381
0.7375	0.0375	0.06184326	0.006568973
0.8125	0.0375	0.07955973	0.007566317

TABLE 17. $\frac{d\sigma}{d\Omega}$ data for $W = 2.005 \pm 0.005$ GeV

$\cos\theta^{\eta'}_{cm}$	$\pm d\cos\theta^{\eta'}_{cm}$	$\frac{d\sigma}{d\Omega}\left[\frac{\mu b}{sr}\right]$	$\Delta\left(\frac{d\sigma}{d\Omega}\right)$
-0.6125	0.0375	0.05821417	0.005008077
-0.5375	0.0375	0.04973809	0.004634119
-0.4625	0.0375	0.05231525	0.005387528
-0.3875	0.0375	0.06972187	0.006480262
-0.3125	0.0375	0.07064737	0.00643113
-0.2375	0.0375	0.05534458	0.00560519
-0.1625	0.0375	0.06208323	0.006256011
-0.0875	0.0375	0.06482619	0.00686561
-0.0125	0.0375	0.06843199	0.00645587
0.0625	0.0375	0.07891417	0.00718669
0.1375	0.0375	0.0633669	0.00615405
0.2125	0.0375	0.07511355	0.00728079
0.2875	0.0375	0.06444787	0.00602108
0.3625	0.0375	0.07598692	0.00738338
0.4375	0.0375	0.08227851	0.00868224
0.5125	0.0375	0.08327643	0.00836425
0.5875	0.0375	0.06785467	0.0065083
0.6625	0.0375	0.06760388	0.00604801
0.7375	0.0375	0.07604692	0.00782543
0.8125	0.0375	0.05811399	0.00597372

TABLE 18. $\frac{d\sigma}{d\Omega}$ data for $W = 2.015 \pm 0.005$ GeV

$\cos\theta^{\eta'}_{cm}$	$\pm d\cos\theta^{\eta'}_{cm}$	$\frac{d\sigma}{d\Omega}\left[\frac{\mu b}{sr}\right]$	$\Delta\left(\frac{d\sigma}{d\Omega}\right)$
-0.6125	0.0375	0.05338718	0.005821417
-0.5375	0.0375	0.05089413	0.004973809
-0.4625	0.0375	0.04258352	0.004231525
-0.3875	0.0375	0.04986842	0.004972187
-0.3125	0.0375	0.07620754	0.007064737
-0.2375	0.0375	0.05736793	0.005534458
-0.1625	0.0375	0.05504007	0.006208323
-0.0875	0.0375	0.06577073	0.006482619
-0.0125	0.0375	0.07637246	0.007643199
0.0625	0.0375	0.08124457	0.007891417
0.1375	0.0375	0.07436035	0.00633669
0.2125	0.0375	0.0685386	0.006511355
0.2875	0.0375	0.08680718	0.008444787
0.3625	0.0375	0.07588922	0.007598692
0.4375	0.0375	0.08454829	0.008227851
0.5125	0.0375	0.08242832	0.008327643
0.5875	0.0375	0.08338867	0.008385467
0.6625	0.0375	0.06698673	0.006760388
0.7375	0.0375	0.08550284	0.008504692
0.8125	0.0375	0.08649148	0.008511399

TABLE 19. $\frac{d\sigma}{d\Omega}$ data for $W = 2.025 \pm 0.005$ GeV

$\cos\theta^{\eta'}_{cm}$	$\pm d\cos\theta^{\eta'}_{cm}$	$\frac{d\sigma}{d\Omega}\left[\frac{\mu b}{sr}\right]$	$\Delta\left(\frac{d\sigma}{d\Omega}\right)$
-0.6125	0.0375	0.03914	0.003813141
-0.5375	0.0375	0.06196897	0.006280674
-0.4625	0.0375	0.06603038	0.005208798
-0.3875	0.0375	0.04273526	0.004570041
-0.3125	0.0375	0.0615481	0.006913394
-0.2375	0.0375	0.0654143	0.006639169
-0.1625	0.0375	0.07156413	0.007702073
-0.0875	0.0375	0.06074424	0.006278178
-0.0125	0.0375	0.07342597	0.007373903
0.0625	0.0375	0.06229765	0.006176675
0.1375	0.0375	0.07846701	0.007018508
0.2125	0.0375	0.06909584	0.006578478
0.2875	0.0375	0.07679106	0.007799884
0.3625	0.0375	0.08019667	0.008043127
0.4375	0.0375	0.08848971	0.008107805
0.5125	0.0375	0.08212528	0.008391873
0.5875	0.0375	0.08807202	0.008812295
0.6625	0.0375	0.08420361	0.008426697
0.7375	0.0375	0.09452591	0.00879425
0.8125	0.0375	0.07615122	0.007453953

TABLE 20. $\frac{d\sigma}{d\Omega}$ data for $W = 2.035 \pm 0.005$ GeV

$\cos\theta^{\eta'}_{cm}$	$\pm d\cos\theta^{\eta'}_{cm}$	$\frac{d\sigma}{d\Omega}\left[\frac{\mu b}{sr}\right]$	$\Delta\left(\frac{d\sigma}{d\Omega}\right)$
-0.6125	0.0375	0.05813141	0.005871001
-0.5375	0.0375	0.06280674	0.006295346
-0.4625	0.0375	0.05208798	0.005204557
-0.3875	0.0375	0.07570041	0.007410289
-0.3125	0.0375	0.06913394	0.0069232215
-0.2375	0.0375	0.06639169	0.006512144
-0.1625	0.0375	0.06702073	0.00673462
-0.0875	0.0375	0.06278178	0.006111637
-0.0125	0.0375	0.06373903	0.0060139
0.0625	0.0375	0.07176675	0.007344647
0.1375	0.0375	0.07018508	0.0077005
0.2125	0.0375	0.08578478	0.00836438
0.2875	0.0375	0.07799884	0.00751866
0.3625	0.0375	0.08843127	0.00820295
0.4375	0.0375	0.08107805	0.00807346
0.5125	0.0375	0.09391873	0.00931879
0.5875	0.0375	0.09812295	0.00832108
0.6625	0.0375	0.07726697	0.00763054
0.7375	0.0375	0.1179425	0.01017889
0.8125	0.0375	0.09453953	0.00942268

TABLE 21. $\frac{d\sigma}{d\Omega}$ data for $W = 2.045 \pm 0.005$ GeV

$\cos\theta^{\eta'}_{cm}$	$\pm d\cos\theta^{\eta'}_{cm}$	$\frac{d\sigma}{d\Omega}\left[\frac{\mu b}{sr}\right]$	$\Delta\left(\frac{d\sigma}{d\Omega}\right)$
-0.6125	0.0375	0.04681724	0.004422759
-0.5375	0.0375	0.05234811	0.005503584
-0.4625	0.0375	0.04469055	0.004396619
-0.3875	0.0375	0.05194306	0.005274038
-0.3125	0.0375	0.0491015	0.004999803
-0.2375	0.0375	0.05053788	0.005072388
-0.1625	0.0375	0.06309509	0.005764529
-0.0875	0.0375	0.05395871	0.005188978
-0.0125	0.0375	0.06359103	0.00608369
0.0625	0.0375	0.05763539	0.00587203
0.1375	0.0375	0.06249335	0.00646429
0.2125	0.0375	0.07070159	0.006841989
0.2875	0.0375	0.07530943	0.00701746
0.3625	0.0375	0.07949424	0.00669956
0.4375	0.0375	0.08185483	0.00824478
0.5125	0.0375	0.09956655	0.00953879
0.5875	0.0375	0.0881072	0.00828633
0.6625	0.0375	0.1006342	0.01006057
0.7375	0.0375	0.1013941	0.01005204
0.8125	0.0375	0.09589207	0.0097506

TABLE 22. $\frac{d\sigma}{d\Omega}$ data for $W = 2.055 \pm 0.005$ GeV

$\cos\theta^{\eta'}_{cm}$	$\pm d\cos\theta^{\eta'}_{cm}$	$\frac{d\sigma}{d\Omega}\left[\frac{\mu b}{sr}\right]$	$\Delta\left(\frac{d\sigma}{d\Omega}\right)$
-0.6125	0.0375	0.05615173	0.005681724
-0.5375	0.0375	0.03669056	0.005234811
-0.4625	0.0375	0.04264413	0.004469055
-0.3875	0.0375	0.05516025	0.005194306
-0.3125	0.0375	0.05333202	0.00491015
-0.2375	0.0375	0.05981592	0.005053788
-0.1625	0.0375	0.05843019	0.005309509
-0.0875	0.0375	0.05459319	0.005395871
0.0625	0.0375	0.06581353	0.005763539
0.1375	0.0375	0.0764286	0.007249335
0.2125	0.0375	0.06561326	0.006070159
0.2875	0.0375	0.08011642	0.007530943
0.3625	0.0375	0.08466376	0.007949424
0.4375	0.0375	0.08163188	0.008185483
0.5125	0.0375	0.09692525	0.009956655
0.5875	0.0375	0.09524223	0.00921072
0.6625	0.0375	0.1164038	0.01006342
0.7375	0.0375	0.1150136	0.01013941
0.8125	0.0375	0.07167068	0.007089207

TABLE 23. $\frac{d\sigma}{d\Omega}$ data for $W = 2.065 \pm 0.005$ GeV

$\cos\theta^{\eta'}_{cm}$	$\pm d\cos\theta^{\eta'}_{cm}$	$\frac{d\sigma}{d\Omega}\left[\frac{\mu b}{sr}\right]$	$\Delta\left(\frac{d\sigma}{d\Omega}\right)$
-0.6125	0.0375	0.04213847	0.004476785
-0.5375	0.0375	0.02852335	0.002468452
-0.4625	0.0375	0.03673056	0.003124921
-0.3875	0.0375	0.04818282	0.00408956
-0.3125	0.0375	0.06042725	0.00605826
-0.2375	0.0375	0.05708745	0.005763453
-0.1625	0.0375	0.05544073	0.005135796
-0.0875	0.0375	0.05864837	0.005268965
0.0625	0.0375	0.05394124	0.005191613
0.1375	0.0375	0.0643249	0.006167033
0.2125	0.0375	0.06151588	0.006439373
0.2875	0.0375	0.0855298	0.008491438
0.3625	0.0375	0.07784094	0.00759018
0.4375	0.0375	0.06886086	0.00657301
0.5125	0.0375	0.09697597	0.00957764
0.5875	0.0375	0.08375398	0.00803932
0.6625	0.0375	0.1302786	0.01938016
0.7375	0.0375	0.1121454	0.01986476
0.8125	0.0375	0.1094686	0.01216787

TABLE 24. $\frac{d\sigma}{d\Omega}$ data for $W = 2.075 \pm 0.005$ GeV

$\cos\theta^{\eta'}_{cm}$	$\pm d\cos\theta^{\eta'}_{cm}$	$\frac{d\sigma}{d\Omega}\left[\frac{\mu b}{sr}\right]$	$\Delta\left(\frac{d\sigma}{d\Omega}\right)$
-0.6125	0.0375	0.0365119	0.00332077
-0.5375	0.0375	0.02978968	0.002278502
-0.4625	0.0375	0.04083281	0.004009583
-0.3875	0.0375	0.04726373	0.004227423
-0.3125	0.0375	0.0587055	0.005064087
-0.2375	0.0375	0.06508969	0.006563117
-0.1625	0.0375	0.04757197	0.00431611
-0.0875	0.0375	0.04845977	0.004797255
-0.0125	0.0375	0.05929037	0.005372348
0.0625	0.0375	0.04794409	0.004091185
0.1375	0.0375	0.06111355	0.006148735
0.2125	0.0375	0.05626249	0.005627381
0.2875	0.0375	0.05660959	0.00562947
0.3625	0.0375	0.07726788	0.00767614
0.4375	0.0375	0.07715339	0.00732913
0.5125	0.0375	0.09051761	0.00905464
0.5875	0.0375	0.1069288	0.0105631
0.6625	0.0375	0.129201	0.01254179
0.7375	0.0375	0.1324317	0.01282181
0.8125	0.0375	0.08111912	0.007642029

TABLE 25. $\frac{d\sigma}{d\Omega}$ data for $W = 2.085 \pm 0.005$ GeV

$\cos\theta^{\eta'}_{cm}$	$\pm d\cos\theta^{\eta'}_{cm}$	$\frac{d\sigma}{d\Omega}\left[\frac{\mu b}{sr}\right]$	$\Delta\left(\frac{d\sigma}{d\Omega}\right)$
-0.6125	0.0375	0.02492446	0.002413299
-0.5375	0.0375	0.05067958	0.005013631
-0.4625	0.0375	0.03553381	0.003789708
-0.3875	0.0375	0.04098077	0.004197068
-0.3125	0.0375	0.0333995	0.003220952
-0.2375	0.0375	0.05178476	0.005608883
-0.1625	0.0375	0.06677384	0.006609497
-0.0875	0.0375	0.06682673	0.006632921
-0.0125	0.0375	0.04428886	0.004026875
0.0625	0.0375	0.0704947	0.007001119
0.1375	0.0375	0.05471223	0.00516192
0.2125	0.0375	0.06982348	0.006578394
0.2875	0.0375	0.06059332	0.006073453
0.3625	0.0375	0.09189622	0.009141866
0.4375	0.0375	0.08250698	0.008206254
0.5125	0.0375	0.1081336	0.01022313
0.5875	0.0375	0.1438038	0.01402746
0.6625	0.0375	0.09689141	0.00930714
0.7375	0.0375	0.1320402	0.01261452
0.8125	0.0375	0.09528224	0.01045987

TABLE 26. $\frac{d\sigma}{d\Omega}$ data for $W = 2.095 \pm 0.005$ GeV

$\cos\theta^{\eta'}_{cm}$	$\pm d\cos\theta^{\eta'}_{cm}$	$\frac{d\sigma}{d\Omega}\left[\frac{\mu b}{sr}\right]$	$\Delta\left(\frac{d\sigma}{d\Omega}\right)$
-0.6125	0.0375	0.03613299	0.003738669
-0.5375	0.0375	0.03613631	0.003601937
-0.4625	0.0375	0.02789708	0.002330072
-0.3875	0.0375	0.03197068	0.003147116
-0.3125	0.0375	0.05220952	0.005009925
-0.2375	0.0375	0.05608883	0.005567715
-0.1625	0.0375	0.04609497	0.00401608
-0.0875	0.0375	0.06332921	0.0062401
-0.0125	0.0375	0.05026875	0.005043329
0.0625	0.0375	0.06001119	0.0065021
0.1375	0.0375	0.0616192	0.006206835
0.2125	0.0375	0.06578394	0.00647352
0.2875	0.0375	0.06873453	0.00688998
0.3625	0.0375	0.08541866	0.00878443
0.4375	0.0375	0.08406254	0.0082376
0.5125	0.0375	0.1022313	0.01022004
0.5875	0.0375	0.1302746	0.0141057
0.6625	0.0375	0.1330714	0.01353371
0.7375	0.0375	0.1261452	0.01250603
0.8125	0.0375	0.1045987	0.01042923

TABLE 27. $\frac{d\sigma}{d\Omega}$ data for $W = 2.110 \pm 0.010$ GeV

$\cos\theta^{\eta'}_{cm}$	$\pm d\cos\theta^{\eta'}_{cm}$	$\frac{d\sigma}{d\Omega}\left[\frac{\mu b}{sr}\right]$	$\Delta\left(\frac{d\sigma}{d\Omega}\right)$
-0.6125	0.0375	0.02907782	0.002836502
-0.5375	0.0375	0.0195848	0.001491346
-0.4625	0.0375	0.03547647	0.00356506
-0.3875	0.0375	0.03229984	0.003218025
-0.3125	0.0375	0.04225512	0.004354062
-0.2375	0.0375	0.0447961	0.00422327
-0.1625	0.0375	0.03431915	0.00330044
-0.0875	0.0375	0.05275687	0.00520987
-0.0125	0.0375	0.05866496	0.00569285
0.0625	0.0375	0.05655913	0.00530903
0.1375	0.0375	0.05825958	0.00572905
0.2125	0.0375	0.05995527	0.00595505
0.2875	0.0375	0.05829164	0.005836804
0.3625	0.0375	0.06675728	0.00661902
0.4375	0.0375	0.09603893	0.00933143
0.5125	0.0375	0.09983484	0.009867489
0.5875	0.0375	0.09250242	0.01017034
0.6625	0.0375	0.1178284	0.01138534
0.7375	0.0375	0.1085905	0.01078439
0.8125	0.0375	0.1113461	0.01113661

TABLE 28. $\frac{d\sigma}{d\Omega}$ data for $W = 2.130 \pm 0.010$ GeV

$\cos\theta^{\eta'}_{cm}$	$\pm d\cos\theta^{\eta'}_{cm}$	$\frac{d\sigma}{d\Omega}\left[\frac{\mu b}{sr}\right]$	$\Delta\left(\frac{d\sigma}{d\Omega}\right)$
-0.6125	0.0375	0.02836502	0.002361673
-0.5375	0.0375	0.03491346	0.00335848
-0.4625	0.0375	0.02756506	0.00254767
-0.3875	0.0375	0.03218025	0.003044976
-0.3125	0.0375	0.03554062	0.00353827
-0.2375	0.0375	0.02722327	0.002719415
-0.1625	0.0375	0.0390044	0.003147872
-0.0875	0.0375	0.04420987	0.003913531
-0.0125	0.0375	0.0369285	0.003799744
0.0625	0.0375	0.03930903	0.003483869
0.1375	0.0375	0.04072905	0.004038938
0.2125	0.0375	0.05095505	0.00509329
0.2875	0.0375	0.05236804	0.00513746
0.3625	0.0375	0.0661902	0.00601359
0.4375	0.0375	0.0833143	0.00840584
0.5125	0.0375	0.08067489	0.00807523
0.5875	0.0375	0.1017034	0.01087536
0.6625	0.0375	0.09385349	0.00967426
0.7375	0.0375	0.1178439	0.0118857
0.8125	0.0375	0.1143661	0.01170191

TABLE 29. $\frac{d\sigma}{d\Omega}$ data for $W = 2.150 \pm 0.010$ GeV

$\cos\theta^{\eta'}_{cm}$	$\pm d\cos\theta^{\eta'}_{cm}$	$\frac{d\sigma}{d\Omega}\left[\frac{\mu b}{sr}\right]$	$\Delta\left(\frac{d\sigma}{d\Omega}\right)$
-0.6125	0.0375	0.02219742	0.004221804
-0.5375	0.0375	0.02719673	0.00263556
-0.4625	0.0375	0.02511947	0.00238027
-0.3875	0.0375	0.02390143	0.002304675
-0.3125	0.0375	0.0197142	0.00195767
-0.2375	0.0375	0.025717	0.002374496
-0.1625	0.0375	0.02817169	0.002380625
-0.0875	0.0375	0.02808889	0.002571881
-0.0125	0.0375	0.03811999	0.003623127
0.0625	0.0375	0.02926869	0.002910482
0.1375	0.0375	0.04351689	0.004577788
0.2125	0.0375	0.03988253	0.003885692
0.2875	0.0375	0.04714821	0.004629067
0.3625	0.0375	0.06855668	0.006798056
0.4375	0.0375	0.07454068	0.0071899
0.5125	0.0375	0.0924199	0.0091422
0.5875	0.0375	0.09630208	0.00983223
0.6625	0.0375	0.1025116	0.01036426
0.7375	0.0375	0.1337334	0.01336322
0.8125	0.0375	0.1336763	0.01436692

TABLE 30. $\frac{d\sigma}{d\Omega}$ data for $W = 2.170 \pm 0.010$ GeV

$\cos\theta^{\eta'}_{cm}$	$\pm d\cos\theta^{\eta'}_{cm}$	$\frac{d\sigma}{d\Omega}\left[\frac{\mu b}{sr}\right]$	$\Delta\left(\frac{d\sigma}{d\Omega}\right)$
-0.6125	0.0375	0.02981202	0.002329614
-0.5375	0.0375	0.02242371	0.002279509
-0.4625	0.0375	0.02492018	0.002467921
-0.3875	0.0375	0.02031172	0.002085214
-0.3125	0.0375	0.02238404	0.00225713
-0.2375	0.0375	0.02249664	0.002257549
-0.1625	0.0375	0.0225375	0.00225753
-0.0875	0.0375	0.02381254	0.00213334
-0.0125	0.0375	0.02415418	0.002417999
0.0625	0.0375	0.02206988	0.00220304
0.1375	0.0375	0.03718525	0.003527533
0.2125	0.0375	0.04590461	0.004598237
0.2875	0.0375	0.04086045	0.004072232
0.3625	0.0375	0.0586537	0.0052835
0.4375	0.0375	0.07279329	0.0071811
0.5125	0.0375	0.07276148	0.00738628
0.5875	0.0375	0.07888152	0.00744531
0.6625	0.0375	0.0957617	0.00937674
0.7375	0.0375	0.0924199	0.00906001
0.8125	0.0375	0.1413661	0.01406001

TABLE 31. $\frac{d\sigma}{d\Omega}$ data for $W = 2.190 \pm 0.010$ GeV

$\cos\theta^{\eta'}_{cm}$	$\pm d\cos\theta^{\eta'}_{cm}$	$\frac{d\sigma}{d\Omega}\left[\frac{\mu b}{sr}\right]$	$\Delta\left(\frac{d\sigma}{d\Omega}\right)$
-0.6125	0.0375	0.02341976	0.002665562
-0.5375	0.0375	0.0221043	0.002860849
-0.4625	0.0375	0.01720224	0.00171392
-0.3875	0.0375	0.01907007	0.001907925
-0.3125	0.0375	0.02256621	0.0022022
-0.2375	0.0375	0.01493136	0.001553852
-0.1625	0.0375	0.01856755	0.00188816
-0.0875	0.0375	0.02548382	0.002376192
-0.0125	0.0375	0.02056756	0.002096515
0.0625	0.0375	0.01982932	0.013448607
0.1375	0.0375	0.02691172	0.002579149
0.2125	0.0375	0.03202303	0.00377645
0.2875	0.0375	0.03490448	0.00314329
0.3625	0.0375	0.04423534	0.0048968
0.4375	0.0375	0.05779133	0.0056737
0.5125	0.0375	0.07428567	0.007457776
0.5875	0.0375	0.06645044	0.00644771
0.6625	0.0375	0.07621416	0.0156095
0.7375	0.0375	0.07276148	0.00744531
0.8125	0.0375	0.0924199	0.0091315

TABLE 32. $\frac{d\sigma}{d\Omega}$ data for $W = 2.210 \pm 0.010$ GeV

$\cos\theta^{\eta'}_{cm}$	$\pm d\cos\theta^{\eta'}_{cm}$	$\frac{d\sigma}{d\Omega}\left[\frac{\mu b}{sr}\right]$	$\Delta\left(\frac{d\sigma}{d\Omega}\right)$
-0.6125	0.0375	0.01777041	0.001512964
-0.5375	0.0375	0.01907233	0.0019646
-0.4625	0.0375	0.0140928	0.001380336
-0.3875	0.0375	0.01405283	0.00286051
-0.3125	0.0375	0.01707233	0.00184932
-0.2375	0.0375	0.01468133	0.00139704
-0.1625	0.0375	0.01702568	0.001785132
-0.0875	0.0375	0.01725877	0.001822573
-0.0125	0.0375	0.01584128	0.00185133
0.0625	0.0375	0.0153101	0.00143985
0.1375	0.0375	0.02299071	0.00226758
0.2125	0.0375	0.03719433	0.00303454
0.2875	0.0375	0.03585096	0.003635672
0.3625	0.0375	0.04209552	0.004635301
0.4375	0.0375	0.04565933	0.004668699
0.5125	0.0375	0.06778247	0.00614285
0.5875	0.0375	0.06305184	0.00630567
0.6625	0.0375	0.07631805	0.00743212
0.7375	0.0375	0.1040633	0.01040601
0.8125	0.0375	0.09942097	0.00976741

TABLE 33. $\frac{d\sigma}{d\Omega}$ data for $W = 2.230 \pm 0.010$ GeV

$\cos\theta^{\eta'}_{cm}$	$\pm d\cos\theta^{\eta'}_{cm}$	$\frac{d\sigma}{d\Omega}\left[\frac{\mu b}{sr}\right]$	$\Delta\left(\frac{d\sigma}{d\Omega}\right)$
-0.6125	0.0375	0.01255823	0.001265124
-0.5375	0.0375	0.02481115	0.002485249
-0.4625	0.0375	0.01645079	0.001681163
-0.3875	0.0375	0.01042323	0.00107769
-0.3125	0.0375	0.01281931	0.001340713
-0.2375	0.0375	0.01077704	0.001076179
-0.1625	0.0375	0.01310041	0.0014354
-0.0875	0.0375	0.008984278	0.0008351594
-0.0125	0.0375	0.009706857	0.00097182
0.0625	0.0375	0.0141538	0.001460253
0.1375	0.0375	0.02313719	0.002335908
0.2125	0.0375	0.01476848	0.00143186
0.2875	0.0375	0.02834806	0.002674956
0.3625	0.0375	0.03467844	0.00330862
0.4375	0.0375	0.04518837	0.004067297
0.5125	0.0375	0.05084315	0.0051912
0.5875	0.0375	0.06117879	0.00621372
0.6625	0.0375	0.07473516	0.0072851
0.7375	0.0375	0.09584209	0.00971065
0.8125	0.0375	0.1046391	0.01093835

TABLE 34. $\frac{d\sigma}{d\Omega}$ data for $W = 2.250 \pm 0.010$ GeV

$\cos\theta^{\eta'}_{cm}$	$\pm d\cos\theta^{\eta'}_{cm}$	$\frac{d\sigma}{d\Omega}\left[\frac{\mu b}{sr}\right]$	$\Delta\left(\frac{d\sigma}{d\Omega}\right)$
-0.6125	0.0375	0.01843416	0.001883735
-0.5375	0.0375	0.01190166	0.0011673
-0.4625	0.0375	0.009207755	0.0009673
-0.3875	0.0375	0.01478513	0.001463485
-0.3125	0.0375	0.008938088	0.0009226
-0.2375	0.0375	0.01174527	0.00116556
-0.1625	0.0375	0.009569332	0.00096501
-0.0875	0.0375	0.00556773	0.00054642
-0.0125	0.0375	0.01184788	0.00116028
0.0625	0.0375	0.01306836	0.0013307
0.1375	0.0375	0.01557272	0.0015709
0.2125	0.0375	0.01982124	0.0019272
0.2875	0.0375	0.03116637	0.00325209
0.3625	0.0375	0.0353908	0.003501767
0.4375	0.0375	0.03378198	0.00338256
0.5125	0.0375	0.04127466	0.00426472
0.5875	0.0375	0.05780915	0.00576819
0.6625	0.0375	0.07952335	0.00791027
0.7375	0.0375	0.07807097	0.0077631
0.8125	0.0375	0.1062556	0.01069586

TABLE 35. $\frac{d\sigma}{d\Omega}$ data for $W = 2.270 \pm 0.010$ GeV

$\cos\theta^{\eta'}_{cm}$	$\pm d\cos\theta^{\eta'}_{cm}$	$\frac{d\sigma}{d\Omega}\left[\frac{\mu b}{sr}\right]$	$\Delta\left(\frac{d\sigma}{d\Omega}\right)$
-0.6125	0.0375	0.01616722	0.001675067
-0.5375	0.0375	0.01771956	0.00175425
-0.4625	0.0375	0.006906362	0.000645038
-0.3875	0.0375	0.01059519	0.00105693
-0.3125	0.0375	0.01495268	0.001433285
-0.2375	0.0375	0.009339672	0.000985257
-0.1625	0.0375	0.0101712	0.00102587
-0.0875	0.0375	0.007621692	0.000736082
-0.0125	0.0375	0.006310953	0.000608207
0.0625	0.0375	0.008290208	0.000870364
0.1375	0.0375	0.01219495	0.001269168
0.2125	0.0375	0.02535802	0.0022971
0.2875	0.0375	0.0260708	0.00281652
0.3625	0.0375	0.03983289	0.00399932
0.4375	0.0375	0.03553111	0.00343725
0.5125	0.0375	0.04014345	0.004077039
0.5875	0.0375	0.07374203	0.007199296
0.6625	0.0375	0.08279529	0.00821402
0.7375	0.0375	0.09391621	0.0092867
0.8125	0.0375	0.1102619	0.0112566

TABLE 36. $\frac{d\sigma}{d\Omega}$ data for $W = 2.290 \pm 0.010$ GeV

$\cos\theta^{\eta'}_{cm}$	$\pm d\cos\theta^{\eta'}_{cm}$	$\frac{d\sigma}{d\Omega}\left[\frac{\mu b}{sr}\right]$	$\Delta\left(\frac{d\sigma}{d\Omega}\right)$
-0.6125	0.0375	0.01316711	0.001425083
-0.5375	0.0375	0.006769501	0.000657933
-0.4625	0.0375	0.01630025	0.001635954
-0.3875	0.0375	0.0104623	0.00105898
-0.3125	0.0375	0.01088857	0.0010902
-0.2375	0.0375	0.008568378	0.0009514
-0.1625	0.0375	0.009817246	0.001008
-0.0875	0.0375	0.007573881	0.000743254
-0.0125	0.0375	0.01072138	0.001946429
0.0625	0.0375	0.00913576	0.000943531
0.1375	0.0375	0.01179446	0.001182924
0.2125	0.0375	0.008197997	0.000803703
0.2875	0.0375	0.0187768	0.00191062
0.3625	0.0375	0.01999547	0.001974934
0.4375	0.0375	0.02914834	0.0029666
0.5125	0.0375	0.03318026	0.00341517
0.5875	0.0375	0.05466197	0.006131
0.6625	0.0375	0.06809344	0.00741929
0.7375	0.0375	0.06857801	0.0068743
0.8125	0.0375	0.1083773	0.0106539

TABLE 37. $\frac{d\sigma}{d\Omega}$ data for $W = 2.310 \pm 0.010$ GeV

$\cos\theta^{\eta'}_{cm}$	$\pm d\cos\theta^{\eta'}_{cm}$	$\frac{d\sigma}{d\Omega}\left[\frac{\mu b}{sr}\right]$	$\Delta\left(\frac{d\sigma}{d\Omega}\right)$
-0.6125	0.0375	0.01537126	0.002305689
-0.5375	0.0375	0.005577521	0.0008366281
-0.4625	0.0375	0.01339554	0.00200933
-0.3875	0.0375	0.007929342	0.001189401
-0.3125	0.0375	0.008438152	0.001265723
-0.2375	0.0375	0.0123959	0.001859385
-0.1625	0.0375	0.0115878	0.00173817
-0.0875	0.0375	0.005986869	0.0008980304
-0.0125	0.0375	0.009737564	0.001460635
0.0625	0.0375	0.01068013	0.001602019
0.1375	0.0375	0.01067212	0.001600818
0.2125	0.0375	0.01352945	0.002029417
0.2875	0.0375	0.02556168	0.003834251
0.3625	0.0375	0.02592296	0.003888444
0.4375	0.0375	0.031473	0.00472095
0.5125	0.0375	0.03432272	0.005148408
0.5875	0.0375	0.05358644	0.008037965
0.6625	0.0375	0.06129158	0.009193737
0.7375	0.0375	0.0932304	0.01398456
0.8125	0.0375	0.1136758	0.01705138

TABLE 38. $\frac{d\sigma}{d\Omega}$ data for $W = 2.330 \pm 0.010$ GeV

$\cos\theta^{\eta'}_{cm}$	$\pm d\cos\theta^{\eta'}_{cm}$	$\frac{d\sigma}{d\Omega}\left[\frac{\mu b}{sr}\right]$	$\Delta\left(\frac{d\sigma}{d\Omega}\right)$
-0.6125	0.0375	0.008732281	0.001309842
-0.5375	0.0375	0.007168361	0.001075254
-0.4625	0.0375	0.01016431	0.001524647
-0.3875	0.0375	0.008942798	0.00134142
-0.3125	0.0375	0.005015417	0.0007523126
-0.2375	0.0375	0.003954974	0.0005932461
-0.1625	0.0375	0.004859784	0.0007289676
-0.0875	0.0375	0.007332777	0.001099916
-0.0125	0.0375	0.007356951	0.001103543
0.0625	0.0375	0.009756714	0.001463507
0.1375	0.0375	0.01089654	0.001634481
0.2125	0.0375	0.01797617	0.002696426
0.2875	0.0375	0.01714692	0.002572038
0.3625	0.0375	0.01370093	0.00205514
0.4375	0.0375	0.03063086	0.00459463
0.5125	0.0375	0.03972464	0.005958696
0.5875	0.0375	0.05286775	0.007930162
0.6625	0.0375	0.06290077	0.009435115
0.7375	0.0375	0.07852696	0.01177904
0.8125	0.0375	0.1074581	0.01611871

TABLE 39. $\frac{d\sigma}{d\Omega}$ data for $W = 2.350 \pm 0.010$ GeV

$\cos\theta^{\eta'}_{cm}$	$\pm d\cos\theta^{\eta'}_{cm}$	$\frac{d\sigma}{d\Omega}\left[\frac{\mu b}{sr}\right]$	$\Delta\left(\frac{d\sigma}{d\Omega}\right)$
-0.6125	0.0375	0.004289021	0.0006433531
-0.5375	0.0375	0.007954809	0.001193221
-0.4625	0.0375	0.006030439	0.0009045658
-0.3875	0.0375	0.007822247	0.001173337
-0.3125	0.0375	0.005516218	0.0003774328
-0.2375	0.0375	0.005215077	0.0007822615
-0.1625	0.0375	0.006553603	0.0009830405
-0.0875	0.0375	0.006999124	0.001049869
-0.0125	0.0375	0.01085278	0.001627917
0.0625	0.0375	0.008114471	0.001217171
0.1375	0.0375	0.007183496	0.0006275244
0.2125	0.0375	0.0137387	0.002060804
0.2875	0.0375	0.02463611	0.003695417
0.3625	0.0375	0.02426786	0.003640179
0.4375	0.0375	0.03644476	0.005466714
0.5125	0.0375	0.02846118	0.004269177
0.5875	0.0375	0.05182724	0.007774086
0.6625	0.0375	0.08261397	0.01239209
0.7375	0.0375	0.09202031	0.01380305
0.8125	0.0375	0.09914898	0.01487235

TABLE 40. $\frac{d\sigma}{d\Omega}$ data for $W = 2.380 \pm 0.020$ GeV

$\cos\theta^{\eta'}_{cm}$	$\pm d\cos\theta^{\eta'}_{cm}$	$\frac{d\sigma}{d\Omega}\left[\frac{\mu b}{sr}\right]$	$\Delta\left(\frac{d\sigma}{d\Omega}\right)$
-0.6125	0.0375	0.003439683	0.0006879365
-0.5375	0.0375	0.006397519	0.001479504
-0.4625	0.0375	0.00808561	0.002017121
-0.3875	0.0375	0.003935012	0.0003870024
-0.3125	0.0375	0.005124992	0.001024998
-0.2375	0.0375	0.005691437	0.001138287
-0.1625	0.0375	0.004951225	0.000990245
-0.0875	0.0375	0.01059925	0.00211985
-0.0125	0.0375	0.009943535	0.001988707
0.0625	0.0375	0.004704973	0.0007409945
0.1375	0.0375	0.01518588	0.003037175
0.2125	0.0375	0.01288198	0.002576395
0.2875	0.0375	0.01241571	0.002483143
0.3625	0.0375	0.02208237	0.004416475
0.4375	0.0375	0.01533162	0.003066324
0.5125	0.0375	0.02659439	0.005318877
0.5875	0.0375	0.04905312	0.009810623
0.6625	0.0375	0.05542368	0.01108474
0.7375	0.0375	0.06742439	0.01348488
0.8125	0.0375	0.09061724	0.01812345

TABLE 41. $\frac{d\sigma}{d\Omega}$ data for $W = 2.420 \pm 0.020$ GeV

$\cos\theta^{\eta'}_{cm}$	$\pm d\cos\theta^{\eta'}_{cm}$	$\frac{d\sigma}{d\Omega}\left[\frac{\mu b}{sr}\right]$	$\Delta\left(\frac{d\sigma}{d\Omega}\right)$
-0.6125	0.0375	0.00381006	0.00236012
-0.5375	0.0375	0.003242614	0.0006485229
-0.4625	0.0375	0.002130519	0.0002261037
-0.3875	0.0375	0.007008017	0.001401603
-0.3125	0.0375	0.003300331	0.0006600663
-0.2375	0.0375	0.004450344	0.0008900687
-0.1625	0.0375	0.003039626	0.0006079252
-0.0875	0.0375	0.004886001	0.0009772002
-0.0125	0.0375	0.005849805	0.001169961
0.0625	0.0375	0.0065406	0.00310812
0.1375	0.0375	0.007156455	0.001431291
0.2125	0.0375	0.00844757	0.001689514
0.2875	0.0375	0.01821382	0.004642765
0.3625	0.0375	0.01538998	0.003077996
0.4375	0.0375	0.02069992	0.004139983
0.5125	0.0375	0.02991633	0.005983265
0.5875	0.0375	0.04392683	0.008785366
0.6625	0.0375	0.04611666	0.009223333
0.7375	0.0375	0.06791974	0.01358395
0.8125	0.0375	0.07345816	0.01469163

TABLE 42. $\frac{d\sigma}{d\Omega}$ data for $W = 2.460 \pm 0.020$ GeV

$\cos\theta^{\eta'}_{cm}$	$\pm d\cos\theta^{\eta'}_{cm}$	$\frac{d\sigma}{d\Omega}\left[\frac{\mu b}{sr}\right]$	$\Delta\left(\frac{d\sigma}{d\Omega}\right)$
-0.6125	0.0375	0.005912514	0.001182503
-0.5375	0.0375	0.003424137	0.0006848275
-0.4625	0.0375	0.002077152	0.0004154303
-0.3875	0.0375	0.0017126214	0.0001425243
-0.3125	0.0375	0.003080046	0.0006160091
-0.2375	0.0375	0.001806488	0.0003612976
-0.1625	0.0375	0.006363892	0.001872778
-0.0875	0.0375	0.001530188	0.0003060376
-0.0125	0.0375	0.006001724	0.001200345
0.0625	0.0375	0.0107137	0.002142741
0.1375	0.0375	0.006809697	0.001361939
0.2125	0.0375	0.009328133	0.001865627
0.2875	0.0375	0.01433785	0.002867569
0.3625	0.0375	0.01239963	0.002479927
0.4375	0.0375	0.0151719	0.00303438
0.5125	0.0375	0.02369766	0.004739531
0.5875	0.0375	0.03324573	0.006649147
0.6625	0.0375	0.04414127	0.008828253
0.7375	0.0375	0.06291191	0.01258238
0.8125	0.0375	0.1096725	0.02193449

TABLE 43. $\frac{d\sigma}{d\Omega}$ data for $W = 2.500 \pm 0.020$ GeV

$\cos\theta^{\eta'}_{cm}$	$\pm d\cos\theta^{\eta'}_{cm}$	$\frac{d\sigma}{d\Omega}\left[\frac{\mu b}{sr}\right]$	$\Delta\left(\frac{d\sigma}{d\Omega}\right)$
-0.6125	0.0375	0.003196983	0.0007992458
-0.5375	0.0375	0.001192025	0.0002980062
-0.4625	0.0375	0.001183027	0.0001795757
-0.3875	0.0375	0.001481957	0.0003704893
-0.3125	0.0375	0.001564945	0.0003912362
-0.2375	0.0375	0.002499707	0.0006249266
-0.1625	0.0375	0.006560223	0.001890056
-0.0875	0.0375	0.007370022	0.00092505
-0.0125	0.0375	0.004512946	0.0003782365
0.0625	0.0375	0.006969774	0.00642443
0.1375	0.0375	0.00152241	0.000180602
0.2125	0.0375	0.002428659	0.0006071647
0.2875	0.0375	0.001888922	0.0004722305
0.3625	0.0375	0.007727962	0.000931991
0.4375	0.0375	0.003907208	0.0009768021
0.5125	0.0375	0.01585854	0.001964634
0.5875	0.0375	0.02854106	0.007135264
0.6625	0.0375	0.04944441	0.0043611
0.7375	0.0375	0.05789483	0.00547371
0.8125	0.0375	0.1010014	0.01525034

TABLE 44. $\frac{d\sigma}{d\Omega}$ data for $W = 2.540 \pm 0.020$ GeV

$\cos\theta^{\eta'}_{cm}$	$\pm d\cos\theta^{\eta'}_{cm}$	$\frac{d\sigma}{d\Omega}\left[\frac{\mu b}{sr}\right]$	$\Delta\left(\frac{d\sigma}{d\Omega}\right)$
-0.6125	0.0375	0.001921216	0.00017842
-0.5375	0.0375	0.001739837	0.0003479675
-0.4625	0.0375	0.001394763	0.0002789526
-0.3875	0.0375	0.001749773	0.000149955
-0.3125	0.0375	0.001033204	0.0002066408
-0.2375	0.0375	0.001994448	0.0003988897
-0.1625	0.0375	0.005635781	0.00734156
-0.0875	0.0375	0.004670004	0.0009340008
-0.0125	0.0375	0.005212459	0.00062492
0.0625	0.0375	0.004829325	0.0009658651
0.1375	0.0375	0.007000614	0.000700123
0.2125	0.0375	0.009288988	0.000857798
0.2875	0.0375	0.004890108	0.0009780217
0.3625	0.0375	0.008011029	0.001602206
0.4375	0.0375	0.005912882	0.00082576
0.5125	0.0375	0.02287262	0.004574524
0.5875	0.0375	0.02292876	0.004585753
0.6625	0.0375	0.03784345	0.007568691
0.7375	0.0375	0.05108257	0.0051651
0.8125	0.0375	0.06698237	0.00639647

TABLE 45. $\frac{d\sigma}{d\Omega}$ data for $W = 2.580 \pm 0.020$ GeV

$\cos\theta^{\eta'}_{cm}$	$\pm d\cos\theta^{\eta'}_{cm}$	$\frac{d\sigma}{d\Omega}\left[\frac{\mu b}{sr}\right]$	$\Delta\left(\frac{d\sigma}{d\Omega}\right)$
-0.6125	0.0375	0.00375705	0.0007514101
-0.5375	0.0375	0.001395024	0.0002790048
-0.4625	0.0375	0.0009604822	0.0001064179
-0.3875	0.0375	0.001753251	0.0003506502
-0.3125	0.0375	0.002618278	0.0005236556
-0.2375	0.0375	0.001157468	0.0002314937
-0.1625	0.0375	0.002618278	0.0001920964
-0.0875	0.0375	0.006741399	0.00134828
-0.0125	0.0375	0.004433619	0.0008867238
0.0625	0.0375	0.006363535	2.403985e-04
0.1375	0.0375	0.003396804	0.001272707
0.2125	0.0375	0.008112113	0.0006793608
0.2875	0.0375	0.003325523	0.001622423
0.3625	0.0375	0.003977073	0.0004651045
0.4375	0.0375	0.01055155	0.0007954147
0.5125	0.0375	0.01914663	0.00211031
0.5875	0.0375	0.01987435	0.003829326
0.6625	0.0375	0.04112102	0.00397487
0.7375	0.0375	0.06865016	0.008224204
0.8125	0.0375	0.06698657	0.00783003

TABLE 46. $\frac{d\sigma}{d\Omega}$ data for $W = 2.620 \pm 0.020$ GeV

$\cos\theta^{\eta'}_{cm}$	$\pm d\cos\theta^{\eta'}_{cm}$	$\frac{d\sigma}{d\Omega}\left[\frac{\mu b}{sr}\right]$	$\Delta\left(\frac{d\sigma}{d\Omega}\right)$
-0.6125	0.0375	0.003026282	0.0007565704
-0.5375	0.0375	0.00257802	0.000394505
-0.4625	0.0375	0.0007173029	0.0001793257
-0.3875	0.0375	0.0009944373	0.0002486093
-0.3125	0.0375	0.006388471	0.000597118
-0.2375	0.0375	0.004802513	0.001200628
-0.1625	0.0375	0.002026178	0.0005065446
-0.0875	0.0375	0.001787721	0.0004469301
-0.0125	0.0375	0.0058332	0.00064583
0.0625	0.0375	0.001267136	0.0003167841
0.1375	0.0375	0.002091556	0.0005228891
0.2125	0.0375	0.002064092	0.0005160229
0.2875	0.0375	0.003918611	0.0009796527
0.3625	0.0375	0.007672107	0.000918027
0.4375	0.0375	0.004249731	0.00062433
0.5125	0.0375	0.02560011	0.006400027
0.5875	0.0375	0.01684348	0.004210871
0.6625	0.0375	0.05357679	0.0053942
0.7375	0.0375	0.05049508	0.0062377
0.8125	0.0375	0.09838795	0.00096992

TABLE 47. $\frac{d\sigma}{d\Omega}$ data for $W = 2.660 \pm 0.020$ GeV

$\cos\theta^{\eta'}_{cm}$	$\pm d\cos\theta^{\eta'}_{cm}$	$\frac{d\sigma}{d\Omega}\left[\frac{\mu b}{sr}\right]$	$\Delta\left(\frac{d\sigma}{d\Omega}\right)$
-0.6125	0.0375	0.0019992	0.0003998399
-0.5375	0.0375	0.001028262	0.0002056524
-0.4625	0.0375	0.0008103393	0.0001620679
-0.3875	0.0375	0.00133841	0.0002676819
-0.3125	0.0375	0.0016724416	0.0001344883
-0.2375	0.0375	0.002373279	0.0004746559
-0.1625	0.0375	0.001733588	0.0003467176
-0.0875	0.0375	0.001984559	0.0003969117
-0.0125	0.0375	0.004630781	0.0009261562
0.0625	0.0375	0.002180126	0.0002360253
0.1375	0.0375	0.002560149	0.0003120297
0.2125	0.0375	0.002244725	0.0002489449
0.3625	0.0375	0.006135997	4.935519e-05
0.4375	0.0375	0.00615062	0.001227199
0.5125	0.0375	0.008686558	0.001230124
0.5875	0.0375	0.02116351	0.001737312
0.6625	0.0375	0.03084692	0.004232702
0.7375	0.0375	0.04084692	0.006169384
0.8125	0.0375	0.04441338	0.008882677

TABLE 48. $\frac{d\sigma}{d\Omega}$ data for $W = 2.705 \pm 0.025$ GeV

$\cos\theta^{\eta'}_{cm}$	$\pm d\cos\theta^{\eta'}_{cm}$	$\frac{d\sigma}{d\Omega}\left[\frac{\mu b}{sr}\right]$	$\Delta\left(\frac{d\sigma}{d\Omega}\right)$
-0.6125	0.0375	0.001087858	0.0002175716
-0.5375	0.0375	0.0008115155	0.0001623031
-0.3875	0.0375	0.001277962	0.0002555923
-0.2375	0.0375	0.0009437799	0.000188756
-0.1625	0.0375	0.001325875	0.000265175
-0.0875	0.0375	0.0022782676	0.0001556535
-0.0125	0.0375	0.00220606	0.0004412119
0.1375	0.0375	0.004174573	0.001034915
0.2125	0.0375	0.00562374	0.001324748
0.2875	0.0375	0.001748479	0.0003496958
0.3625	0.0375	0.00332434	0.000664868
0.4375	0.0375	0.002364784	0.0004729568
0.5125	0.0375	0.005352685	0.001070537
0.5875	0.0375	0.01653375	0.003306751
0.6625	0.0375	0.02268334	0.004536667
0.7375	0.0375	0.03401515	0.006803029
0.8125	0.0375	0.08351634	0.00870327

APPENDIX B

$M_X^2(p\pi^+\pi^-)$ DISTRIBUTIONS

The figures below show $M_X^2(p\pi^+\pi^-)$ distributions after side band substraction (FIG. 43) for $m_{\pi\pi}$ bins in the range 500 - 860 MeV with a regular background fitted with a polynomial of first order. Depending on each bin, after the polynomial background is rejected, the signal is obtained from a gaussian or double gaussian fit to the histogram.

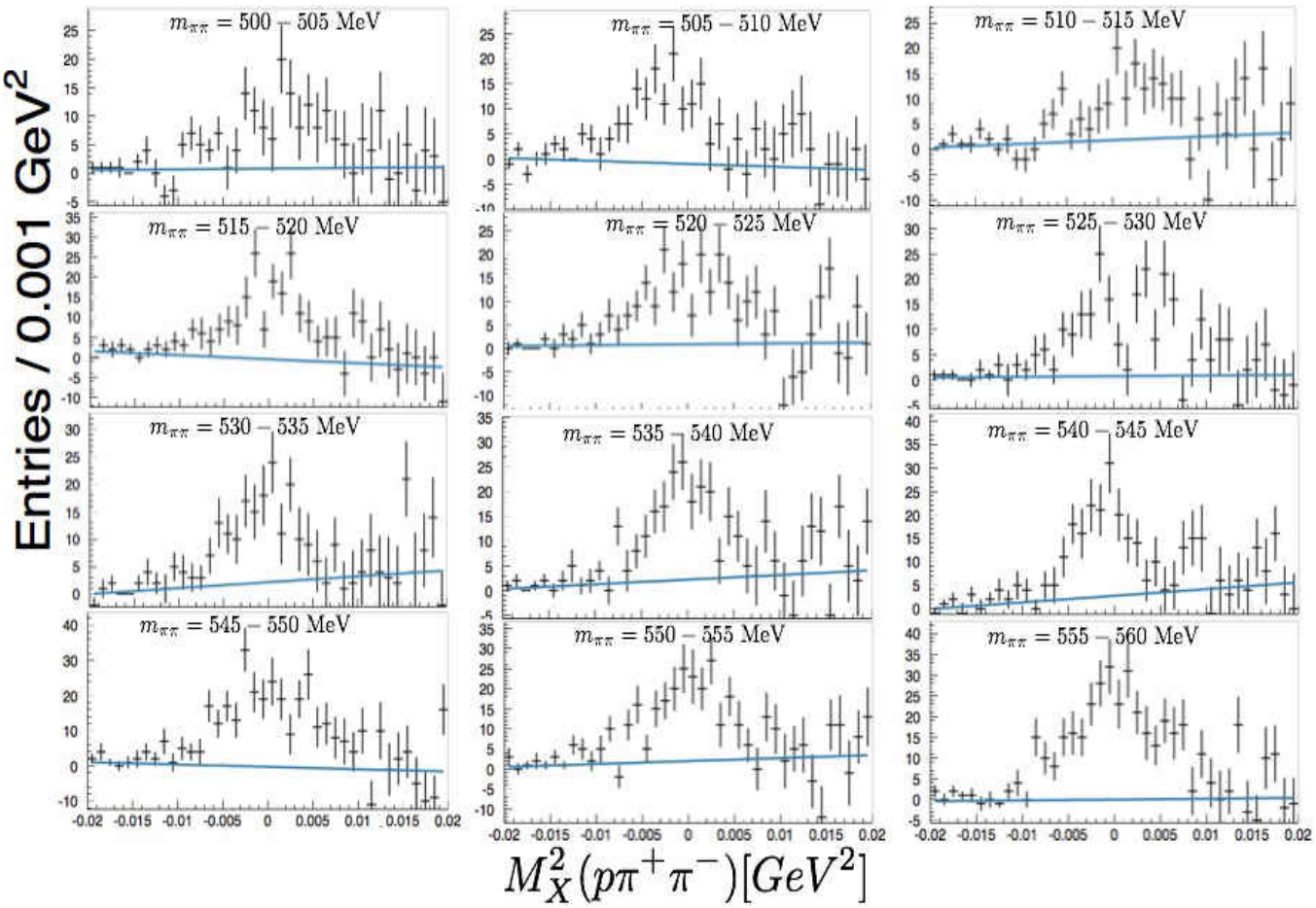

FIG. 72. $M_X^2(p\pi^+\pi^-)$ distributions after side band substraction (FIG. 43) for $m_{\pi\pi}$ bins in the range 500 - 560 MeV.

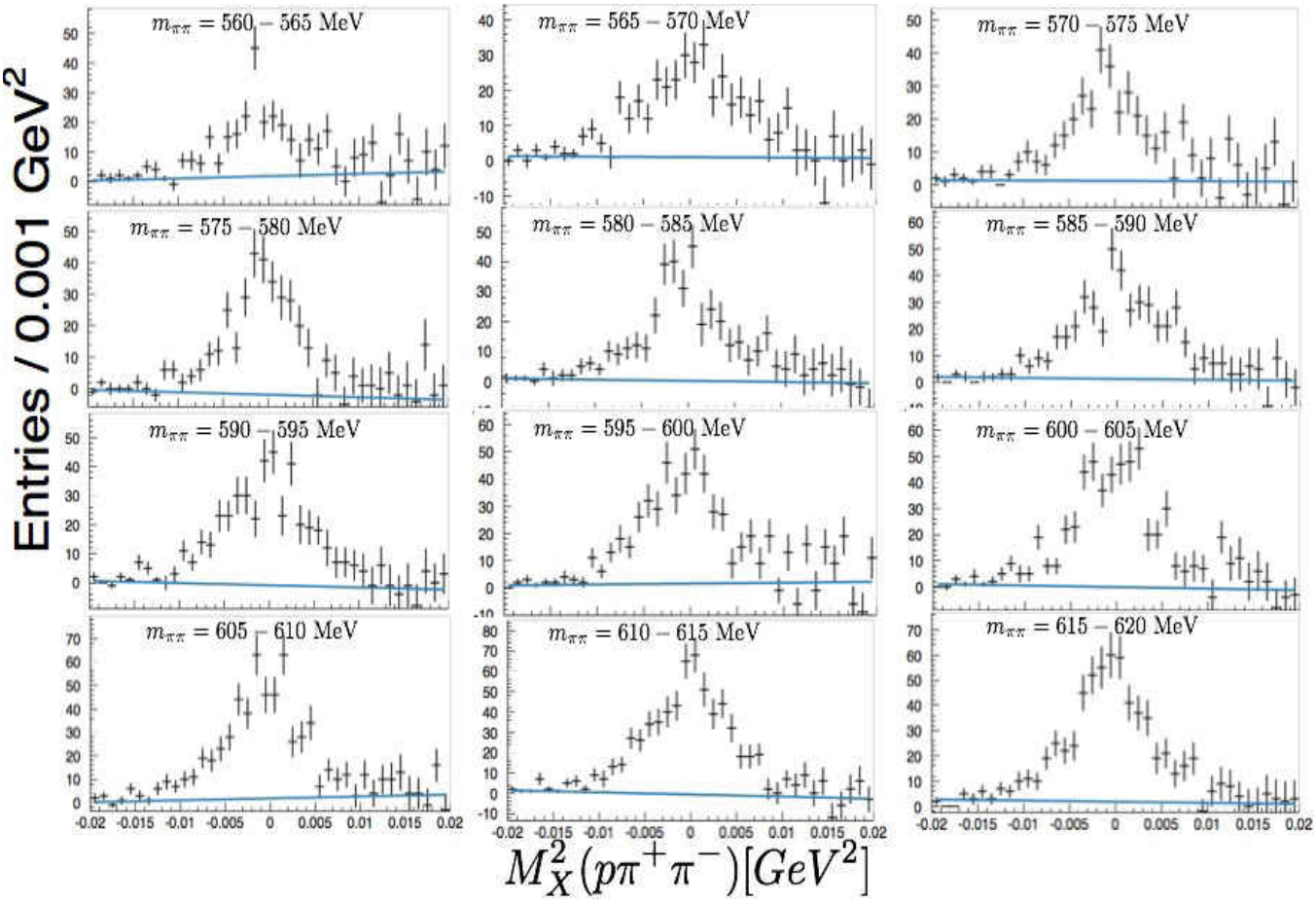

FIG. 73. $M_X^2(p\pi^+\pi^-)$ distributions after side band substraction (FIG. 43) for $m_{\pi\pi}$ bins in the range 560 - 620 MeV.

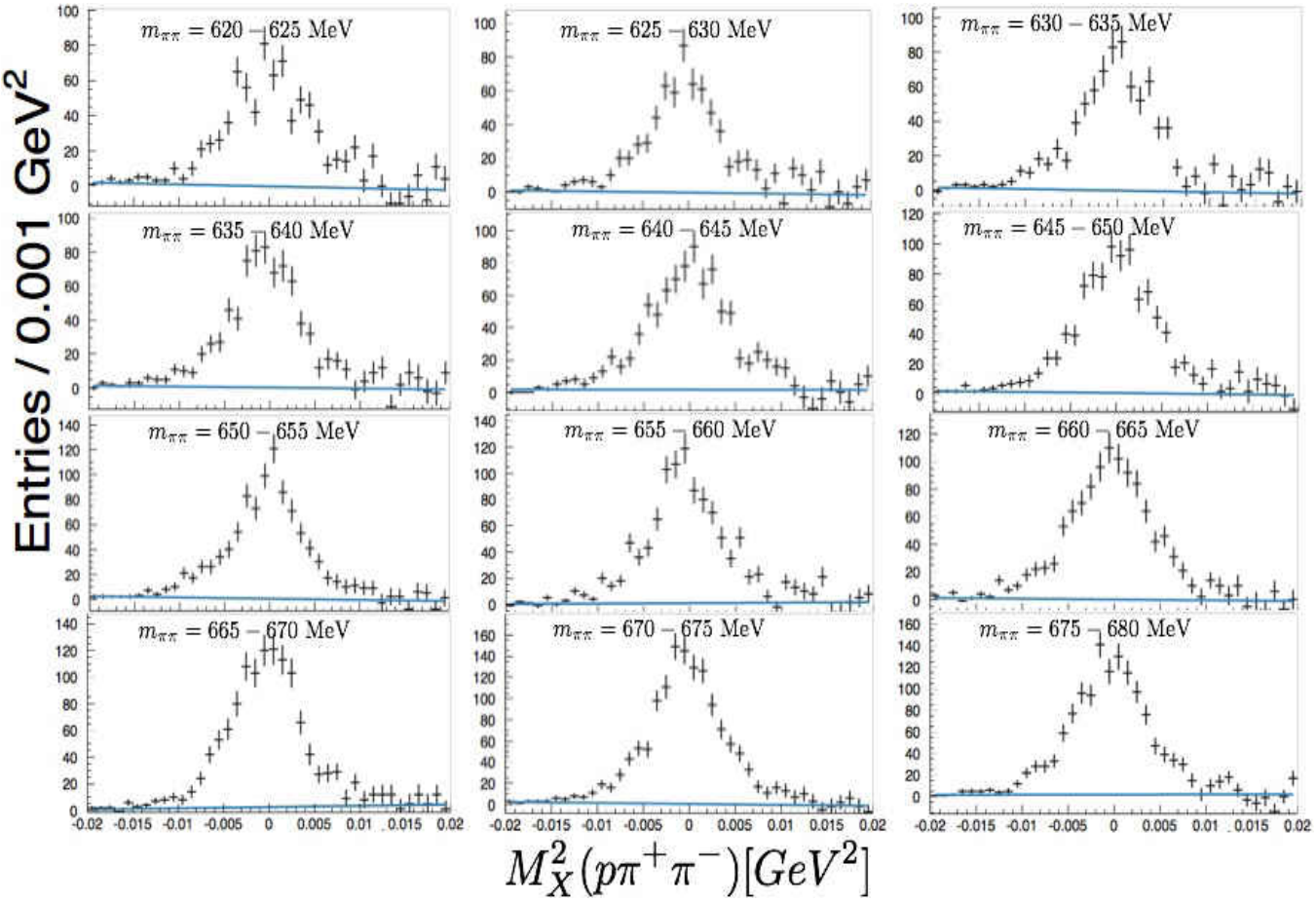

FIG. 74. $M_X^2(p\pi^+\pi^-)$ distributions after side band substraction (FIG. 43) for $m_{\pi\pi}$ bins in the range 620 - 680 MeV.

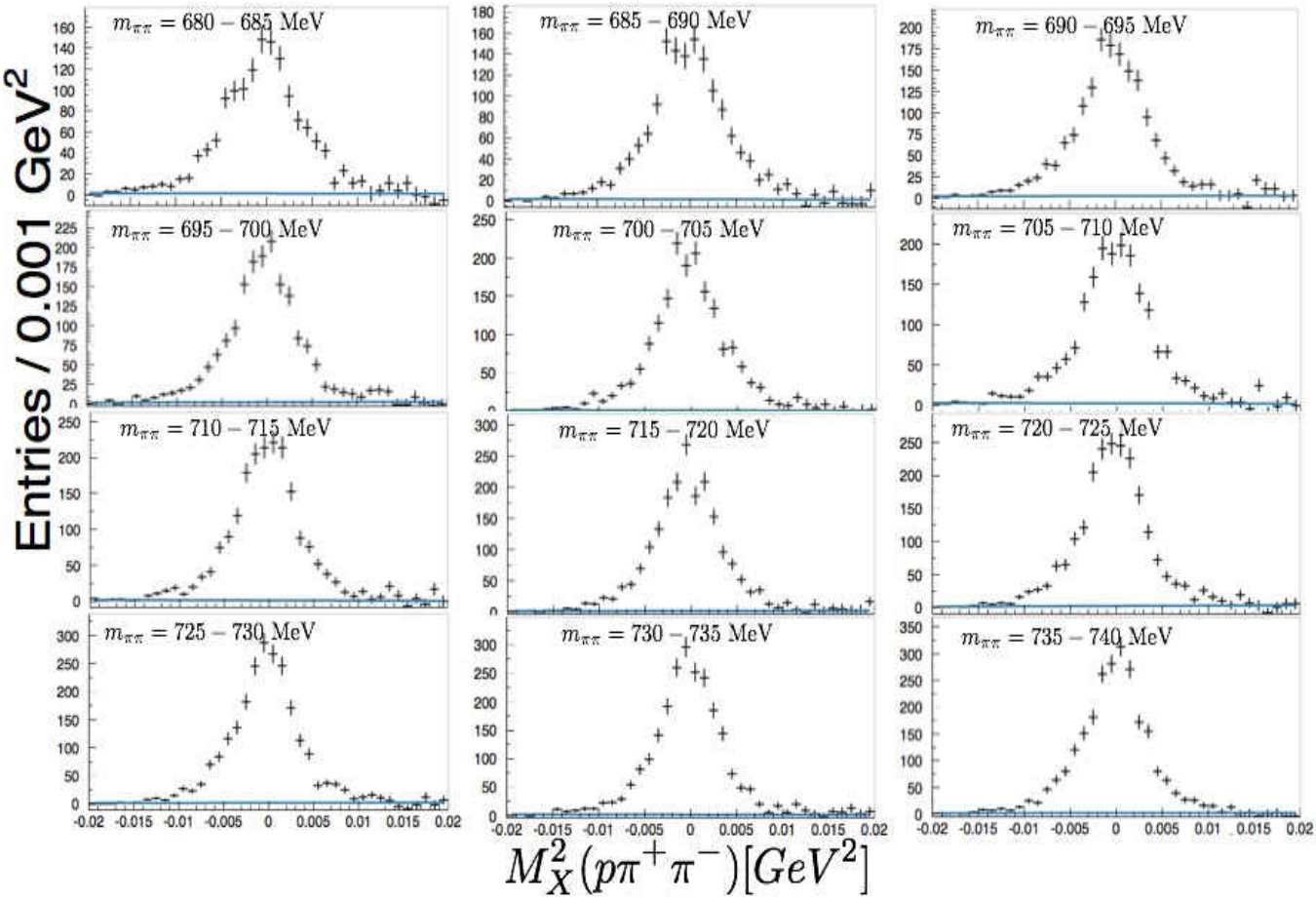

FIG. 75. $M_X^2(p\pi^+\pi^-)$ distributions after side band substraction (FIG. 43) for $m_{\pi\pi}$ bins in the range 680 - 740 MeV.

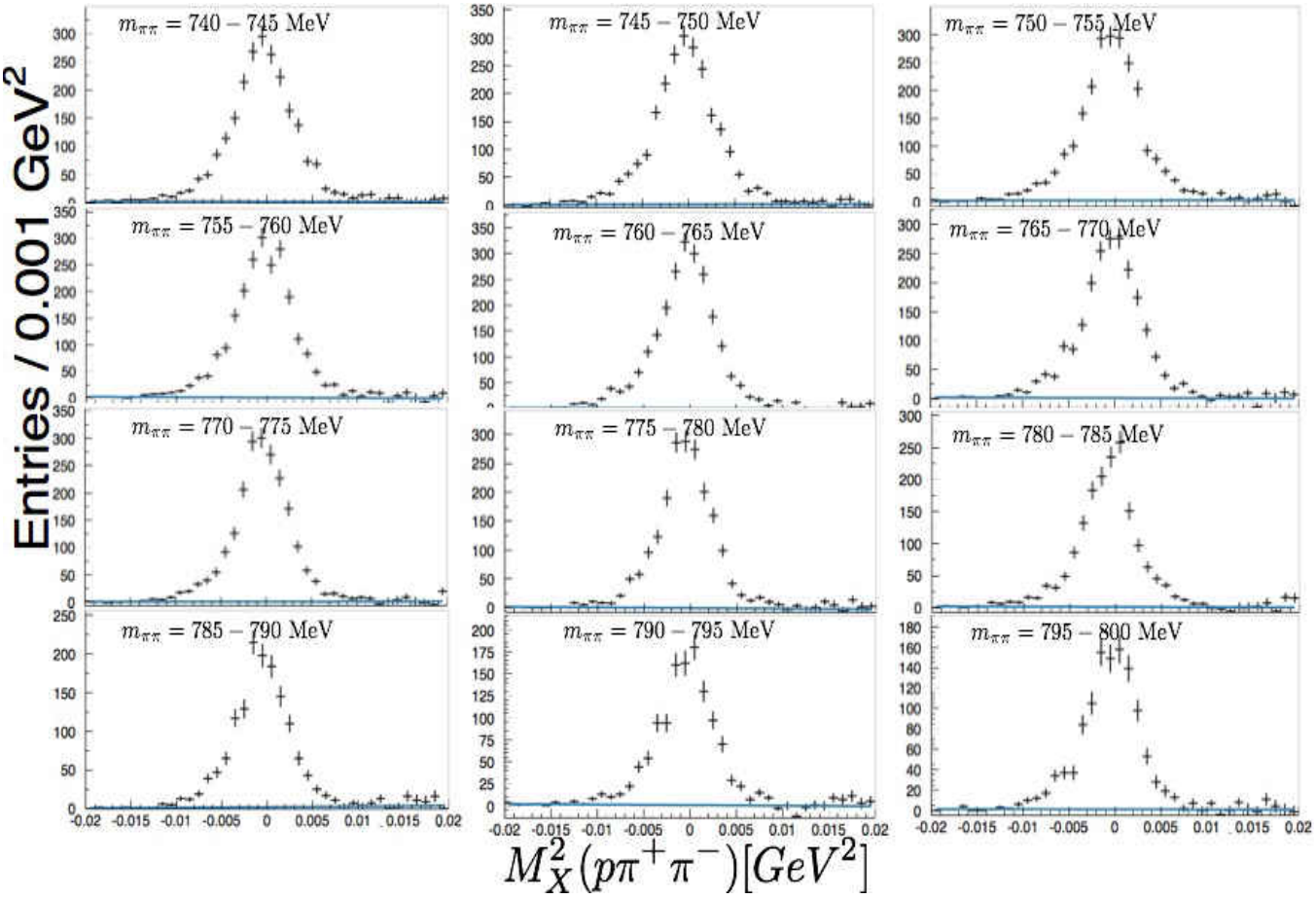

FIG. 76. $M_X^2(p\pi^+\pi^-)$ distributions after side band substraction (FIG. 43) for $m_{\pi\pi}$ bins in the range 740 - 800 MeV.

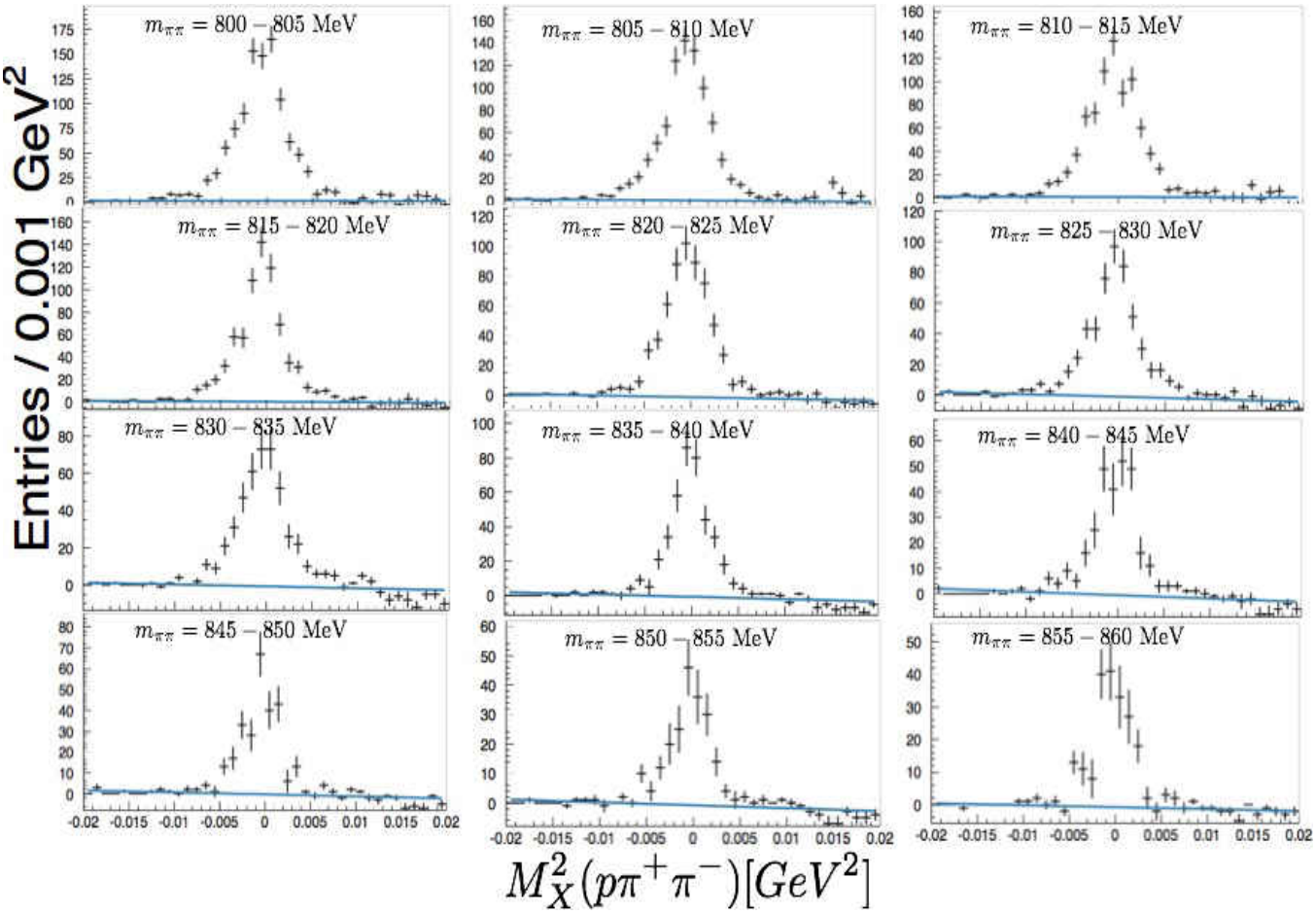

FIG. 77. $M_X^2(p\pi^+\pi^-)$ distributions after side band substraction (FIG. 43) for $m_{\pi\pi}$ bins in the range 800 - 860 MeV.

VITA

Georgie Mbianda Njencheu
Department of Physics
Old Dominion University
Norfolk, VA 23529

August 2012 - May 2017:	PhD in Physics- Old Dominion University, Norfolk, VA, USA
August 2010 - May 2012:	MS in Physics- Old Dominion University, Norfolk, VA, USA
August 2008 - June 2010:	MEng in Materials and Sensor Systems for Environmental Technologies - University of Bologna, Italy and Polytechnic University of Valencia, Spain
August 2006 - June 2008:	MSc in Physics - University of the Witwatersrand, Johannesburg, South Africa
August 2005 - June 2006:	PGDip in Mathematical Sciences - AIMS (African Institute for Mathematical Sciences) University of Cape Town, South Africa
January 1994 - July 1997:	BSc in Physics and Computer Science - University of Buea, Cameroon

Typeset using LaTeX.